Supramolecular Binding and Separation of Hydrocarbons within a Functionalised Porous Metal-Organic Framework

Sihai Yang,[1]* Anibal J. Ramirez-Cuesta,[2] Ruth Newby,[1] Victoria Garcia-Sakai,[3] Pascal Manuel,[3] Samantha K. Callear,[3] Stuart I. Campbell,[4] Chiu C. Tang[5] and Martin Schröder[1]*

[1] School of Chemistry, University of Nottingham, University Park, Nottingham, NG7 2RD (UK)

Fax: +44 115 951 3563 E-mail: Sihai.Yang@nottingham.ac.uk; M.Schroder@nottingham.ac.uk

[2] The Chemical and Engineering Materials Division (CEMD), Neutron Sciences Directorate, Oak Ridge National Laboratory, Oak Ridge, TN 37831 (USA)

[3] ISIS Neutron Facility, STFC Rutherford Appleton Laboratory, Chilton, Oxfordshire, OX11 0QX (UK)

[4] Neutron Data Analysis and Visualization Division (NDAV), Neutron Sciences Directorate, Oak Ridge National Laboratory, Oak Ridge, TN 37831 (USA)

[5] Diamond Light Source, Harwell Science and Innovation Campus, Didcot, Oxfordshire, OX11 0DE (UK)

Supramolecular interactions are fundamental to host-guest binding in chemical and biological processes. Direct visualisation of such supramolecular interactions within host-guest systems is extremely challenging but crucial for the understanding of their function. We report a comprehensive study combining neutron scattering with synchrotron X-ray and neutron diffraction, coupled with computational modelling, to define the detailed binding at a molecular level of acetylene, ethylene and ethane within the porous host NOTT-300. This study reveals the simultaneous and cooperative hydrogen-bonding, $\pi\cdots\pi$ stacking interactions and inter-molecular dipole interactions in the binding of acetylene and ethylene to give up to twelve individual weak supramolecular interactions aligned within the host to form an optimal geometry for intelligent, selective binding of hydrocarbons. We also report, for the first time, the cooperative binding of a mixture of acetylene and ethylene within the porous host together with the corresponding breakthrough experiment and analysis of mixed gas adsorption isotherms.

There is great current interest in the use of porous materials for substrate storage and separations, catalysis, drug delivery, and sensing.[1-5] Understanding the host-guest interactions in these systems is vital if new generations of improved materials are to be developed. However, gaining such insight is challenging and often not feasible in large void materials due to lack of order in porous systems such as carbon, mesoporous silica and zeolites,[5] and also because the nature of these host-guest interactions is often based upon very weak and dynamic supramolecular contacts such as hydrogen-bond, $\pi \cdots \pi$ stacking, van der Waals, electrostatic or dipole interactions. Such supramolecular binding usually involves many hydrogen atoms and undergoes dynamic processes that are difficult to probe directly by experiment.[2,6]

Recent studies on porous metal-organic frameworks (MOFs) for hydrogen storage,[7,8] carbon capture,[1] and hydrocarbon separations[9,10] have shown, in exceptional cases, location of guest molecules within the host *via* advanced crystallography studies, providing invaluable structural rationale for their function and properties. Most of these successes have been achieved within host systems that display strong confinement effects on the guest molecules and/or have specific relatively strong binding sites such as open metal centers.[7-12] However, host-guest systems involving primarily soft supramolecular interactions usually lead to serious positional disorder of the guest molecules, and hydrogen atoms involved in these binding processes are not readily seen or defined from crystallography studies,[13,14] leading to problems in defining the ***dynamics*** and ***motions*** of such host-guest systems. As a result, information on molecular binding dynamics and the motion of guests within the confined space of MOF hosts is largely lacking. Herein, we report the application of combined inelastic, quasi-elastic and elastic neutron scattering and synchrotron X-ray diffraction coupled to density functional theory (DFT) calculations to directly visualise the dynamics of host-guest interactions between adsorbed C_2-hydrocarbons and the hydroxyl-functionalised porous MOF NOTT-300, which exhibits high selectivity and uptake capacity for unsaturated hydrocarbons. Moreover, direct observation of the mobility and diffusion for these adsorbed hydrocarbons within NOTT-300 has been achieved, representing important methodologies for their potential kinetic separations. These complementary experiments using dynamic, kinetic and static approaches lead to the same conclusion: four types of soft supramolecular interactions cooperatively bind guest molecules in these functionalised cavities, and these fine-tuned interactions lead to optimal uptake kinetics and binding dynamics affording excellent selectivities between these hydrocarbons.

Results and discussion

Material and characterisation. The complex [Al$_2$(OH)$_2$(L)] (L = biphenyl-3,3',5,5'-tetracarboxylate) (NOTT-300)[15] was selected for this study since it exhibits both high thermal, chemical and water stability and a polyfunctional pore environment. Its large scale (~20 grams) synthesis can be achieved *via* traditional hydrothermal batch reactions enabling multiple studies by neutron scattering. NOTT-300 exhibits an open structure comprising

chains of $[AlO_4(OH)_2]$ moieties bridged by tetracarboxylate ligands L^{4-} to afford a porous structure with channels formed by corner-sharing $[AlO_4(OH)_2]$ octahedra linked *via* two mutually *cis*-μ_2-OH groups. Desolvated NOTT-300 displays a surface area of 1370 m^2 g^{-1} and 6.5 Å-wide channels.

Analysis of gas adsorption isotherms and selectivity. At 293 K, the total adsorption uptakes for C_2H_2, C_2H_4, C_2H_6, and CH_4 in NOTT-300 were measured as 6.34, 4.28, 0.85, 0.29 mmol g^{-1}, respectively at 1.0 bar (Figure 1a). The difference in the uptakes between C_2H_2 and C_2H_4 is 2.06 mmol g^{-1}, and is significant (~48% of the total alkene uptake) compared to the complexes $[M_2(dobdc)]$ (M = Mg, Mn, Fe, Co, Ni, Zn; dobdc^{2-} = 2,5-dihydroxybenzene-1,4-dicarboxylate)[9,10] (Table 1). Although the alkyne/alkene uptake difference in NOTT-300 is comparable to that observed in HOF-1[16] and M'MOF-3a[17], the latter systems display much lower absolute uptakes with separation achieved using narrow pore windows, leading to an intrinsic trade-off between selectivity and capacity, two important factors for practical separation systems. The difference in the uptakes between ethylene and ethane in NOTT-300 is 3.43 mmol g^{-1}, approximately twice that observed in the best performing alkene/alkane separation solids $[M_2(dobdc)]$ (~1.5 mmol g^{-1})[9] and PAF-1-SO$_3$Ag (~1.6 mmol g^{-1}).[18] NOTT-300 shows an especially low uptake capacity for CH_4.

Analysis of the pure-component isotherms at 293 K *via* ideal adsorbed solution theory (IAST)[19] was carried out to estimate selectivity between these hydrocarbons as a function of varying composition (from 10:90 to 90:10) since hydrocarbon compositions will vary in different applications (Figures 1b-c and Supplementary Figure 70). Results for equimolar mixtures at 1.0 bar are discussed here (Table 1). The C_2H_2/C_2H_4 selectivity of 2.30 for NOTT-300 by IAST is higher than that oserved for $[Fe_2(dobdc)]$ (1.87),[10] but is lower than for M'MOF-3a (5.23),[17] although the latter system exhibits a relatively low total capacity owing to the narrow pore. The selectivity for C_2H_4/C_2H_6 in NOTT-300 was calculated to be 48.7. Significantly, this value is higher than that observed for zeolites NaX (9.5),[20] NaETS-10 (15),[21] and for the MOF materials $[Fe_2(dobdc)]$ (13.6),[10] $[Co_2(dobdc)]$ (6),[9,22] $[Mn_2(dobdc)]$ (8),[9] HKUST-1 (4),[20] and the polymer PAF-1-SO$_3$Ag (26.9),[18] which are the current state-of-the-art ethylene/ethane separating materials. Thus, NOTT-300 shows the highest selectivity reported so far. Moreover, the alkene/alkane selectivity in $[M_2(dobdc)]$ (M = Fe, Co, Mn) and HKUST-1 relies upon strong binding of unsaturated hydrocarbons at open metal sites, and these materials lose activity (and often porosity) rapidly on exposure to moisture. In contrast, NOTT-300, with soft functional groups and a saturated coordination sphere at Al(III), demonstrates excellent structural stability to water and other organic vapours with retention of porosity upon regeneration.[15] The C_2H_2/CH_4, C_2H_4/CH_4, and C_2H_6/CH_4 selectivities in NOTT-300 were estimated by IAST analysis as >1000, ~380, and 5, respectively. These selectivities are, however, subject to uncertainties associated with isotherm measurement of the extremely low methane uptake in NOTT-300. The above IAST selectivity data are entirely consistent with the

direct comparison of the uptake ratios between the corresponding hydrocarbons derived from the experimental isotherms (Table 1, Supplementary Figure 35).

To validate these selectivities, we also measured dual-component adsorption isotherms for equimolar mixtures of C_2H_2/C_2H_4, C_2H_4/C_2H_6, C_2H_2/CH_4, and C_2H_4/CH_4 at 293 K under flow mode. In contrast to a typical static isotherm experiment, flow experiments enable the gas in the sample station to be constantly refreshed by a flow of an equimolar gas mixture to ensure that the composition of the mixture is unchanged throughout the experiment. The measured uptakes were compared with those predicted by IAST[19] calculations (Figures 1d, 4c, Supplementary Figures 71-74), and excellent agreement between the observed experimental isotherms and IAST calculations are observed in all cases, confirming the applicability and complementarity of these approaches. A slightly higher experimental uptake was recorded in the C_2H_2/C_2H_4 mixture measurement, indicating the presence of slightly enhanced selectivity in practical C_2H_2/C_2H_4 separations (*i.e.*, ~4 versus 2.3 predicted by IAST). Given that NOTT-300 displays a different kinetic profile for each C_2-hydrocarbon (*i.e.*, fast, moderate and slow for C_2H_2, C_2H_4 and C_2H_6, respectively, Supplementary Figure 33), its practical selectivity for C_2-hydrocarbon separation may be enhanced further by contributions from kinetic aspects.[23] Comparison of both the capacity and selectivity data confirms that NOTT-300 has potential for the separation of C_2-alkyne/alkene, C_2-alkene/alkane, C_2/C_1-hydrocarbon mixtures, which is relevent to the purification of ethylene, to olefin/paraffin separations, and natural gas upgrading, respectively. We therefore sought to understand these properties at the molecular level.

Studies of the preferred binding sites and supramolecular interactions. The binding sites for C_2H_2, C_2H_4, and C_2H_6 were studied by *in situ* synchrotron X-ray and neutron powder diffraction experiments, with deuterated substrates used in neutron experiments. Two independent binding sites (I and II) were observed in each case: the unsaturated C_2-molecules at Site I exhibit a side-on interaction to the HO-Al group *via* formation of weak hydrogen bonds that are supplemented by additional supramolecular contacts to the aromatic hydrogen atoms and $\pi\cdots\pi$ stacking interactions to the phenyl rings; C_2-molecules at Site II are located in the middle of the pore and interact primarily with the molecules at Site I *via* intermolecular dipole interactions. The bond distances obtained from independent analysis of synchrotron X-ray diffraction, neutron diffraction, and DFT calculations are compared in Figure 3 with very good agreement observed between the three methods.

In addition to the static crystallography study, we have, for the first time, successfully combined inelastic neutron scattering (INS) and DFT[24] to visualise the binding dynamics for adsorbed C_2H_2, C_2H_4, and C_2H_6 molecules in NOTT-300 (Figure 2). Comparison of INS spectra, measured at temperatures below 7($\pm$0.1) K to minimise the thermal motion of the adsorbed hydrocarbons and the host, reveals five major changes in peak intensity on going from bare NOTT-300 to NOTT-300·$3C_2H_2$ (Figure 2d). Peaks I and II occur at low energy transfer (5-24, 25-50 meV, respectively) and Peak III, IV, and V at high energy transfer (80, 95, 120 meV, respectively). Peaks I, III and

IV can be assigned to translational, symmetric and asymmetric C-H vibrational motions of adsorbed C_2H_2 molecules, respectively, based upon the INS spectra for condensed C_2H_2 in the solid state. Peaks III and IV are changed compared to free C_2H_2 from singlets to doublets, indicating removal of the degeneracy of the C-H vibrational modes upon binding of C_2H_2 to the host *via* its π-electrons (Supplementary Figures 36-40). Moreover, the peaks in the range 100-160 meV are slightly shifted to higher energies in NOTT-300·$3C_2H_2$ (Figure 2d) compared to bare NOTT-300, indicating a stiffening of the motion of the NOTT-300 host upon C_2H_2 adsorption. To understand the changes, DFT calculations have been used to simulate the INS spectra and optimise the structures for NOTT-300 and NOTT-300·$3C_2H_2$.[25,26] Initially, the structural models obtained from synchrotron diffraction experiments were adapted in calculations. Upon convergence, excellent agreements between calculation and experiment for the structural models were obtained. In the case of diffraction experiments, disorder of molecules was observed owing not only to the thermal motion, but also to the nature of the soft binding to these molecules within the pore. Therefore, models from calculations are shown here (Figure 3) for clarity and disordered models are shown in Supplementary Information. The INS spectra derived from these calculations show excellent agreement with experimental spectra and confirm that the adsorbed C_2H_2 molecules interact side-on to the hydroxyl groups (Figure 3a). The C···O distance between C_2H_2 and the O-centre of the Al-OH group is 4.12 Å, indicating a weak hydrogen-bond between the π-electrons of C_2H_2 and the HO-Al moiety. The optimised C≡C and C-H bond distances in C_2H_2 are 1.21 and 1.07 Å, respectively, and the <HCC bond angle is 179.2°, indicating no major distortion of the C_2H_2 molecules. Additionally, each adsorbed C_2H_2 molecule is surrounded by four aromatic C-H groups and two phenyl rings, forming weak cooperative supramolecular interactions between C(δ-) of C_2H_2 and H(δ+) from -CH [C···H = 2.96-3.64 Å] and moderate-to-weak π···π stacking interactions between the electron in the π-orbitals of C_2H_2 and the aromatic π-electrons [C≡C···C_6 = 3.81 Å]. Peak II can be assigned to the –OH groups bending/wagging perpendicular to the <Al-O-Al plane and Peak V to the bending and out-of-plane wagging of the four aromatic C-H groups on two benzene rings adjacent to each C_2H_2 molecule in conjunction with the bending of the OH group along the <Al-O-Al plane (Figure 2d). The significant changes observed for Peak II and V suggest that adsorbed C_2H_2 molecules have direct interaction with the -OH and -CH groups, thereby affecting their molecular motions and inducing the changes in INS spectra. Peak I, corresponding to translational motions of C_2H_2, shifts to lower energy due to the geometry confinement in the pore. C_2H_2(II) interacts primarily with C_2H_2(I) *via* electrostatic dipole interactions between C(δ-) and H(δ+) of adjacent C_2H_2 molecules [C^I···H^{II} = 3.24 Å; C^{II}···H^I = 3.12 Å]; this is comparable to the inter-molecular distance observed in solid C_2H_2 [C^I···H^{II} = 3.09 Å] confirming that the adsorbed C_2H_2 in NOTT-300 has a restricted solid-type motion. Thus, in total, four types of weak interactions interact cooperatively to bind C_2H_2 molecules in the functionalised cavity, and leads to the removal of the degeneracy of some vibrational modes of C_2H_2. To our knowledge the Al-OH to π(C≡C) hydrogen-bond

interaction described herein has not been observed previously, and thus represents a new type of supramolecular contact in host-guest systems.

Comparison of the INS spectra of bare and C_2H_4-loaded NOTT-300 reveals a broad peak at low energy transfer (below 25 meV) without any other distinct energy transfer peaks (Figure 2e). This is characteristic of the one dimensional, almost free, recoil rotational motion of C_2H_4 molecules along its C=C axis. Indeed, DFT calculations based upon these INS spectra suggest two models with different orientations of C_2H_4 in the channel (Figures. 3b-c). In the first model, the plane of C_2H_4 molecule is perpendicular to the –OH group (denoted as "ground-state", NOTT-300·C_2H_4G); in the second model, the plane of C_2H_4 molecule is parallel to the –OH group (denoted as "excited state", NOTT-300·C_2H_4E). The energy barrier for this rotational motion between the "ground" and "excited" states of NOTT-300·C_2H_4 is estimated to be 0.93 kJ mol^{-1}. NOTT-300·C_2H_4G has a lower energy and is, therefore, thermodynamically more stable. Because of the orientation of the π-orbital of C_2H_4 molecules, the π-electrons of C_2H_4 have better overlap with the hydroxyl group in the "ground-state" than that in the "excited-state". This is also confirmed by the neutron diffraction experiment: the refinement based upon the model of NOTT-300·C_2H_4G yields much improved R factors than that of NOTT-300·C_2H_4E, indicating the favourable orientation of NOTT-300·C_2H_4G that dominates the bulk sample. But, due to the reduced π-electron density in C_2H_4 compared to C_2H_2, the C⋯HO distance between the C_2H_4 molecule and the O-centre of hydroxyl group is elongated as 4.62 Å, suggesting a weaker hydrogen-bond in comparison to that in NOTT-300·3C_2H_2. The C⋯O distance is further increased to 4.97 Å in NOTT-300·C_2H_4E, indicating weaker hydrogen bonding. However, better overlap of the π⋯π stacking interaction between the π-electrons of C_2H_4 molecules and phenyl rings can be achieved in this "excited state" moiety, thus stabilising this orientation. Interestingly, a comparable hydrogen bond interaction between π-electrons of C_2H_4 molecules and bridging –OH group in a zeolite has been observed recently *via* infrared spectroscopic experiments.[27] Similarly, comparison of the INS spectra for bare and C_2H_6 loaded NOTT-300 reveals a major peak at low energy transfer corresponding to the 1D recoil rotational motion of C_2H_6 molecule along its C-C axis. Further DFT calculations suggest that C_2H_6 is aligned at a very long distance to –OH group [C⋯O = 5.07 Å] as a result of zero π-electron density and repulsion between the hydrogen atoms. Therefore, C_2H_6 has very weak interactions with the NOTT-300 host, consistent with the observed low uptakes. INS experiments on CH_4-loaded NOTT-300 were unsuccessful due to the ultra-low uptake of this gas.

The separation of C_2H_2 and C_2H_4 is a technologically important goal, but is highly challenging due to their similar molecular sizes, volatilities, and electronic structures based upon unsaturated carbon-carbon bonds. This leads to very similar binding interactions for these substrates to open metal sites, with low preferential adsorption.[9,10,20] Selective adsorption C_2H_2 over C_2H_4 has only been achieved recently *via* the molecular sieving mechanism in HOF-1[16] and M'MOF-3a[17] with optimal pore windows to separate these two molecules. Due to this

molecular sieving mechanism, these systems usually display relatively low total uptakes and higher selectivities are often achieved at lower temperatures. Simulated breakthrough experiments of C_2H_2 and C_2H_4 mixtures have also been carried out in [$Fe_2(dobdc)$],[10] which suggest promising selective removal of C_2H_2 and purification of C_2H_4. However, to date there is no experimental report on direct competing binding between these two molecules within a porous host, and such information is fundamental if new improved separation systems are to be developed. We therefore sought to study the dynamics of NOTT-300 loaded with an equimolar mixture of C_2H_2/C_2H_4 to determine the relative binding of these two guests. Upon loading of this mixture, a more significant increase in the scattered neutron intensity was observed compared to the single component system, indicating that both guest molecules are adsorbed in NOTT-300 (Figure 4a-b). Integration of the increased scatterings gives a C_2H_2 to C_2H_4 ratio of approximately 3:1, consistent with the selectivity obtained from IAST analysis and the mixed gas adsorption isotherm. Comparison of the difference spectra for C_2H_2-, C_2H_4-, and C_2H_2/C_2H_4-loaded NOTT-300 clearly suggests that the INS spectra of the mixed gas system contain all the features for pure C_2H_2 INS spectra (peaks I to V), and an increase in intensity of Peak I due to the incorporation of additional C_2H_4 in the cavities. Moreover, a small increase in Peak VI is observed at 135 meV corresponding to the change of –CH motion on the phenyl rings as confirmed by DFT calculations. This calculation and INS spectra further suggest that C_2H_2 interacts with the -OH group in a similar way to that observed in NOTT-300·$3C_2H_2$, consistent with Peaks (I –V). Interestingly, C_2H_4 has been found at the centre of the cavity and to interact predominantly with the C_2H_2 molecules *via* electrostatic dipole interaction between $H^e(\delta+)$ of C_2H_4 and $C^a(\delta-)$ of C_2H_2 [$C^a \cdots H^e$ = 3.37 Å] (Figure 5). These observations are also consistent with the findings obtained from corresponding neutron diffraction experiments on a C_2D_2/C_2D_4 mixture loaded into NOTT-300, although C_2D_2 and C_2D_4 molecules cannot be distinguished definitively at each site (Supplementary Table 11) indicating the possible presence of mixed site occupancy. This result confirms that in this binding competition, C_2H_2 has a stronger interaction to the host than C_2H_4 and directly supports the optimal selectivity and uptake capacity observed in the isotherm experiments. To the best of our knowledge, this INS study represents the first dynamic study of competing C_2-hydrocarbons binding in a functional host material. This most challenging alkyne/alkene separation has also been confirmed in experimental breakthrough experiments in which an equimolar mixture of C_2H_2/C_2H_4 was flowed over a packed bed of NOTT-300 under ambient conditions (Figure 4d). As predicted, C_2H_4 was the first to elute through the bed, whereas C_2H_2 was retained. Upon saturation, C_2H_2 breaks through from the bed and reaches saturation rapidly. As measured from this breakthrough experiment, for an entering equimolar mixture of C_2H_2/C_2H_4, C_2H_4 composition can be purified to 99.5% dropping to 97.5% until C_2H_2 starts to break through. To the best of our knowledge, this is the first example of an experimental breakthrough separation of a C_2H_2-C_2H_4 mixture by a MOF material.

Analysis of storage density for acetylene and ethylene. The storage density of C_2H_2 in NOTT-300 was recorded to be 0.48 g cc^{-1} at 273 K and 1.0 bar corresponding to 65% of the solid density at 189 K; this is 232 times greater than the safe compression limit for C_2H_2 storage at 2.0 bar. In comparison, the storage density of C_2H_4 in NOTT-300 was recorded to be 0.40 g cc^{-1} at 273 K and 1.0 bar corresponding to 70% of the liquid density at 169 K. Considering that the storage temperature is well above their melting/boiling points, these high precentage values suggest that C_2H_2 and C_2H_4 can be compressed efficiently in NOTT-300 even at near room temperature. Thus, NOTT-300 may also find possible application in high density acetylene storage.

Analysis of quasi-elastic neutron scattering (QENS) data. In order to analyse the mobility of adsorbed hydrocarbon molecules, we employed *in situ* QENS, a technique specifically targeted to the study of diffusion processes of small molecules within confined host systems.[28-30] QENS spectra were recorded for bare NOTT-300 as well as NOTT-300 loaded with C_2H_2, C_2H_4, and a 1:1 mixture of C_2H_2-C_2H_4 at 5-293 K (Figure 1e and Supplementary Figures 53-65). At 5 K, all QENS spectra are purely elastic with no active motions observed in either the bare or C_2H_2- and C_2H_4-loaded NOTT-300 materials, suggesting adsorbed hydrocarbon molecules are immobile. At higher temperatures (190-293 K) significant QENS broadening is observed for bare NOTT-300, corresponding to the localised motion of free hydroxyl groups. Adsorption of C_2H_2 into NOTT-300 leads to only a slight increase in QENS broadening suggesting that the adsorbed C_2H_2 molecules have limited mobility within the channel. In comparison, QENS spectra for C_2H_4-loaded NOTT-300 show significant broadening, indicating that adsorbed molecules of C_2H_4 have much higher mobility within the channel than for C_2H_2. Interestingly, QENS spectra for 1:1 C_2H_2-C_2H_4 loaded NOTT-300 are nearly identical to that for C_2H_4-loaded NOTT-300, indicating that adsorbed C_2H_4 molecules are weakly bound to the host and are dominating the mobility of the system, with C_2H_2 bound more strongly to the host and barely playing any role in the observed QENS broadening. These preliminary conclusions are entirely consistent with the INS study and confirm that adsorbed C_2H_2 has solid-type binding dynamics, while C_2H_4 shows strong recoil motion that is a reminiscent of liquid ethylene. Overall, the combined INS and QENS experiments have enabled the interrogation of molecular motion at the nano-scale and thus the microscopic phase behaviour of adsorbed hydrocarbon molecules. These findings are vital for the understanding of their selective bindings and hence separations, and are entirely consistent with the calculated of isosteric heat of adsorptions (see below). Importantly, this QENS study confirms directly that in the binding of the C_2H_2-C_2H_4 mixture within NOTT-300, C_2H_2 molecules will selectively occupy the strongest binding sites (close to -OH group), while C_2H_4 molecules are poorly bound and therefore have greater mobility and diffusivity.

Conclusions

These studies confirm that the M-OH groups, aromatic –CH groups and phenyl rings in NOTT-300 can participate in weak additive, supramolecular interactions with unsaturated hydrocarbons, and that these are

supplemented by cooperative inter-molecular dipole interactions between adsorbed hydrocarbon molecules. The binding energy of these weak supramolecular bonds can be viewed as soft dynamic interactions and are distinct from the direct bond formation between metal centres and the π-electron density of C_2H_2 or C_2H_4.[9,10,18] The latter, often observed for MOFs containing open metal sites, leads to high isosteric heats of adsorption (40–60 kJ mol^{-1}), which affords a potential energy penalty in the regeneration process.[9,10,20] The isosteric heat of adsorption for C_2H_2 in NOTT-300 decreases slightly initially from 32 to 30 kJ mol^{-1}, and increases slowly after 1.0 mmol g^{-1} loading to the original value of 32 kJ mol^{-1}. This suggests a cooperative binding mechanism, consistent with the INS/QENS study. In contrast, the isosteric heat of adsorption for C_2H_4 in NOTT-300 increases continuously over the whole range from initially 16 kJ mol^{-1} to 28 kJ mol^{-1} at 1.0 bar. This confirms the appearance of strong C_2H_4-C_2H_4 interactions (reminiscent of liquid ethylene) during the adsorption process, and the absence of strong C_2H_4-host interaction is consistent with its lower uptake and the INS/QENS studies. The moderate isosteric heat of adsorption in NOTT-300 [16–32 kJ mol^{-1} (Figure 1f)] confirms that the relatively weak supramolecular bonding interactions within this multiple functionalised host system are sufficiently strong to selectively recognise and bind guest molecules and induce a difference in their molecular motions, thus achieving the observed high selectivity and uptake capacity simultaneously.

Methods

Gas adsorption experiment: CH_4, C_2H_2, C_2H_4, and C_2H_6 sorption isotherms were recorded at 273-303 K on an IGA-003 system under ultra-high vacuum. CH_4, C_2H_4, and C_2H_6 gases used were ultra-pure research grade (99.99%). C_2H_2 was purified by dual-stage cold trap systems operated at 195 K (dry ice) before introduction to the IGA system. For the flow experiments, the flow rates, typically 25ml/min for each gas A and B, were controlled by two identical mass flow controllers and gas A and B were mixed in the pipe before introduction to the sample station, the volume of which is about 1.8 L. This was kept under a dynamic flow environment in order to maintain constant composition of mixture in the sample station throughout the experiment. Breakthrough experiments were carried out in a 7 mm diameter fixed bed tube of 130 mm length packed with ~3 g of NOTT-300 powder (particle size < 5 microns). The sample was heated at 100 ^{o}C under a flow of He overnight for complete activation. The fixed bed was then cooled to room temperature and the breakthrough experiment with an equimolar mixture of acetylene and ethylene was performed at atmospheric pressure and room temperature. The flow rate of the entering gas mixture was maintained at 2 ml min^{-1}, and the gas composition at outlet determined by mass spectrometry.

Neutron scattering experiment: INS, QENS and neutron powder diffraction experiments were carried out at the ISIS beamlines TOSCA, IRIS, and WISH, respectively. In a typical experiment, 2-5 g of desolvated NOTT-300 sample was used. The loading of gases was performed volumetrically at room temperature in order to ensure that gases were present in the gas phase when not adsorbed and also to ensure sufficient mobility of gases inside the crystalline structure of NOTT-300. It is important to note that the computations and modelling were performed simultaneously as the measurement of INS spectra. The result of the calculations allows us to identify the vibrational motions present in the experimental INS data immediately and in this way the INS experiment could be optimised rapidly and efficiently.

Structure determination of guest-loaded NOTT-300 from synchrotron X-ray and neutron powder diffraction experiment: The structure solutions were initially established by considering the structure of the bare NOTT-300 framework, and the residual electron density maps were further developed from subsequent difference Fourier analysis. The final structure

refinement of guest-loaded NOTT-300 was carried out using the Rietveld method with isotropic displacement parameters for all atoms. The final stage of the Rietveld refinement involved soft restraints to the C-C bond lengths within the benzene rings and carboxylate groups. Rigid body refinement was applied to define the molecular geometry for the hydrocarbon molecules in the pore. The details for the structural refinements are given in supplementary information.

Crystal data for NOTT-300·4C$_2$H$_2$: [Al$_2$(OH)$_2$(C$_{16}$H$_6$O$_8$)](C$_2$H$_2$)$_4$. White powder. Tetragonal, space group $I4_122$, $a = b = 14.82280(13)$, $c = 11.79190(10)$ Å, $V = 2590.86(5)$ Å^3, $M = 518.34$, $T = 273(2)$ K, $Z = 4$. The final Rietveld plot corresponds to satisfactory crystal structure model ($R_{Bragg} = 0.050$) and profile ($R_p = 0.056$ and $R_{wp} = 0.077$) indicators with a goodness-of-fit parameter of 1.73. Atomic fractional coordinates and relevant bond lengths for NOTT-300·4C$_2$H$_2$ are listed in Supplementary Table 1 and Table 2, respectively.

Crystal data for NOTT-300·2.5C$_2$H$_4$: [Al$_2$(OH)$_2$(C$_{16}$H$_6$O$_8$)](C$_2$H$_4$)$_{2.5}$. White powder. Tetragonal, space group $I4_122$, $a = b = 14.80469(3)$Å, $c = 11.80173(3)$Å, $V = 2586.69(1)$ Å^3, $M = 484.33$, $T = 273(2)$ K, $Z = 4$. The final Rietveld plot corresponds to satisfactory crystal structure model ($R_{Bragg} = 0.050$) and profile ($R_p = 0.059$ and $R_{wp} = 0.084$) indicators with a goodness-of-fit parameter of 2.74. Atomic fractional coordinates and relevant bond lengths for NOTT-300·2.5C$_2$H$_4$ are listed in Supplementary Table 3 and Table 4, respectively.

Crystal data for NOTT-300·2.7C$_2$D$_2$: [Al$_2$(OH)$_2$(C$_{16}$H$_6$O$_8$)](C$_2$D$_2$)$_{2.7}$. White powder. Tetragonal, space group $I4_122$, $a = b = 14.78536(8)$, $c = 11.77396(15)$ Å, $V = 2573.87(4)$ Å^3, $M = 489.90$, $T = 10(0.2)$ K, $Z = 4$. The final Rietveld plot corresponds to satisfactory crystal structure model ($R_{Bragg} = 0.006$) and profile ($R_p = 0.013$ and $R_{wp} = 0.014$) indicators with a goodness-of-fit parameter of 3.31. Atomic fractional coordinates and relevant bond lengths for NOTT-300·2.7C$_2$D$_2$ are listed in Supplementary Table 5 and 6, respectively.

Crystal data for NOTT-300·1.8C$_2$D$_4$: [Al$_2$(OH)$_2$(C$_{16}$H$_6$O$_8$)](C$_2$D$_4$)$_{1.8}$. White powder. Tetragonal, space group $I4_122$, $a = b = 14.79423(10)$, $c = 11.77851(18)$ Å, $V = 2577.95(5)$ Å^3, $M = 471.94$, $T = 10(0.2)$ K, $Z = 4$. The final Rietveld plot corresponds to satisfactory crystal structure model ($R_{Bragg} = 0.015$) and profile ($R_p = 0.015$ and $R_{wp} = 0.016$) indicators with a goodness-of-fit parameter of 3.83. Atomic fractional coordinates and relevant bond lengths for NOTT-300·2.7C$_2$D$_2$ are listed in Supplementary Table 7 and 8, respectively.

Crystal data for NOTT-300·1.3C$_2$D$_6$: [Al$_2$(OH)$_2$(C$_{16}$H$_6$O$_8$)](C$_2$D$_6$)$_{1.3}$. White powder. Tetragonal, space group $I4_122$, $a = b = 14.79549(11)$, $c = 11.77847(20)$ Å, $V = 2578.38(6)$ Å^3, $M = 461.15$, $T = 10(0.2)$ K, $Z = 4$. The final Rietveld plot corresponds to satisfactory crystal structure model ($R_{Bragg} = 0.014$) and profile ($R_p = 0.016$ and $R_{wp} = 0.018$) indicators with a goodness-of-fit parameter of 4.17. Atomic fractional coordinates and relevant bond lengths for NOTT-300·2.7C$_2$D$_2$ are listed in Supplementary Table 9 and 10, respectively.

References

1   Vaidhyanathan, R. *et al.* Direct observation and quantification of CO_2 binding within an amine-functionalized nanoporous solid. *Science* **330**, 650-653 (2010).
2   Rabone, J. *et al.* An adaptable peptide-based porous material. *Science* **329**, 1053-1057 (2010).
3   Long, J. R. & Yaghi, O. M. The pervasive chemistry of metal-organic frameworks. *Chem. Soc. Rev.* **38**, 1201-1507 (2009).
4   Zhou, H. C., Long, J. R. & Yaghi, O. M. Introduction to metal-organic frameworks. *Chem. Rev.* **112**, 673 (2012).
5   Davis, M. E. Ordered porous materials for emerging applications. *Nature* **417**, 813-821 (2002).
6   Yang, S. *et al.* A partially interpenetrated metal-organic framework for selective hysteretic sorption of carbon dioxide. *Nature Mater.* **11**, 710-716 (2012).
7   Yan, Y. *et al.* Metal-organic polyhedral frameworks: high H_2 adsorption capacities and neutron powder diffraction studies. *J. Am. Chem. Soc.* **132**, 4092-4094 (2010).
8   Lin, X. *et al.* High capacity hydrogen adsorption in Cu(II) tetracarboxylate framework materials: the role of pore size, ligand functionalization, and exposed metal sites. *J. Am. Chem. Soc.* **131**, 2159-2171 (2009).
9   Geier, S. J. *et al.* Selective adsorption of ethylene over ethane and propylene over propane in the metal-organic frameworks M_2(dobdc) (M = Mg, Mn, Fe, Co, Ni, Zn). *Chem. Sci.* **4**, 2054-2061 (2013).
10   Bloch, E. D. *et al.* Hydrocarbon separations in a metal-organic framework with open iron(II) coordination sites. *Science* **335**, 1606-1610 (2012).
11   Matsuda, R. *et al.* Highly controlled acetylene accommodation in a metal-organic microporous material. *Nature* **436**, 238-241 (2005).
12   Zhang, J. & Chen, X. Optimized acetylene/carbon dioxide sorption in a dynamic porous crystal. *J. Am. Chem. Soc.* **131**, 5516-5521 (2009).
13   Rowsell, J. L. C., Spencer, E. C., Eckert, J., Howard, J. A. K. & Yaghi, O. M. Gas adsorption sites in a large-pore metal-organic framework. *Science* **309**, 1350-1354 (2005).
14   Spencer, E. C., Howard, J. A. K., McIntyre, G. J., Rowsell, J. L. C. & Yaghi, O. M. Determination of the hydrogen absorption sites in Zn_4O(1,4-benzenedicarboxylate) by single crystal neutron diffraction. *Chem. Commun.*, 278-280 (2006).
15   Yang, S. *et al.* Selectivity and direct visualization of carbon dioxide and sulfur dioxide in a decorated porous host. *Nature Chem.* **4**, 887-894 (2012).
16   He, Y., Xiang, S. & Chen, B. A microporous hydrogen-bonded organic framework for highly selective C_2H_2/C_2H_4 separation at ambient temperature. *J. Am. Chem. Soc.* **133**, 14570-14573 (2011).
17   Xiang, S.-C. *et al.* Rationally tuned micropores within enantiopure metal-organic frameworks for highly selective separation of acetylene and ethylene. *Nat. Commun.* **2**, 204 (2011).
18   Li, B. *et al.* Introduction of π-complexation into porous aromatic framework for highly selective adsorption of ethylene over ethane. *J. Am. Chem. Soc.* **136**, 8654-8660 (2014).
19   Myers, A. L. & Prausnitz, J. M. Thermodynamics of mixed-gas adsorption. *AlChE J.* **11**, 121-127 (1965).
20   He, Y., Krishna, R. & Chen, B. Metal-organic frameworks with potential for energy-efficient adsorptive separation of light hydrocarbons. *Energy & Environ. Sci.* **5**, 9107-9120 (2012).
21   Anson, A., Wang, Y., Lin, C. C. H., Kuznicki, T. M. & Kuznicki, S. M. Adsorption of ethane and ethylene on modified ETS-10. *Chem. Eng. Sci.* **63**, 4171-4175 (2008).
22   Bae, Y.-S. *et al.* High propene/propane selectivity in isostructural metal–organic frameworks with high densities of open metal sites. *Angew. Chem. Int. Ed.* **51**, 1857-1860 (2012).
23   Peralta, D. *et al.* Comparison of the behavior of metal¬organic frameworks and zeolites for hydrocarbon separations. *J. Am. Chem. Soc.* **134**, 8115-8126 (2012).
24   Ramirez-Cuesta, A. J. aCLIMAX 4.0.1, The new version of the software for analyzing and interpreting INS spectra. *Comput. Phys. Commun.* **157**, 226-238 (2004).
25   Clark, S. J. *et al.* First principles methods using CASTEP. *Z. Kristall.* **220**, 567-570 (2005).
26   Refson, K., Tulip, P. R. & Clark, S. J. Variational density-functional perturbation theory for dielectrics and lattice dynamics. *Physical Review B* **73** (2006).
27   Boscoboinik, J. A. *et al.* Interaction of probe molecules with bridging hydroxyls of two-dimensional zeolites: a surface science approach. *J. Phys. Chem. C* **117**, 13547-13556 (2013).
28   Jobic, H. & Theodorou, D. N. Quasi-elastic neutron scattering and molecular dynamics simulation as complementary techniques for studying diffusion in zeolites. *Microporous Mesoporous Mater.* **102**, 21-50 (2007).
29   Rives, S. *et al.* Diffusion of xylene isomers in the MIL-47(V) MOF material: a synergic combination of computational and experimental tools. *J. Phys. Chem. C* **117**, 6293-6302 (2013).
30   Salles, F. *et al.* Diffusion of binary CO_2/CH_4 mixtures in the MIL-47(V) and MIL-53(Cr) metal¬organic framework type solids: a combination of neutron scattering measurements and molecular dynamics simulations. *J. Phys. Chem. C* **117**, 11275-11284 (2013).

Author Contributions

SY and RN: syntheses, characterisation of MOF samples, measurements and analysis of adsorption isotherms. SY, SKC and CCT: collection and analysis of synchrotron X-ray powder diffraction data. SY, AJRC, RN, VGS, PM, SKC and SIC: collection, analysis, refinement and DFT modelling of neutron scattering data. SY and MS: overall direction of project and preparation of the manuscript.

Additional information

Supplementary information is available in the online version of the paper. Reprints and permissions information is available online at www.nature.com/reprints. Correspondence and requests for materials should be addressed to S.Y. and M.S.

Competing financial interests

The authors declare no competing financial interests.

Figures and Legends
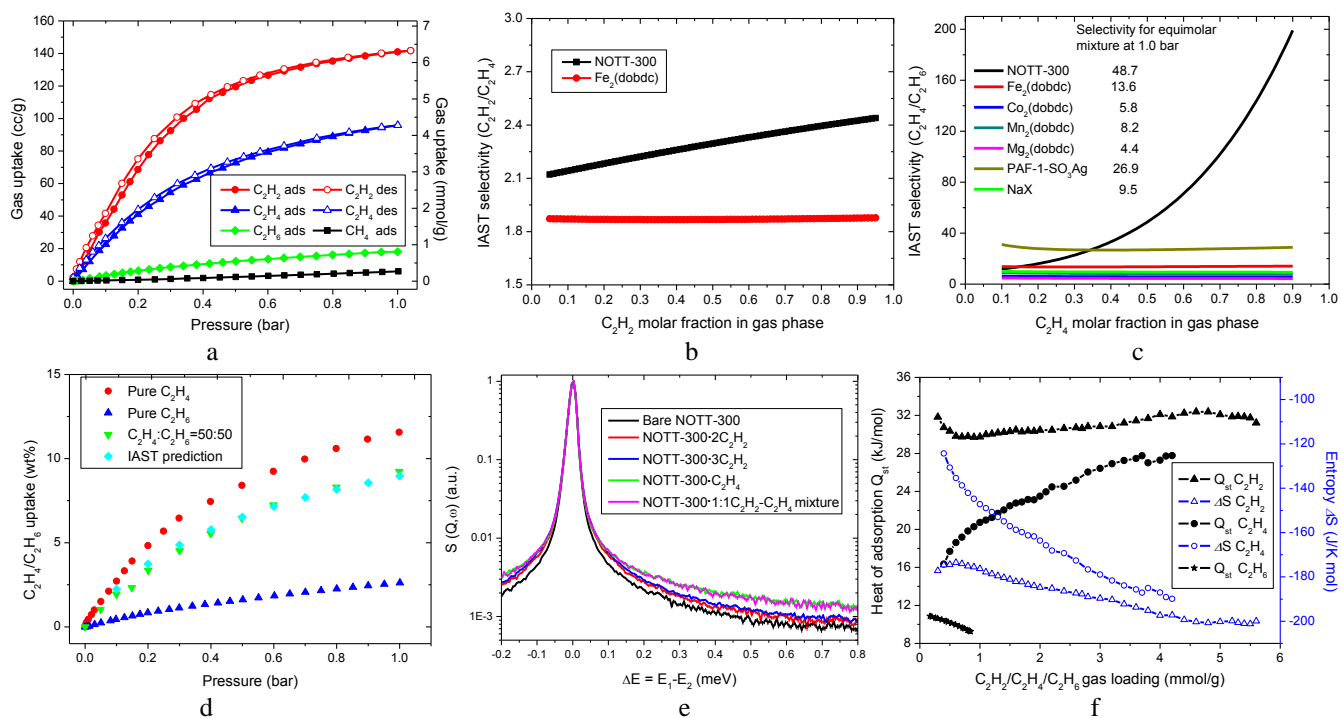
Figure 1. Hydrocarbon adsorption isotherms and selectivity data for NOTT-300, QENS spectra, and variation of thermodynamic parameters for hydrocarbon adsorption in NOTT-300. (a) Adsorption isotherms of C_2H_2, C_2H_4, C_2H_6, and CH_4 in NOTT-300 at 293 K; data at other temperatures are shown in supplementary information. Comparison of IAST selectivities for equimolar mixtures of (b) C_2H_2/C_2H_4 and (c) C_2H_4/C_2H_6 of varying compositions at 1.0 bar for NOTT-300 and the state-of-the-art porous materials.[9,10,18,20-22] The IAST selectivities of equimolar mixture of C_2H_2/C_2H_4 for NOTT-300 and Fe_2(dobdc) are 2.30 and 1.87, respectively. (d) Comparison of the adsorption isotherms for C_2H_4, C_2H_6, and an equimolar mixture of C_2H_4-C_2H_6 at 293 K in NOTT-300. Data were measured in flow mode. Prediction from the IAST calculation is shown in cyan. (e) QENS spectra for bare NOTT-300, NOTT-300·$2C_2H_2$, NOTT-300·$3C_2H_2$, NOTT-300·C_2H_4, and NOTT-300·1:$1C_2H_2$-C_2H_4 at 293 K. (f) Variation of the thermodynamic parameters of isosteric heat of adsorption (Q_{st}) and entropy ($\varDelta S$) for C_2H_2, C_2H_4 and C_2H_6 uptakes in NOTT-300. The values of Q_{st} for C_2H_2 uptake lies in the range 30–32 kJ mol^{-1} and do not vary much with increased C_2H_2 loading. In contrast, values of Q_{st} for C_2H_4 uptake lie in the range 16–28 kJ mol^{-1} and increase with increased C_2H_4 loading, indicating the presence of a strong C_2H_4-C_2H_4 interaction. Overall, $\varDelta S$ decreases with increasing surface coverage over the whole loading range for both C_2H_2 and C_2H_4. Q_{st} of C_2H_6 adsorption is subject to uncertainties due to the low isotherm uptake.
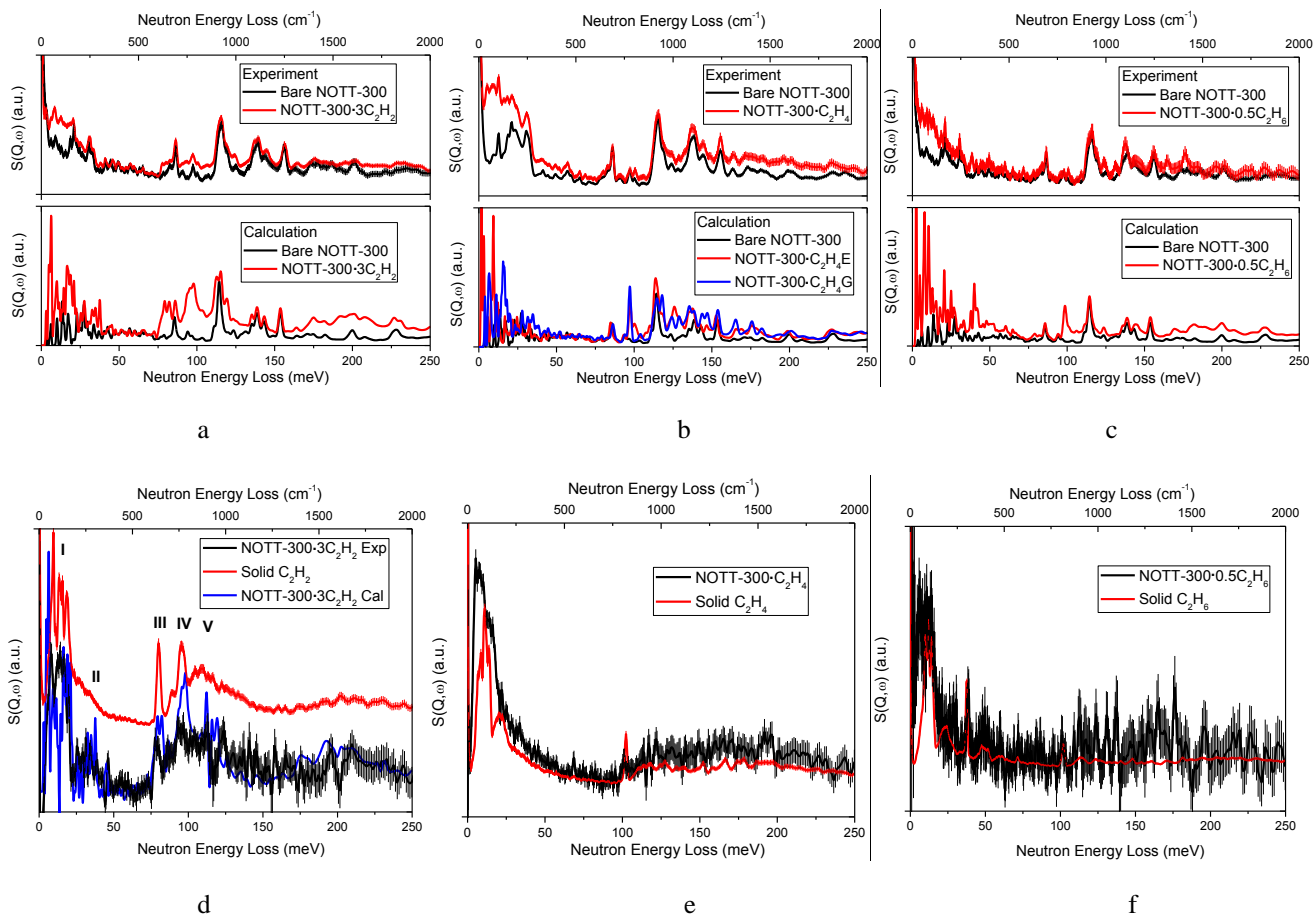
Figure 2. Inelastic neutron scattering (INS) spectra for NOTT-300 as a function of hydrocarbon loadings. Comparison of the experimental (top) and DFT calculated (bottom) INS spectra for bare NOTT-300 and the (a) C_2H_2, (b) C_2H_4 and (c) C_2H_6-loaded NOTT-300. Comparison of the difference plots for experimental INS spectra of bare NOTT-300 and the (d) C_2H_2, (e) C_2H_4 and (f) C_2H_6-loaded NOTT-300, and the experimental INS spectra of condensed (d) C_2H_2, (e) C_2H_4 and (f) C_2H_6 in the solid state. A difference plot for DFT calculated INS spectra of bare and the C_2H_2-loaded NOTT-300 is shown in (d), confirming good agreement with the experimental difference INS spectra. Due to the strong rotational recoil motion of adsorbed C_2H_4 and C_2H_6 molecules, and the lack the resolved energy transfer peaks, the corresponding difference plots for solid-state DFT calculations are not shown here. In the DFT calculation of NOTT-300·C_2H_4, two models with different orientation of adsorbed C_2H_4 molecules were found. NOTT-300·C_2H_4G and NOTT-300·C_2H_4E in (b) represent the "ground-state" and "excited-state" structural models, respectively. Peaks I, III and IV in (d) are assigned to translational, symmetric and asymmetric C-H vibrational motions of adsorbed C_2H_2 molecules, respectively. Peaks II and V in (d) are assigned to the bending/wagging motions of the –OH groups and four aromatic C-H groups on two benzene rings, respectively.
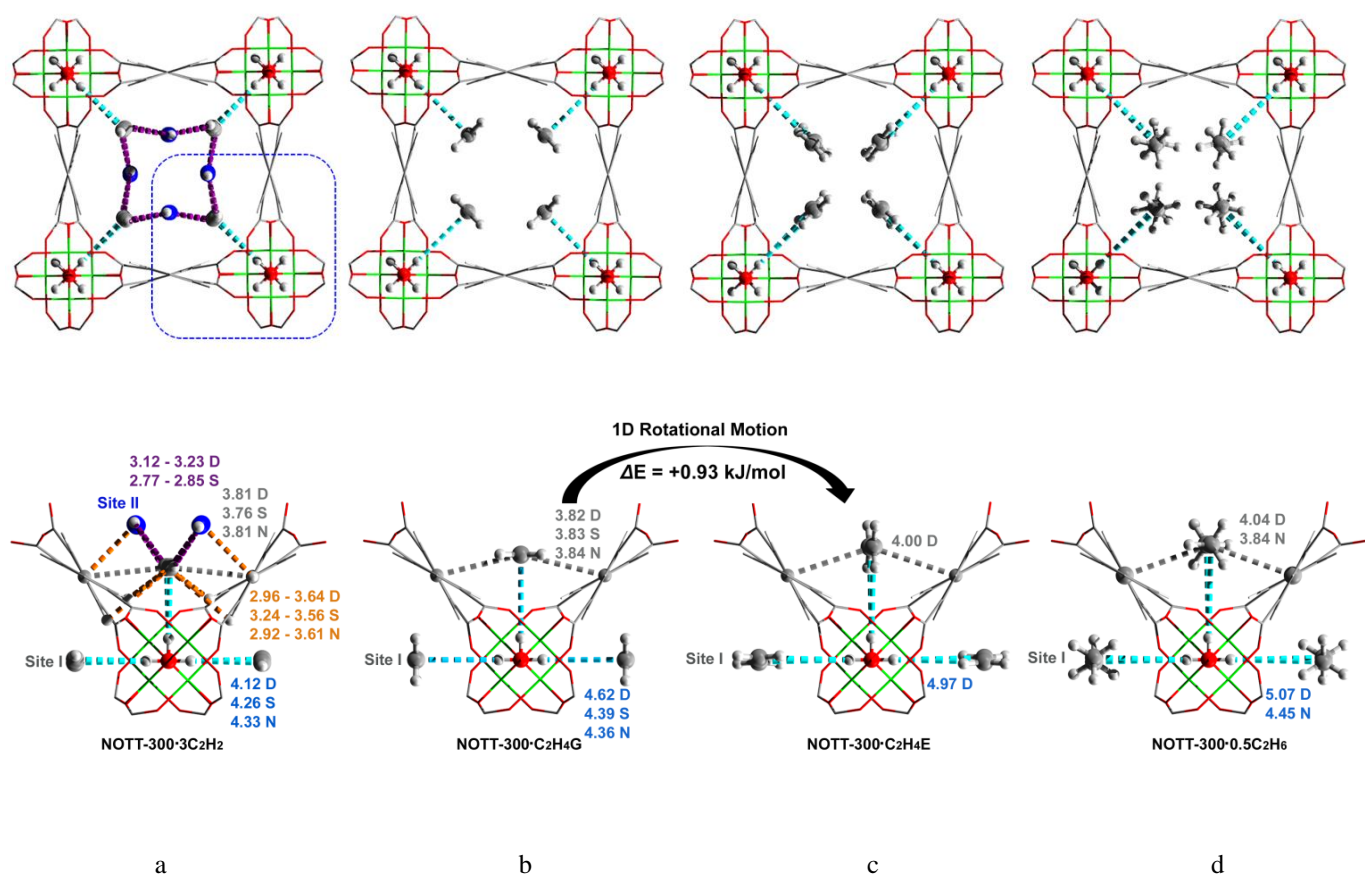
Figure 3. Views of the structural models for (a) NOTT-300·3C$_2$H$_2$, (b) NOTT-300·C$_2$H$_4$G, (c) NOTT-300·C$_2$H$_4$E and (d) NOTT-300·C$_2$H$_6$ (Al: green; carbon: grey; oxygen: red; hydrogen: white). These models were generated from DFT optimisations based upon the structural analyses obtained from synchrotron and neutron powder diffraction experiments. The details of the host-guest binding as shown in the blue square are enlarged and shown in the bottom row for each of the corresponding model. Hydrocarbon molecules in the channel and the host functional groups involved in cooperative binding are highlighted by the use of ball-and-stick mode. The $\pi\cdots$HO hydrogen-bonds, $\pi\cdots\pi$ stacking, C$\cdots$H supramolecular interactions, and inter-molecular dipole interactions are highlighted in cyan, grey, orange, and purple, respectively. The carbon atoms of second site of C$_2$H$_2$ are highlighted in blue. Sites I and II represent two preferred binding sites within the pore: molecules at Site I interacts with the Al-OH groups and those at Site II bind primarily with molecules at Site I via dipole interactions. The energy barrier for 1D rotational motion between NOTT-300·C$_2$H$_4$G and NOTT-300·C$_2$H$_4$E was estimated to be 0.93 kJ mol^{-1}. The bond distances obtained from DFT calculations, synchrotron X-ray diffraction and from neutron diffraction experiments are labelled as D, S and N, respectively, and are shown in Å. Throughout this report, the uncertainties for the bond distance obtained from synchrotron X-ray diffraction and neutron diffraction experiments are below 0.01 and 0.02 Å, respectively. To simplify the positional disorder of the guest molecules owing to the thermal motion, optimised models from calculations are shown here for clarity, and disordered models are shown in supplementary information. Due to the uncertainty of the hydrogen atom location, the $\pi\cdots$HO hydrogen-bonds are described *via* the distance between the O-centre and the centroid of the C$_2$ bond of hydrocarbon molecules.
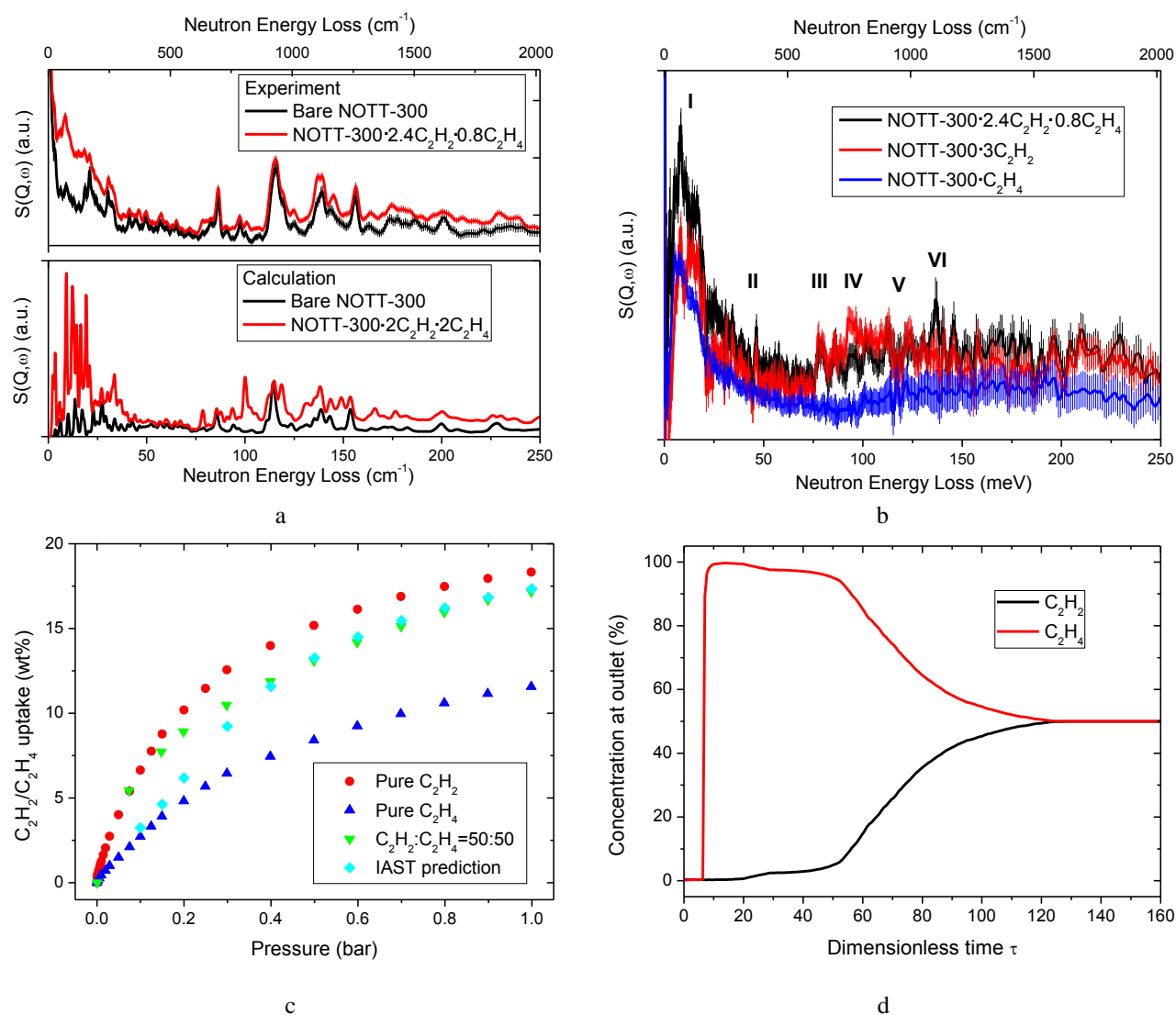
Figure 4. Inelastic neutron scattering (INS) spectra for C₂H₂-C₂H₄ hydrocarbon-mixture-loaded NOTT-300 and views of the C₂H₂-C₂H₄ mixture adsorption isotherm and the corresponding breakthrough plot. (a) Comparison of the experimental (top) and DFT calculated (bottom) INS spectra for bare and 1:1 C₂H₂-C₂H₄ loaded NOTT-300. (b) Comparison of the difference plots for experimental INS spectra of bare NOTT-300 and C₂H₂, C₂H₄, and 1:1 C₂H₂:C₂H₄-loaded NOTT-300. Peaks I, III and IV are assigned to translational, symmetric and asymmetric C-H vibrational motions of adsorbed C₂H₂ molecules, respectively. Translational motion from adsorbed C₂H₄ molecules also contribute to the increased intensity in Peak I. Peaks II, V and VI are assigned to the bending/wagging motions of the –OH groups and the aromatic C-H groups on two benzene rings, respectively. (c) Comparison of the adsorption isotherms for C₂H₂, C₂H₄, and an equimolar mixture of C₂H₂/C₂H₄ at 293 K in NOTT-300. Data were measured in flow mode. Prediction from the IAST calculation is shown in cyan. (d) Experimental breakthrough plots for an equimolar mixture of C₂H₂-C₂H₄ in a fixed bed packed with NOTT-300 measured at 293 K and 1.0 bar. Dimensionless time, τ, is calculated by equation $\tau = tu/\varepsilon L$, where t, u, ε and L represent the actual time, superficial gas velocity, the fractional porosity of the fixed bed, and bed length, respectively. The details of the calculations are shown in Supplementary Information.
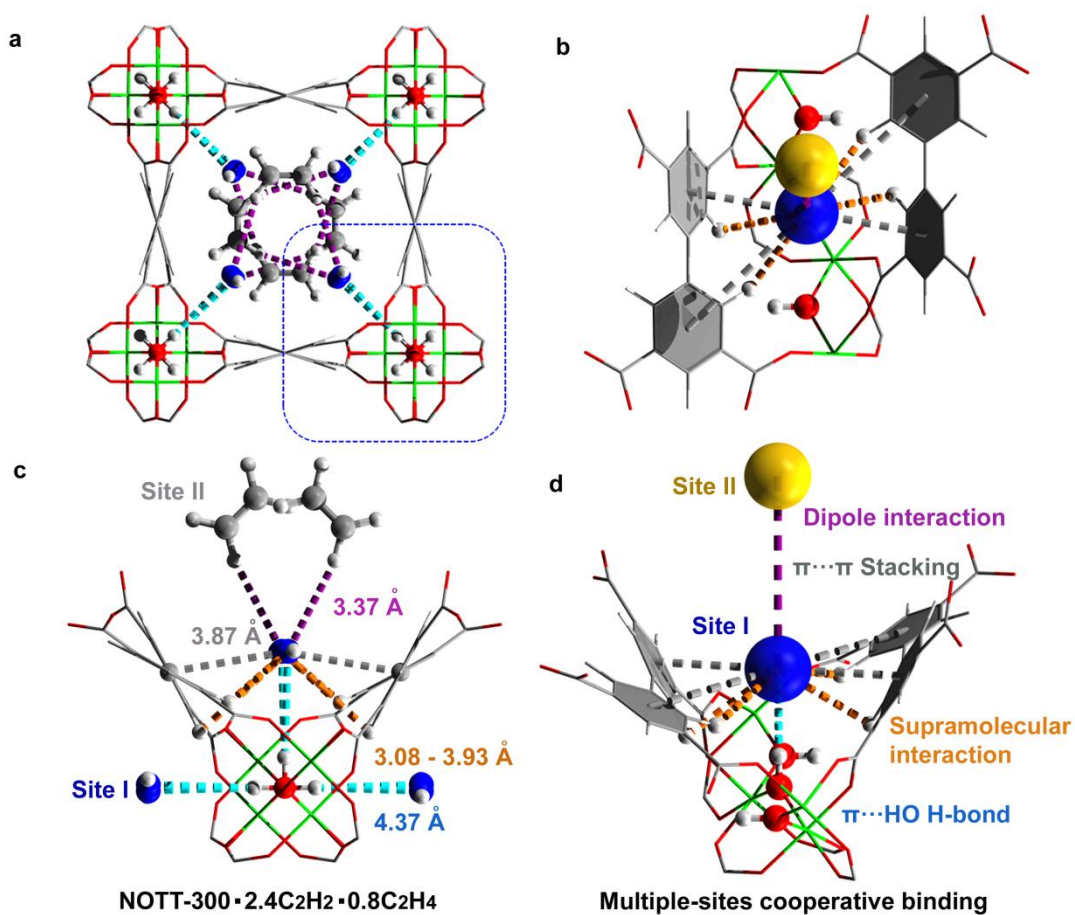
Figure 5. Views of the calculated structural models for C_2H_2-C_2H_4 mixture-loaded NOTT-300 (NOTT-300·2.4C_2H_2·0.8C_2H_4) (Al: green; carbon: grey; oxygen: red; hydrogen: white). (a,c) Views of the structure of NOTT-300·2.4C_2H_2·0.8C_2H_4 obtained from DFT calculations based upon INS spectra. The details of the host-guest binding as shown in the blue square are enlarged and shown in (c). The bond distances were obtained from DFT optimisation. The adsorbed C_2H_2 and C_2H_4 molecules in the pore are highlighted by the use of ball-and-stick mode. The carbon atoms of C_2H_2 are highlighted in blue. Discussion on the structural models obtained from corresponding neutron powder diffraction experiments of C_2D_2-C_2D_4 mixture-loaded NOTT-300 is given in Supplementary Information. (b,d) Schematic view of the role of the –OH, -CH and phenyl ring groups in binding C_2H_2 and C_2H_4 molecules in a "pocket-like" cavity. Sites I and II represent two preferred binding sites within the pore, and are shown by blue and yellow balls, respectively. The $\pi\cdots$HO hydrogen-bonds, $\pi\cdots\pi$ stacking, C$\cdots$H supramolecular interactions, and inter-molecular dipole interactions are highlighted in cyan, grey, orange, and purple, respectively.

18

Table 1. Summary of the adsorption uptakes, selectivities and heat of adsorption data for C_2H_2, C_2H_4, C_2H_6, and CH_4 in [Fe$_2$(dobdc)],[9,10] M'MOF-3a,[17] PAF-1-SO$_3$Ag,[18] and NOTT-300. The selectivity data calculated from IAST analysis and by the direct comparison of the corresponding isotherm uptakes have consistent trends. [Fe$_2$(dobdc)] and PAF-1-SO$_3$Ag exhibit high isosteric heat of adsorption for unsaturated hydrocarbons owing the formation of π complexation between the open metal sites (*i.e.*, Fe^{2+}, Ag^+) and π electrons of the hydrocarbons. In contrast, NOTT-300 shows a significant difference in isosteric heat of adsorption for C_2H_2 and C_2H_4 since the selective binding in NOTT-300 is achieved *via* formation of a combination of weak supramolecular interactions, which are sensitive the number of π electrons of the guest molecule.

	[Fe$_2$(dobdc)]	M'MOF-3a	PAF-1-SO$_3$Ag	NOTT-300
Surface area ($m^2\,g^{-1}$)	1350	551	783	1370
Pore Volume ($cc\,g^{-1}$)	0.626	0.164	0.309	0.433
Size of pore window (Å)	11 x 11	4 x 9	~8	6.5 x 6.5
C_2H_2 uptake at 1.0 bar ($mmol\,g^{-1}$)	6.8[a]	1.9[b]	-	6.34[d]
C_2H_4 uptake at 1.0 bar ($mmol\,g^{-1}$)	6.1[a]	0.4[b]	4.06[c]	4.28[d]
C_2H_6 uptake at 1.0 bar ($mmol\,g^{-1}$)	5.0[a]	-	2.23[c]	0.85[d]
CH_4 uptake at 1.0 bar ($mmol\,g^{-1}$)	0.8[a]	-	-	0.29[d]
C_2H_2/C_2H_4 uptake ratio[e]	1.11	4.75	-	1.48
C_2H_4/C_2H_6 uptake ratio[e]	1.22	-	1.82	5.03
C_2H_6/CH_4 uptake ratio[e]	6.25	-	-	2.93
Selectivity for C_2H_2/C_2H_4	1.87[f]	5.23[g]	-	2.30[f]
Selectivity for C_2H_4/C_2H_6	13.6[f]	-	26.9[f]	48.7[f]
Selectivity for C_2H_6/CH_4	~35[f]	-	-	~5.1[f]
Isosteric heat of adsorption (C_2H_2)[h] ($kJ\,mol^{-1}$)	-47	-27.1	-	-32
Isosteric heat of adsorption (C_2H_4)[h] ($kJ\,mol^{-1}$)	-45	-27.4	-106	-16
Isosteric heat of adsorption (C_2H_6)[h] ($kJ\,mol^{-1}$)	-25	-	-27	-11
Isosteric heat of adsorption (CH_4)[h] ($kJ\,mol^{-1}$)	-20	-	-	n.a.[i]

[a] at 318 K, moderately larger uptakes are expected for isotherms measured at lower temperatures; [b] at 295 K, [c] at 296 K, [d] at 293 K, [e] for ratios of the total uptake capacities at 1.0 bar; [f] IAST analysis for an equimolar mixture at 1.0 bar; [g] ratio of Henry's constants; [h] Q_{st} values at low surface coverage; [i] due to the very low uptake, it was unable to determine the heat of adsorption accurately.

TOC (50 words):

The molecular details of cooperative binding at multiple sites have been elucidated in a complex host-guest system (NOTT-300) which is capable of separating C_1 and C_2 hydrocarbons under ambient conditions based upon the intelligent recognition of different hydrocarbon molecules.

Supramolecular host-guest system   Multiple-sites cooperative binding
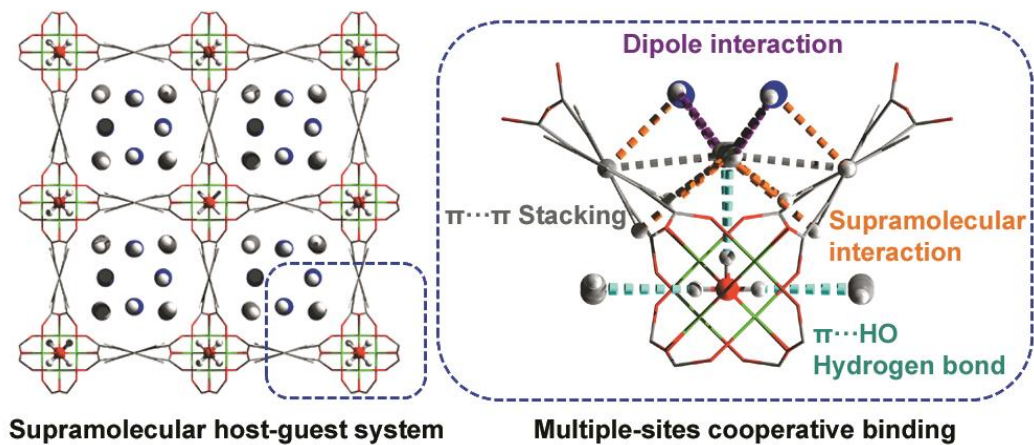
Supplementary Information

Supramolecular Binding and Separation of Hydrocarbons within a Functionalised Porous Metal-Organic Framework

Sihai Yang,[1]* Anibal J. Ramirez-Cuesta,[2] Ruth Newby,[1] Victoria Garcia-Sakai,[3] Pascal Manuel,[3] Samantha K. Callear,[3] Stuart I. Campbell,[4] Chiu C. Tang[5] and Martin Schröder[1]*

[1] School of Chemistry, University of Nottingham, University Park, Nottingham, NG7 2RD (UK)

   Fax: +44 115 951 3563 E-mail: Sihai.Yang@nottingham.ac.uk; M.Schroder@nottingham.ac.uk

[2] The Chemical and Engineering Materials Division (CEMD), Neutron Sciences Directorate, Oak Ridge National Laboratory, Oak Ridge, TN 37831 (USA)

[3] ISIS Neutron Facility, STFC Rutherford Appleton Laboratory, Chilton, Oxfordshire, OX11 0QX (UK)

[4] Neutron Data Analysis and Visualization Division (NDAV), Neutron Sciences Directorate, Oak Ridge National Laboratory, Oak Ridge, TN 37831 (USA)

[5] Diamond Light Source, Harwell Science and Innovation Campus, Didcot, Oxfordshire, OX11 0DE (UK)

Index of Supplementary Information

1. Experimental Section

1.1 Synthesis and Activation of NOTT-300

All reagents were used as received from commercial suppliers without further purification. Synthesis of $[Al_2(OH)_2(C_{16}O_8H_6)](H_2O)_6$ (NOTT-300-solvate) and activation of $[Al_2(OH)_2(C_{16}O_8H_6)]$ (NOTT-300) were carried out using our previously reported method.[1]

1.2 Gas Adsorption Isotherms

CH_4, C_2H_2, C_2H_4, and C_2H_6 sorption isotherms were recorded at 273-303 K using a temperature programmed water bath on an IGA-003 system (Hiden) at the University of Nottingham under ultra-high vacuum from a diaphragm and turbo pumping system. CH_4, C_2H_4, and C_2H_6 gases used were ultra-pure research grade (99.99%) purchased from BOC or AIRLIQUIDE. C_2H_2 was purified by dual-stage cold trap systems operated at 195 K (dry ice) and an activated carbon filter before introduction to the IGA system. In a typical gas adsorption experiment, 50-100 mg of NOTT-300-solvate was loaded into the IGA, and degassed at 120 $^{\circ}$C and high vacuum (10^{-10} bar) for 1 day to give fully desolvated NOTT-300. For flow experiments, the flow rates, typically 25ml/min for each gas A and B, were controlled by two identical mass flow controllers. Gas A and B were thoroughly mixed before introduction to the sample station thus maintaining a constant mixture composition throughout the whole experiment.

Breakthrough experiments were carried out in a 7 mm diameter fixed bed tube of 130 mm length packed with ~3 g of NOTT-300 powder (particle size < 5 microns). The total volume of the bed was 5 cm^3. The sample was heated at 100 $^{\circ}$C under a flow of He overnight for complete activation. The fixed bed was then cooled to room temperature using a temperature programmed water bath and the breakthrough experiment was performed with an equimolar mixture of acetylene and ethylene at atmospheric pressure and room temperature. The flow rate of the entering gas mixture was maintained at 2 ml/min, and the gas composition at outlet determined by mass spectrometry.

1.3 Inelastic Neutron Scattering (INS)

INS spectra were recorded on the TOSCA spectrometer at the ISIS Facility at the Rutherford Appleton Laboratory (UK) for energy transfers between ~-2 and 500 meV. In this region TOSCA has a resolution of 1.5% $\Delta E/E$. The sample of desolvated NOTT-300 was loaded into a cylindrical vanadium sample container with an indium vacuum seal and connected to a gas handling system. The sample was degassed at 10^{-7} mbar and 120 $^{\circ}$C for 1 day to remove any remaining trace guest water molecules. The temperature during data collection was controlled using a closed cycle refrigerator (CCR) cryostat (7 ± 0.1 K). The loading of C_2H_2, C_2H_4, and C_2H_6 was performed

volumetrically at room temperature to ensure that C_2H_2, C_2H_4, and C_2H_6 were present in the gas phase when not adsorbed and also to ensure sufficient mobility of C_2H_2, C_2H_4, and C_2H_6 inside the crystalline structure of NOTT-300. Subsequently, the temperature was lowered to below 10 K for scattering measurements to ensure minimum achievable thermal motion of the framework host and adsorbed C_2H_2, C_2H_4, and C_2H_6 molecules. Background spectra (sample can plus NOTT-300) were subtracted to obtain the difference spectra. INS spectra for condensed C_2H_2, C_2H_4, and C_2H_6 in the solid state were measured by using a plate sample container. Approximately 1-2 L of each gas at room temperature was condensed slowly at temperatures below their melting points and cooled to temperature below 10 K for neutron scattering measurements.

The equimolar mixture of C_2H_2/C_2H_4 was prepared externally prior to the dosing. Equal amounts of C_2H_2 and C_2H_4 gas were introduced into the fixed volume vessel at a pressure of 1.0 bar at room temperature. The vessel was left sealed at room temperature for 3 h to allow mixing of the gases. The vessel was then opened to the sample cell (minimal dead cell volume) which was under vacuum, and the connection left open for 3 h to allow full adsorption into desolvated NOTT-300. The sample cell was isolated and sealed at room temperature, and adsorption equilibrium was achieved when the rate of pressure drop was below 0.1 mbar over 20 min. The sealed sample cell was then cooled to ~7 K over a 2 h period with a three-head Closed Cycle Refrigerators (CCR) controller and neutron data collection was then initiated. The initial cooling from RT to ~200 K was less than 20 min and further cooling is slower. The isolation of the sample cell before cooling is essential to prevent condensation of free hydrocarbon molecules from the vessel volume into the sample cell, since this will lead to a broad recoil motion in the background of the spectra. Major re-arrangement of hydrocarbon molecules within the pores of NOTT-300 on rapid reduction of temperature is not expected since (i) the adsorption equilibrium was achieved at room temperature; (ii) the cell was isolated before cooling and no additional gas was available to be adsorbed; (iii) the initial cooling (down to near the boiling point) was very rapid to ensure strong barriers to diffusion, *i.e.,* the guest molecules will have little mobility at temperatures near 200 K.

INS was used to study the binding interaction and structure dynamics in this case, because it has several unique advantages:

- INS spectroscopy is ultra-sensitive to the vibrations of hydrogen atoms, and hydrogen is ten times more visible than other elements due to its high neutron cross-section.
- The technique is not subject to any optical selection rules. All vibrations are active and, in principle, measurable.
- INS observations are not restricted to the centre of the Brillouin zone (gamma point) as is the case for optical techniques.

- INS spectra can be readily and accurately modelled: the intensities are proportional to the concentration of elements in the sample and their cross-sections, and the measured INS intensities relate straightforwardly to the associated displacements of the scattering atom. Treatment of background correction is also straightforward.

- Neutrons penetrate deeply into materials and pass readily through the walls of metal containers making neutrons ideal to measure bulk properties of this material.

- INS spectrometers cover the whole range of the molecular vibrational spectrum, 0-500 meV (0-4000 cm^{-1})

- INS data can be collected at below 10 K, where the thermal motion of the MOF material and adsorbed C_2H_2, C_2H_4, and C_2H_6 molecules can be significantly reduced.

- Calculation of the INS spectra from DFT vibrational analysis can be readily achieved, and DFT calculations relate directly to the INS spectra, and, in the case of solid state calculations, there are no approximations other than the use of DFT eigenvectors and eigenvalues to determine the spectral intensities.

It is important to note that the computations and modelling were performed simultaneously as the measurement of INS spectra. The result of the calculations allows us to identify the vibrational motions present in the experimental INS data immediately and in this way the INS experiment can be optimised rapidly and efficiently.

1.4 DFT Modelling and Simulations

The vibrational properties of NOTT-300 were calculated using a combination of density functional theory (DFT) and plane-wave pseudopotential methods as implemented in the CASTEP code[2] using ultra-soft pseudopotentials with a plane-wave energy cut-off of 380 eV. Calculations were performed under the PBE approximation[3] for exchange and correlation. The wave functions were sampled according to the Monkhorst-Pack scheme with a k-points mesh of spacing ~0.05 Å^{-1}. The normal modes of the solid were determined from dynamical matrices calculated using finite displacements, by numerical differentiation. The INS spectra were calculated using the aClimax software.[4] Calcutions with and without van der Waals corrections were carried out separately to study their effect on the vibrational properties of solids.

1.5 Quasi-elastic Neutron Scattering (QENS)

Quasi-elastic neutron scattering (QENS) provides a means to probe motions in the ps-ns timescale of molecules and has been used extensively to interrogate diffusion processes in confined systems.[5] QENS spectra were recorded on the IRIS spectrometer at the ISIS Facility at the Rutherford Appleton Laboratory (UK). IRIS is an inverted geometry spectrometer which analyses the final energy of neutrons *via* crystals of pyrolitic graphite. The PG002 reflection affords an energy resolution of 17.5ueV and the choppers were phased to look at an energy

window of -0.2 to 1.2meV. The detector coverage on the spectrometer is such that at these energies we can probe a momentum transfer range of 0.4-1.8Å^{-1}. The sample of desolvated NOTT-300 was loaded into an annular aluminium sample container (0.5 mm gap to avoid multiple scattering effects) with an indium vacuum seal and connected to a gas handling system. The sample was degassed at 10^{-7} mbar and 120 °C for 1 day to remove any remaining trace guest water molecules. The temperature during data collection was controlled using a top-loading closed-cycle refrigerator (± 0.2 K). The loadings of C_2H_2 and C_2H_4 were performed volumetrically at room temperature to ensure that C_2H_2 and C_2H_4 were present in the gas phase when not adsorbed and also to ensure sufficient mobility of C_2H_2 and C_2H_4 inside the crystalline structure of NOTT-300. Subsequently, QENS spectra were collected at temperatures in the range 5-293 K for the bare NOTT-300 and NOTT-300 loaded with C_2H_2, C_2H_4 and an equimolar mixture. In this preliminary analysis of the data, all spectra were added together and motions are assumed to be of localised nature such that there is no Q-dependence. This appears likely for the adsorbed C_2H_2 modes but may not be the case for adsorbed C_2H_4. However the main observations described in what follows are still valid. A full analysis of the QENS data will be reported in a separate publication to obtain an accurate description of the dynamic modes. In the figures the data have been normalised so that any changes in broadening can be seen more clearly.

The QENS data at each temperature for bare NOTT-300 was fitted to a simple Lorentzian convolution with a delta and resolution function (measured at 5 K), plus a flat background contribution. The full-width at half maximum of the Lorentzian (*Gamma*) was plotted as a function of temperature yielding Arrhenius behaviour. The activation energy is extracted as the slope from the linear fitting by Arrhenius equation (1).

$$E_a = -R(\frac{\partial \ln(Gamma)}{\partial(1/T)})_p \qquad (1)$$

where *R* is the gas constant, and *T* is temperature. This QENS broadening increases steadily with temperature and fitting the data to a Lorentzian and sequentially Arrhenius function gives an energy (E_a) of 3.2 kJ mol^{-1} for the activation of the free hydroxyl groups.

1.6   High Resolution Synchrotron X-ray Powder Diffraction and Structure Determinations

High resolution *in situ* synchrotron X-ray powder diffraction (PXRD) data were collected at Beamline I11 of Diamond Light Source using multi-analysing crystal-detectors (MACs)[6] and monochromated radiation [λ = 0.826126(2) Å]. These *in situ* diffraction measurements were carried out in capillary mode and the temperature controlled by an Oxford Cryosystems open-flow nitrogen gas cryostat. In a typical experiment, the powder sample of NOTT-300 (~2-4 mg) was dried in air and ground for 10 min before loading into a capillary tube (0.7 mm diameter). Grinding provides a uniform and small (below 10 micron) particle size essential for obtaining high-

quality X-ray patterns. The capillary tube was connected to a high vacuum line (10^{-6} mbar) and heated at 140 $^{\circ}$C for ~2 hour to generate the fully desolvated NOTT-300 material. For each C_2H_2 and C_2H_4 pressure step, the loaded sample was left for ~30-60 minutes to equilibrate before collection of the PXRD pattern. The final PXRD pattern was collected after a final degassing at 373 K and under vacuum for ~40 minute to remove adsorbed C_2H_2 and C_2H_4. Upon desolvation and removal of C_2H_2 and C_2H_4, we observe neither major changes to cell parameters nor extra features in the patterns, suggesting that there is no structural phase change during the experiment.

The structure solutions were initially established by considering the structure of the bare NOTT-300 framework, and the residual electron density maps were further developed from subsequent difference Fourier analysis using TOPAS. The final structure refinement of NOTT-300·$4C_2H_2$ was carried out using the Rietveld method[7] with isotropic displacement parameters for all atoms. Upon loadings with hydrocarbon, there are apparent changes in the Bragg peak intensities indicating that the hydrocarbon molecules are adsorbed into the bare material. Refinement of the occupancy of the adsorption sites for the C_2H_2 loaded NOTT-300 showed both of the sites to be fully occupied by C_2H_2 molecules, slightly higher than the experimental value (~75% occupied). On loading with C_2H_4, the occupancy of the first C_2H_4 site was determined to be 0.706(6) and the second C_2H_4 site 0.560(4), leading to a total refined C_2H_4 stoichiometry of 1.266(10) C_2H_4 per Al in excellent agreement with the experimental value of 1.1 C_2H_4 per Al. The final stage of the Rietveld refinement involved soft restraints to the C-C bond lengths within the benzene rings and carboxylate groups. Rigid body refinement was applied to define the molecular geometry for both the C_2H_2 and C_2H_4 molecules in the pore, whereby the C-C and C-H bond lengths obtained from CCDC crystallographic data of the pure C_2H_2, C_2H_4 and C_2H_6 forms were used. No restraints were used in the position or orientation of the molecules within the pore. Both molecules were located at general positions, and as a result positional disorder of the molecules was observed. A global isotropic thermal parameter was refined for the gas molecules, and the occupancies of the gas molecules were also refined. Hydrogen atoms were included on both molecules in the final refinement in accordance with geometrical constraints, although their precise location could not be obtained from these data. In the case of NOTT-300·$4C_2H_2$, the hydrogen atoms can be defined due to the linear geometry of the C_2H_2 molecule. In the case of NOTT-300·$2.5C_2H_4$, precise location of hydrogen atoms cannot be determined due to the additional rotational freedom along the C-C bond of the C_2H_4 molecules and refinements with different C_2H_4 orientation yield similar R factors. In the final model, the average orientation of the C_2H_4 molecules (half way in between NOTT-300·$1C_2H_4G$ and NOTT-300·$1C_2H_4E$) was used.

1.7 Neutron Powder Diffraction (NPD) and Structure Determinations

WISH is a long wavelength powder and single crystal neutron diffractometer at the ISIS Facility at the Rutherford Appleton Laboratory (UK).[8] The instrument views a solid methane moderator providing a high flux of

cold neutrons with a large bandwidth, transported to the sample *via* an elliptical guide. The WISH divergence jaws system allows the experimentalists to tune the resolution according to the need of the experiment; in this case, it was setup in high resolution mode. The WISH detectors are 1m long, 8mm diameter pixellated 3He tubes positioned at 2.2m from the sample and arranged on a cylindrical locus covering 10-170 degrees in 2 theta scattering angle. To reduce the background from sample environment, it is equipped with an oscillating radial collimator that defines a cylinder of radius about 22mm diameter at 90 degrees scattering.

The sample of desolvated NOTT-300 was loaded into a cylindrical vanadium sample container with an indium vacuum seal and connected to a gas handling system. The sample was degassed at 10^{-7} mbar and 120 °C for 1 day to remove any remaining trace guest water molecules. The temperature during data collection was controlled using a helium cryostat (10 ± 0.2 K). The loadings of C_2D_2, C_2D_4, and C_2D_6 were performed by volumetric method at room temperature in order to ensure that C_2D_2, C_2D_4, and C_2D_6 were present in the gas phase when not adsorbed and also to ensure sufficient mobility of C_2D_2, C_2D_4, and C_2D_6 inside the crystalline structure of NOTT-300. The equimolar mixture of C_2D_2 and C_2D_4 was prepared externally prior to dosing, which was performed in the same way as described in Section 1.3. Subsequently, the temperature was reduced to 10 K for data collection. In each case, the sample cell was isolated and sealed before cooling to prevent the condensation of free gas molecules in the cell during the cooling process.

The structure solution was initially established by considering the structure of bare NOTT-300 framework, and the residual nuclear density maps were further developed from subsequent difference Fourier analysis using TOPAS. The final structure refinements of NOTT-300·2.7C_2D_2, NOTT-300·1.8C_2D_4 and NOTT-300·1.3C_2D_6 were carried out using the Rietveld method[7] with isotropic displacement parameters for all atoms. Upon loading of hydrocarbon, there are significant changes in the Bragg peak intensities indicating that the hydrocarbon molecules are adsorbed into the NOTT-300 material. The final stage of the Rietveld refinement involved soft restraints to the C-C bond lengths within the benzene rings and carboxylate groups. Rigid body refinement was applied to define the molecular geometry for C_2D_2, C_2D_4, and C_2D_6 molecules in the pore, and no restraints were used in the position or orientation of the guest molecules within the pore. All of these molecules were located at general positions, and as a result positional disorder of the molecules was observed. A global isotropic thermal parameter was refined for the gas molecules, and the occupancies of the gas molecules were also refined. In the late stage of refinement of NOTT-300·1.8C_2D_4, orientation of C_2D_4 molecules was attempted in the form of both NOTT-300·C_2H_4G and NOTT-300·C_2H_4E, and the former refinement gives a much improved R factor and was used in the final refinement. This result is also consistent with that found in the case of NOTT-300·2.7C_2D_2 and NOTT-300·1.3C_2D_6. However, it does not exclude the existence of the NOTT-300·C_2H_4E form since the "static" diffraction experiment only measures the average

positions throughout the bulk sample. NOTT-300·C_2H_4G is thermodynamically more stable and will be more likely to dominate the orientation.

## 2. *In Situ* Synchrotron X-Ray Powder Diffraction Patterns
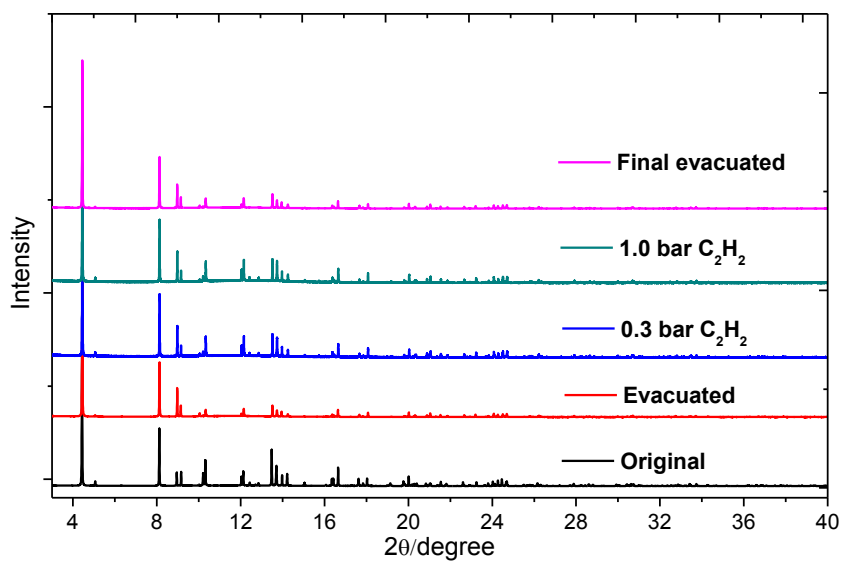
a
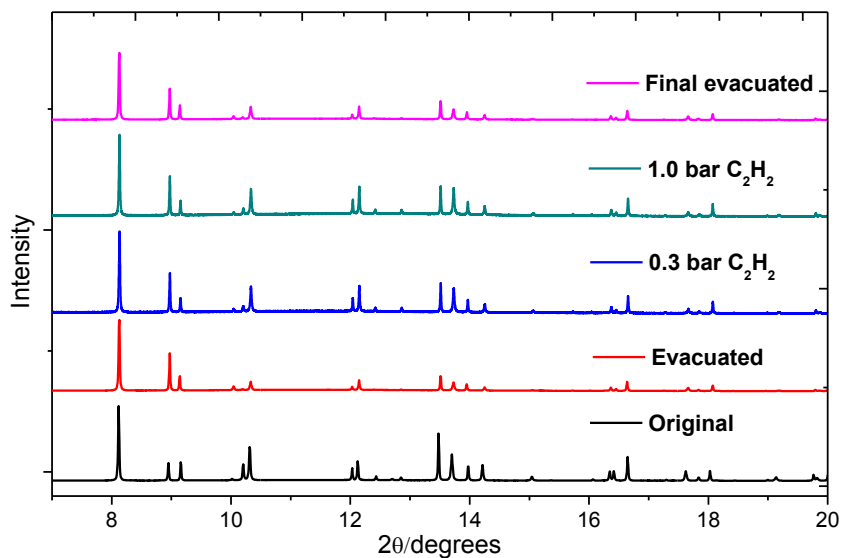
b

Figure 1. (a) Powder X-ray diffraction patterns for original, evacuated, C_2H_2-loaded, and final desolvated samples at 273 K [$\lambda = 0.826126(2)$ Å]; (b) higher angle data ($2\theta = 7\text{-}20^\circ$) has been scaled up confirming that NOTT-300 retains crystallinity on removal of C_2H_2.
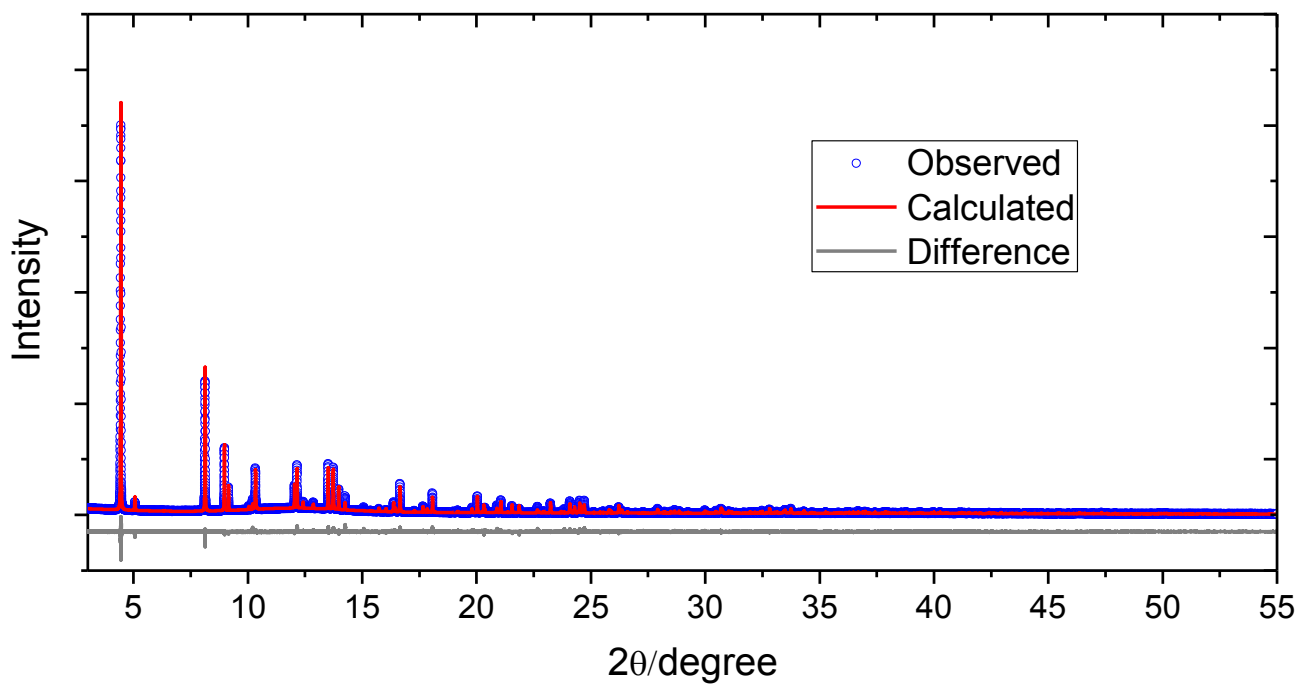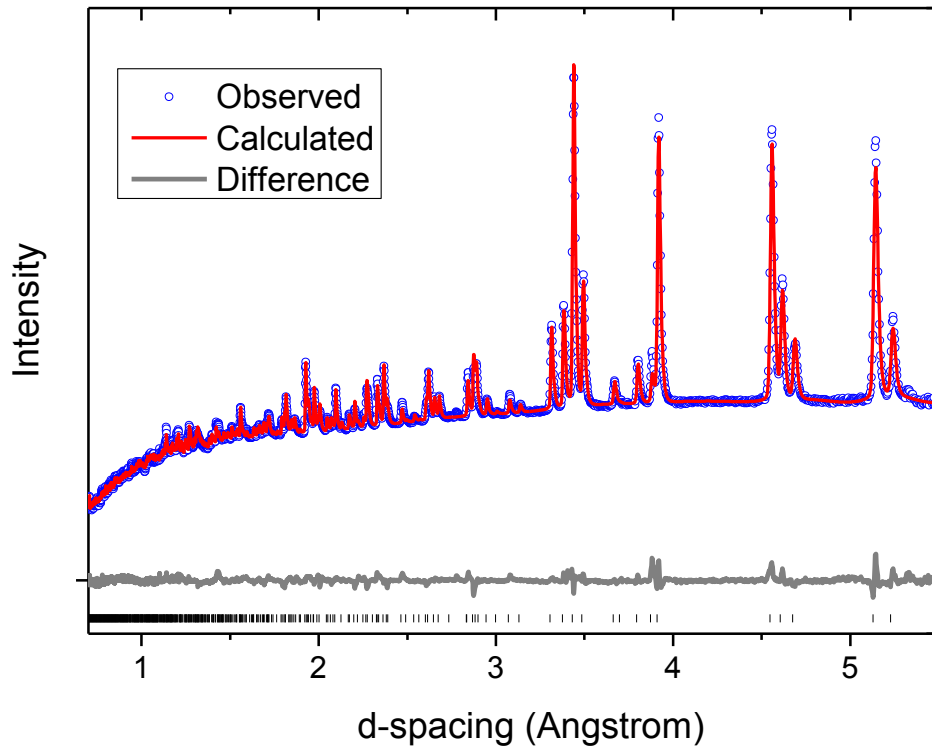
a
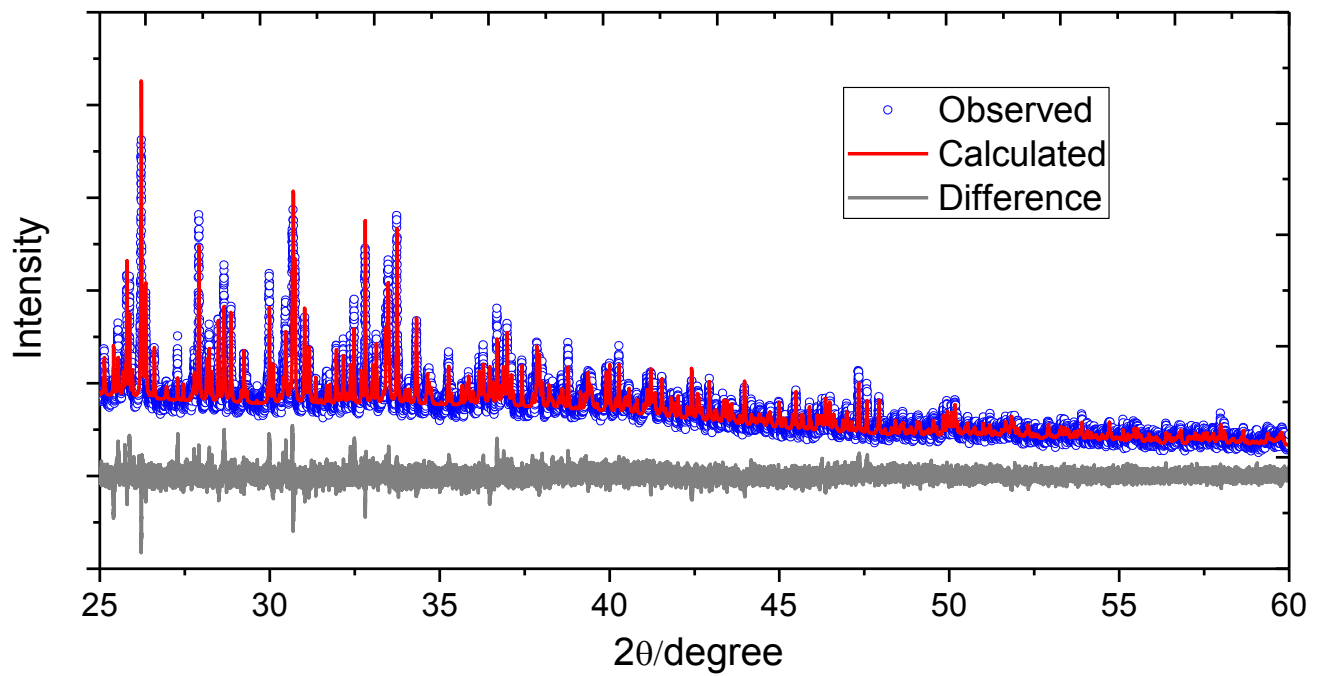
b

Figure 2. (a) PXRD patterns [observed (blue), calculated (red) and difference (grey)] for the Rietveld refinement of the C_2H_2-loaded NOTT-300·$4C_2H_2$ [$\lambda = 0.826126(2)$ Å]; (b) higher angle data ($2\theta = 25$-60°) scaled up to show the quality of fit between the observed and the calculated patterns.

Table 1. List of atomic positions for NOTT-300·$4C_2H_2$.

	Site-num	x	y	z	B_{iso} (Å^2)
Al1	8	0.69415(8)	0.30585(8)	0.5	0.63(12)
O1	8	0.75552(18)	0.25	0.625	0.30(12)
O2	16	0.89613(13)	0.28645(13)	0.99610(19)	0.30(12)
O3	16	0.62081(14)	0.37512(14)	0.39396(15)	0.30(12)
C1	16	0.58992(23)	0.35603(21)	0.69874(25)	0.30(12)
C2	16	0.53881(19)	0.42876(13)	0.76206(15)	0.30(12)
C3	8	0.5	0.5	0.70562(15)	0.30(12)
C4	16	0.53767(12)	0.42905(1)	0.88125(15)	0.30(12)
C5	8	0.5	0.5	0.93719(17)	0.30(12)
H1	8	0.81486	0.25	0.625	0.36(14)
H3	8	0.5	0.5	0.6290	0.36(14)
H4	16	0.57318	0.38162	0.90735	0.36(14)
C6a	16	0.04267	0.25	0.67013	5.65(27)
H6a	16	0.04267	0.25	0.75689	5.65(27)
C6b	16	0.04281	0.25	0.56998	5.65(27)
H6b	16	0.04281	0.25000	0.48323	5.65(27)
C7a	16	0.12722	0.34688	0.26520	6.88(36)
H7a	16	0.10815	0.41009	0.23993	6.88(36)
C7b	16	0.14929	0.27397	0.29453	6.88(36)
H7b	16	0.16836	0.21076	0.31980	6.88(36)

Table 2. List of bond lengths for NOTT-300·$4C_2H_2$.

Bond	Distance (Å)	Bond	Distance (Å)
Al1-O1	1.9198(17)	C2-C3	1.3744(22)
Al1-O2	1.9143(20)	C2-C4	1.4056(25)
Al1-O3	1.9493(23)	C4-C5	1.3612(18)
C1-O2	1.2368(36)	C5-C5	1.4813(39)
C1-O3	1.2575(35)	C6a-C6b	1.1810
C1-C2	1.5145(38)	C7a-C7b	1.1810
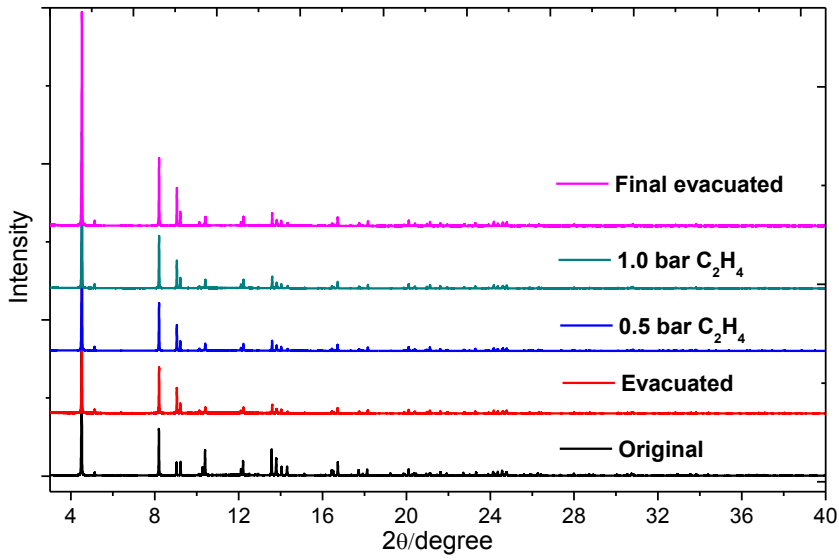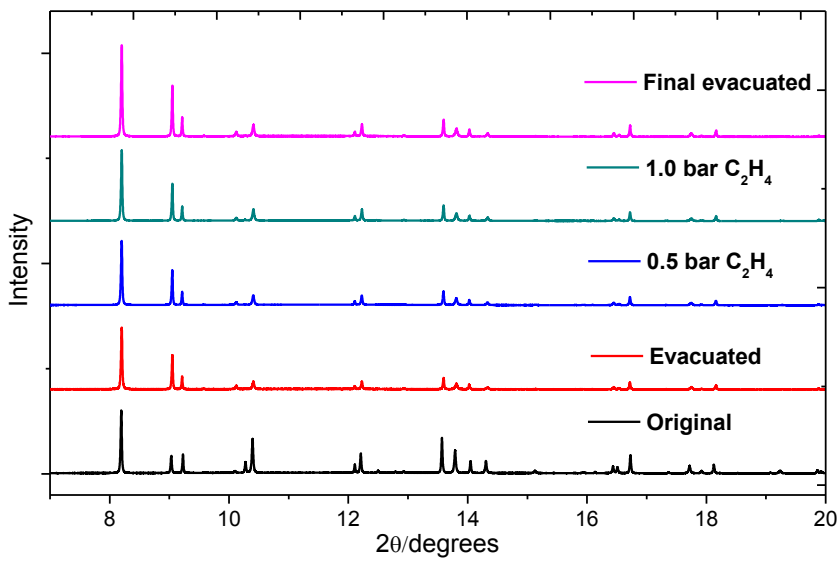
Figure 3. (a) Powder X-ray diffraction patterns for original, evacuated, C_2H_4-loaded, and final desolvated NOTT-300 at 273 K [$\lambda = 0.827136(2)$ Å]; (b) higher angle data ($2\theta = 7\text{-}20^{\circ}$) has been scaled up confirming that NOTT-300 retains crystallinity on removal of C_2H_4.
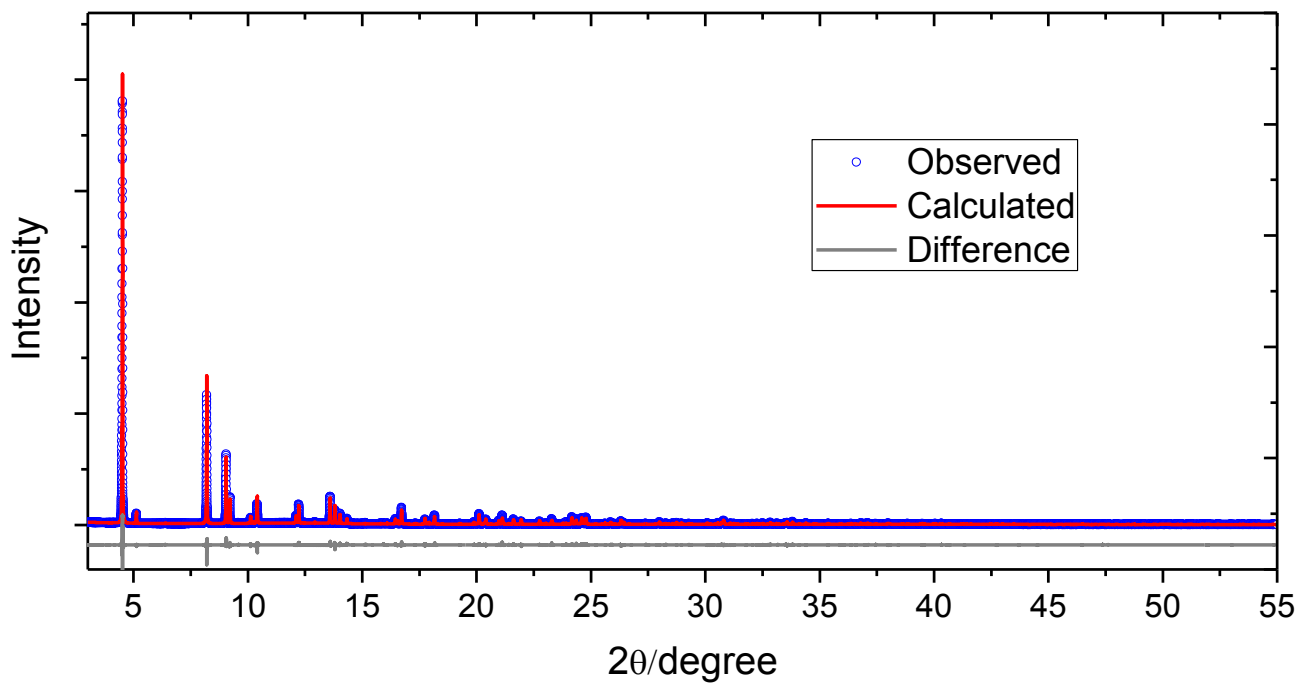
a
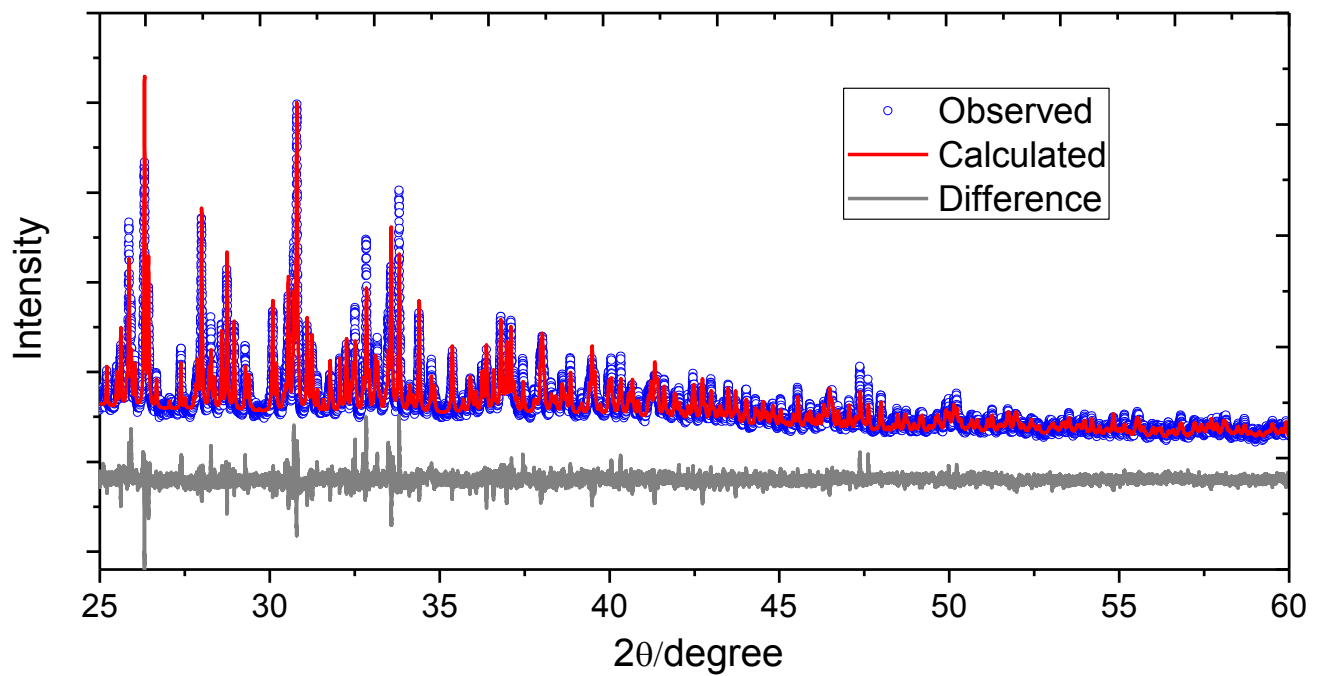
b

Figure 4. (a) PXRD patterns [observed (blue), calculated (red) and difference (grey)] for the Rietveld refinement of the C_2H_4-loaded NOTT-300·2.4C_2H_4 [λ = 0.827136(2) Å]; (b) higher angle data (2θ = 25-60°) scaled up to show the quality of fit between the observed and the calculated patterns.

Table 3. List of atomic positions for NOTT-300·2.5C$_2$H$_4$.

	Site-num	x	y	z	B_{iso} (Å^2)
Al1	8	0.69415(5)	0.30585(5)	0.5	0.94(24)
O1	8	0.75401(12)	0.25	0.625	0.50(20)
O2	16	0.62233(28)	0.37947(30)	0.60369(21)	0.50(20)
O3	16	0.60473(30)	0.28484(20)	0.74714(25)	0.50(20)
C1	16	0.59305(22)	0.35991(18)	0.70027(18)	0.99(28)
C2	16	0.54174(8)	0.42942(6)	0.76252(15)	0.99(28)
C3	8	0.5	0.5	0.70313(18)	0.99(28)
C4	16	0.54174(8)	0.42942(6)	0.88130(11)	0.99(28)
C5	8	0.5	0.5	0.94069(10)	0.99(28)
H1	8	0.81480	0.25	0.625	0.60(24)
H3	8	0.5	0.5	0.61416	1.19(33)
H4	16	0.57301	0.37655	0.92578	1.19(33)
C6a	16	0.55036	0.75	0.13829	16.58(57)
H6a	16	0.51077	0.70046	0.09187	16.58(57)
H6b	16	0.59292	0.79754	0.09271	16.58(57)
C6b	16	0.54676	0.75245	0.24661	16.58(57)
H6c	16	0.58618	0.80213	0.29302	16.58(57)
H6d	16	0.50412	0.70498	0.29218	16.58(57)
C7a	16	0.150	0.3220	0.196	20.0(9)
H7a	16	0.1225	0.3739	0.2509	24.0(11)
H7b	16	0.177	0.3400	0.113	24.0(11)
C7b	16	0.152	0.2397	0.229	20.00(9)
H7c	16	0.180	0.1878	0.174	24.0(11)
H7d	16	0.126	0.2217	0.312	24.0(11)

Table S4. List of bond lengths for NOTT-300·2.5C$_2$H$_4$.

Bond	Distance (Å)	Bond	Distance (Å)
Al1-O1	1.9092(11)	C2-C3	1.4018(9)
Al1-O2	1.9535(35)	C2-C4	1.4018(9)
Al1-O3	1.8859(30)	C4-C5	1.4018(9)
C1-O2	1.2534(12)	C5-C5	1.4000(24)
C1-O3	1.2534(12)	C6a-C6b	1.2800
C1-C2	1.4750(23)	C7a-C7b	1.2800

3. *In Situ* Neutron Powder Diffraction Patterns

Figure 5. NPD patterns [observed (blue), calculated (red) and difference (grey)] for the Rietveld refinement of the NOTT-300·2.7C_2D_2.

Table 5. List of atomic positions for NOTT-300·2.7C$_2$D$_2$.

	Site-num	x	y	z	B_{iso} (Å^2)
Al1	8	0.6924 (4)	0.3076(4)	0.5	0.50(25)
O1	8	0.7525(4)	0.25	0.625	1.04(7)
O2	16	0.6250(4)	0.3802(4)	0.6000(5)	1.04(7)
O3	16	0.6077(4)	0.2865(4)	0.7408(5)	1.04(7)
C1	16	0.5943(3)	0.3628(3)	0.6970(3)	1.26(6)
C2	16	0.5431(1)	0.4308(1)	0.7585(2)	1.26(6)
C3	8	0.5	0.5	0.6993(2)	1.26(6)
C4	16	0.5431(1)	0.4308(1)	0.8767(2)	1.26(6)
C5	8	0.5	0.5	0.9359(2)	1.26(6)
H1	8	0.8149	0.25	0.625	1.04(7)
H3	8	0.5	0.5	0.6101	1.26(6)
H4	16	0.5756	0.3786	0.9213	1.26(6)
C6	16	0.0730	0.25	0.6749	7.54(37)
D6	16	0.0730	0.25	0.7611	7.54(37)
C6a	16	-0.0102	0.2485	0.6266	7.54(37)
D6a	16	-0.0753	0.2345	0.6477	7.54(37)
C6b	16	0.0652	0.2647	0.6023	7.54(37)
D6b	16	0.1303	0.2787	0.5813	7.54(37)
C7a	16	0.1535	0.4114	0.2490	6.15(36)
D7a	16	0.1838	0.4728	0.2432	6.15(36)
C7b	16	0.1184	0.3402	0.2558	6.15(36)
D7b	16	0.0881	0.2788	0.2616	6.15(36)

Table 6. List of bond lengths for NOTT-300·2.7C$_2$D$_2$.

Bond	Distance (Å)	Bond	Distance (Å)
Al1-O1	1.9182(55)	C2-C3	1.3926(13)
Al1-O2	1.8792(83)	C2-C4	1.3926(13)
Al1-O3	1.8743(49)	C4-C5	1.3926(13)
C1-O2	1.2562(28)	C5-C5	1.5103(39)
C1-O3	1.2562(28)	C6a-C6b	1.176
C1-C2	1.4512(33)	C7a-C7b	1.176
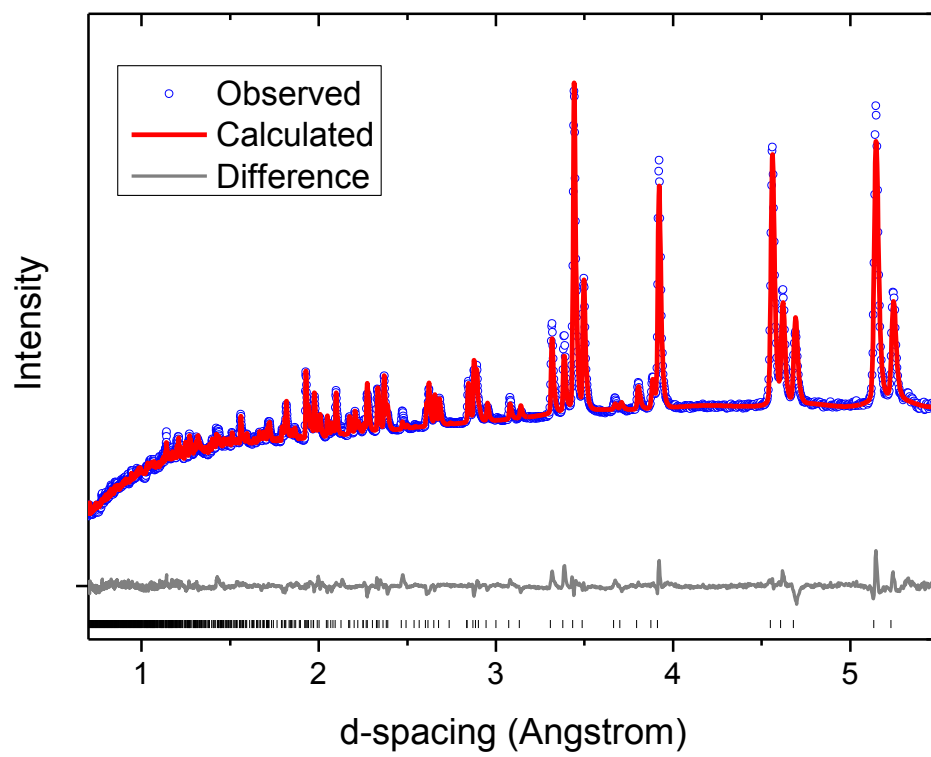
Figure 6. NPD patterns [observed (blue), calculated (red) and difference (grey)] for the Rietveld refinement of the NOTT-300·1.8C$_2$D$_4$.

Table 7. List of atomic positions for NOTT-300·1.8C$_2$D$_4$.

	Site-num	x	y	z	B_{iso} (Å^2)
Al1	8	0.6944(4)	0.3056(4)	0.5	0.50(28)
O1	8	0.7559(4)	0.25	0.625	2.57(11)
O2	16	0.6253(6)	0.3810(7)	0.6000(5)	2.57(11)
O3	16	0.6084(6)	0.2874(4)	0.7386(6)	2.57(11)
C1	16	0.5943(4)	0.3629(4)	0.6955(3)	1.18(7)
C2	16	0.5417(2)	0.4298(1)	0.7567(3)	1.18(7)
C3	8	0.5	0.5	0.6974(4)	1.18(7)
C4	16	0.5417(2)	0.4298(1)	0.8752(2)	1.18(7)
C5	8	0.5	0.5	0.9345(2)	1.18(7)
H1	8	0.8168	0.25	0.625	2.57(11)
H3	8	0.5	0.5	0.6083	1.18(7)
H4	16	0.5731	0.3769	0.9198	1.18(7)
C6a	16	0.0112	0.2326	0.6447	5.87(35)
D6a	16	0.0107	0.2065	0.7310	5.87(35)
D6b	16	-0.0509	0.2578	0.6068	5.87(35)
C6b	16	0.0883	0.2338	0.5852	5.87(35)
D6c	16	0.0889	0.2601	0.4990	5.87(35)
D6d	16	0.1504	0.2087	0.6232	5.87(35)
C7a	16	0.0454	0.3510	0.2647	4.51(51)
D7a	16	0.0251	0.42078	0.2785	4.51(51)
D7b	16	-0.0045	0.2972	0.2690	4.51(51)
C7b	16	0.1319	0.3314	0.2422	4.51(51)
D7c	16	0.1522	0.2617	0.2280	4.51(51)
D7d	16	0.1818	0.3853	0.2377	4.51(51)

Table 8. List of bond lengths for NOTT-300·1.8C$_2$D$_4$.

Bond	Distance (Å)	Bond	Distance (Å)
Al1-O1	1.9170(63)	C2-C3	1.3959(16)
Al1-O2	1.918(10)	C2-C4	1.3959(16)
Al1-O3	1.8789(58)	C4-C5	1.3959(16)
C1-O2	1.2437(33)	C5-C5	1.3959(16)
C1-O3	1.2437(33)	C6a-C6b	1.3390
C1-C2	1.4500(39)	C7a-C7b	1.3390
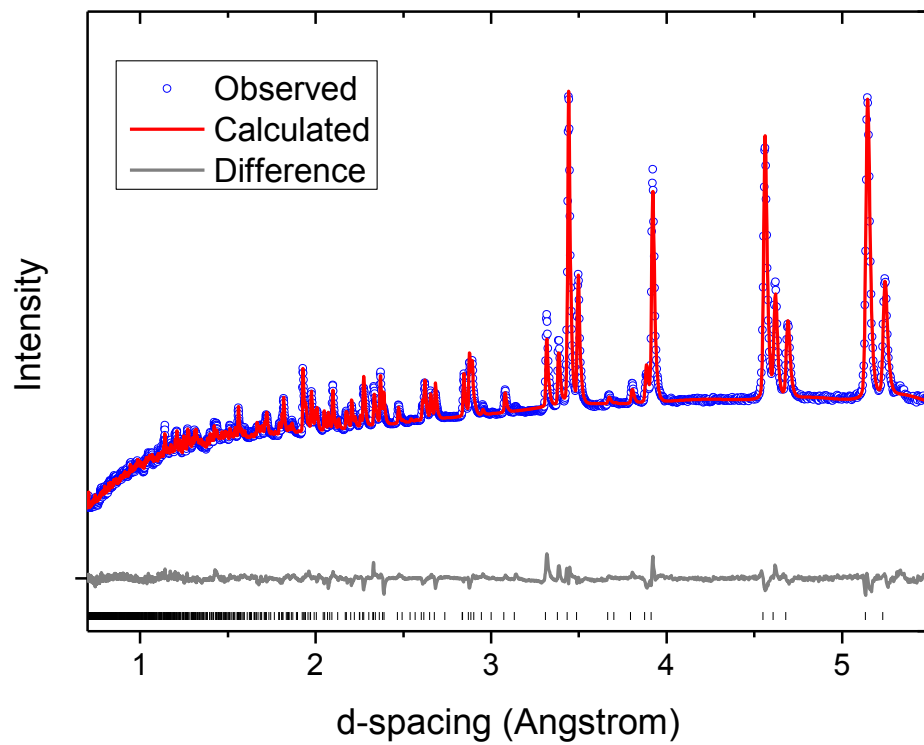
Figure 7. NPD patterns [observed (blue), calculated (red) and difference (grey)] for the Rietveld refinement of the NOTT-300·1.3C_2D_6.

Table 9. List of atomic positions for NOTT-300·1.3C_2D_6.

	Site-num	x	y	z	B_{iso} (Å^2)
Al1	8	0.6924(5)	0.3076(5)	0.5	0.50(29)
O1	8	0.7520(4)	0.25	0.625	2.22(11)
O2	16	0.6213(6)	0.3803(6)	0.6009(5)	2.22(11)
O3	16	0.6039(6)	0.2876(4)	0.7426(6)	2.22(11)
C1	16	0.5927(4)	0.3614(4)	0.6963(4)	0.93(7)
C2	16	0.5428(2)	0.4304(1)	0.7579(3)	0.93(7)
C3	8	0.5	0.5	0.6987(4)	0.93(7)
C4	16	0.5428(2)	0.4304(1)	0.8763(2)	0.93(7)
C5	8	0.5	0.5	0.9356(2)	0.93(7)
H1	8	0.8128	0.25	0.625	2.22(11)
H3	8	0.5	0.5	0.6121	0.93(7)
H4	16	0.5740	0.3796	0.9196	0.93(7)
C6a	16	0.0091	0.2232	0.6264	3.00(30)
D6a	16	0.0032	0.1504	0.6118	3.00(30)
D6b	16	-0.0508	0.2568	0.5922	3.00(30)
D6c	16	0.0134	0.2368	0.7175	3.00(30)
C6b	16	0.0942	0.2583	0.5665	3.00(30)
D6d	16	0.0997	0.3311	0.5804	3.00(30)
D6e	16	0.0889	0.2441	0.4757	3.00(30)
D6f	16	0.1534	0.2240	0.6017	3.00(30)
C7a	16	0.1366	0.2972	0.2623	2.04(50)
D7a	16	0.0913	0.2954	0.3355	2.04(50)
D7b	16	0.2038	0.2750	0.2888	2.04(50)
D7c	16	0.1117	0.2519	0.1960	2.04(50)
C7b	16	0.1412	0.3944	0.2170	2.04(50)
D7d	16	0.1871	0.3964	0.1443	2.04(50)
D7e	16	0.1662	0.4388	0.2842	2.04(50)
D7f	16	0.0736	0.4156	0.1909	2.04(50)

Table 10. List of bond lengths for NOTT-300·1.3C_2D_6.

Bond	Distance (Å)	Bond	Distance (Å)
Al1-O1	1.9181(71)	C2-C3	1.3960(16)
Al1-O2	1.917(11)	C2-C4	1.3960(16)
Al1-O3	1.9241(62)	C4-C5	1.3960(16)
C1-O2	1.2304(33)	C5-C5	1.5191(51)
C1-O3	1.2304(33)	C6a-C6b	1.5351
C1-C2	1.4558(42)	C7a-C7b	1.5351

In order to gain crystallographic insight into the adsorption of an acetylene/ethylene mixture in NOTT-300, we also studied equimolar mixtures of C_2D_2/C_2D_4 loaded NOTT-300 by neutron diffraction. Upon loading of the mixture, significant intensity changes were observed in the diffraction pattern confirming adsorption of gas molecules into the crystalline structure of NOTT-300 (Supplementary Figure 8). The residual nuclear density maps were developed from difference Fourier analysis by considering the structure of bare NOTT-300 framework (Supplementary Figure 9). Two independent binding sites can be seen clearly from the map. Site I is close to –OH group and Site II is in the centre of the pore. Based upon this residual map, two refinement models were constructed: (i) C_2D_2 sits at Site I and C_2D_4 sits at Site II; (ii) C_2D_4 sits at Site I and C_2D_2 sits at Site II. These two refinements give similar R factors, suggesting satisfactory refinement can be obtained in either case (Supplementary Table 11). In Model i, the site occupancies at I and II are refined as 0.854(16) and 0.392(4), respectively. In contrast, these site occupancies are refined as 0.502(4) and 0.578(6) for I and II, respectively, in model ii. The ratios of occupancies at Site I over Site II are approximately 2 and 1 for Models i and ii, respectively. Model i is thus more consistent with the IAST selectivity and the corresponding mixture loaded INS experiment, and is more likely to represent the actual situation. However, due to the similar contribution of C_2D_2 and C_2D_4 molecule to the diffraction experiment (difference in scattering cross section can be off-set by varying occupancy) and possible presence of mixed site occupancy, it is not reliable to definitively conclude the percentage of C_2D_2 or C_2D_4 on each site, and therefore, none of the structural details for these models (i and ii) are reported here. Nevertheless, model i has a better representation of the mixture-loaded NOTT-300 by considering the site occupancy and selectivity determined by IAST and mixed gas adsorption isotherms, and model i was therefore used for DFT optimisation (Figure 4). This experiment also confirmed that the Al-OH moiety group close to Site I can induce a relatively strong interaction to the guest molecule, and this is evidenced by the higher occupancy observed at site I in both models. Due to their different binding interaction to the host framework, C_2D_2 and C_2D_4 molecules behave differently in the corresponding INS experiment, and thus can be more readily distinguished as shown in Figure 4.
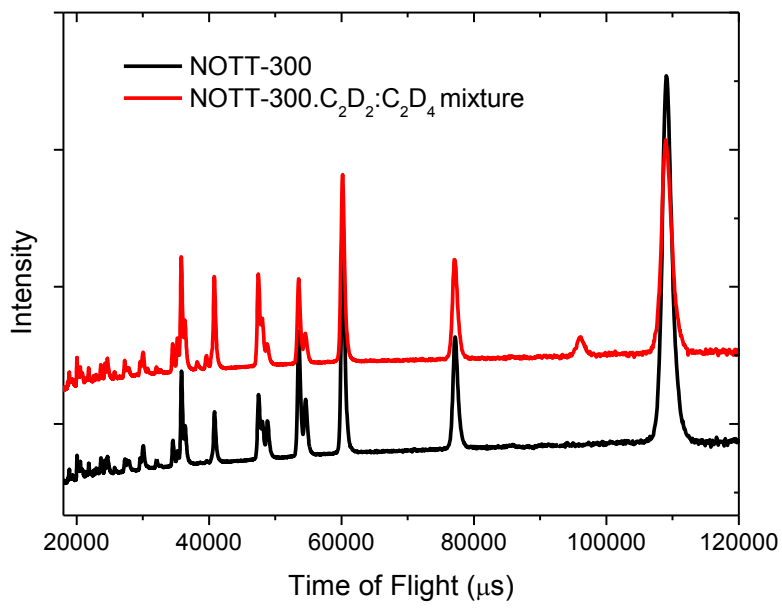
a
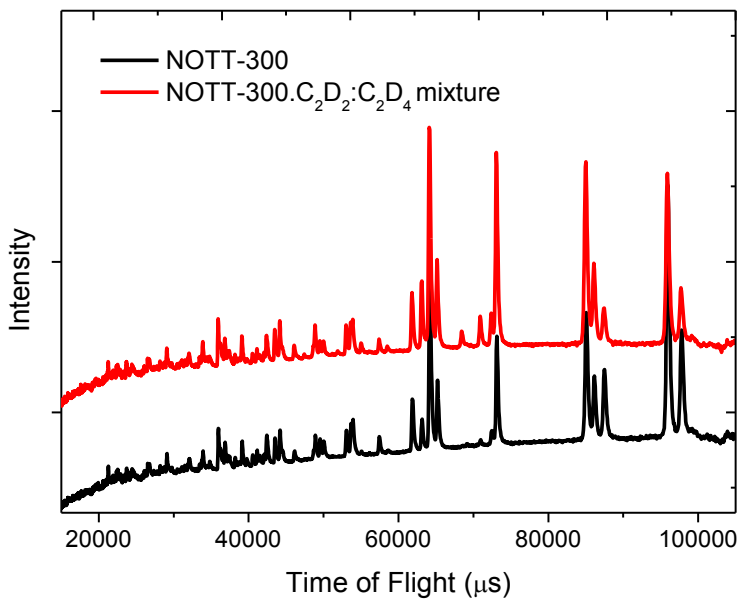
b

Figure 8. (a) Neutron powder diffraction patterns for bare and C_2D_2-C_2D_4 mixture loaded samples on NOTT-300 at 10 K; (b) low d-spacing data from a high resolution detector has been scaled up.

a   b
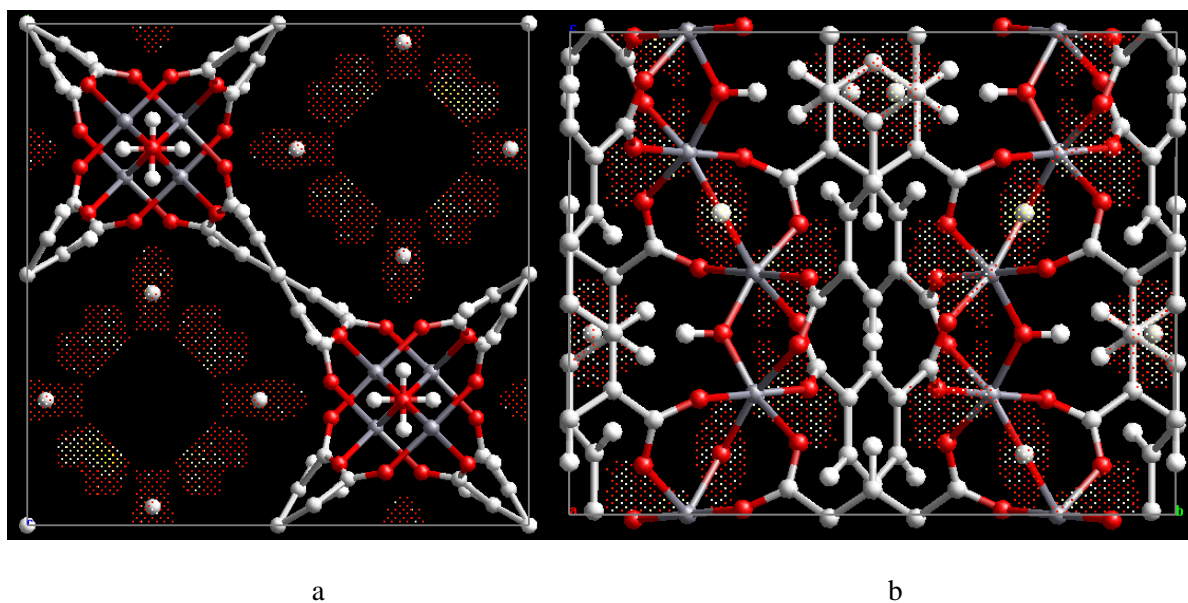
Figure 9. Views of the residual nuclear density in the channel of NOTT-300·C_2D_2-C_2D_4 mixture (a) along the c-axis and (b) along the a-axis. Models were obtained from Fourier difference map analysis (Fobs-Fcalc) of the data for NOTT-300 loaded with an equimolar mixture of C_2D_2 and C_2D_4 mixture. No C_2D_2 or C_2D_4 molecules were included in the difference map calculation. Two independent binding sites can be seen clearly from the map. Site I is close to the –OH group and Site II is in the middle of the pore. Site II is more dispersive than Site I, indicating the possible population of C_2D_4 molecules at Site II. The distance between the centroid of Site (I) to the H(δ+) of –OH is 3.38 Å.

Table 11. Comparison of the refinement results for NOTT-300·C_2D_2:C_2D_4 mixture by two different models (i, ii).

	Model i	Model ii
R_p	0.013	0.014
R_{wp}	0.015	0.016
gof	3.59	3.81
Occupancy at Site I	0.854(16) by C_2D_2	0.502(4) by C_2D_4
Occupancy at Site II	0.392(4) by C_2D_4	0.578(6) by C_2D_2

4. Additional View of Crystal Structures

a

b

c
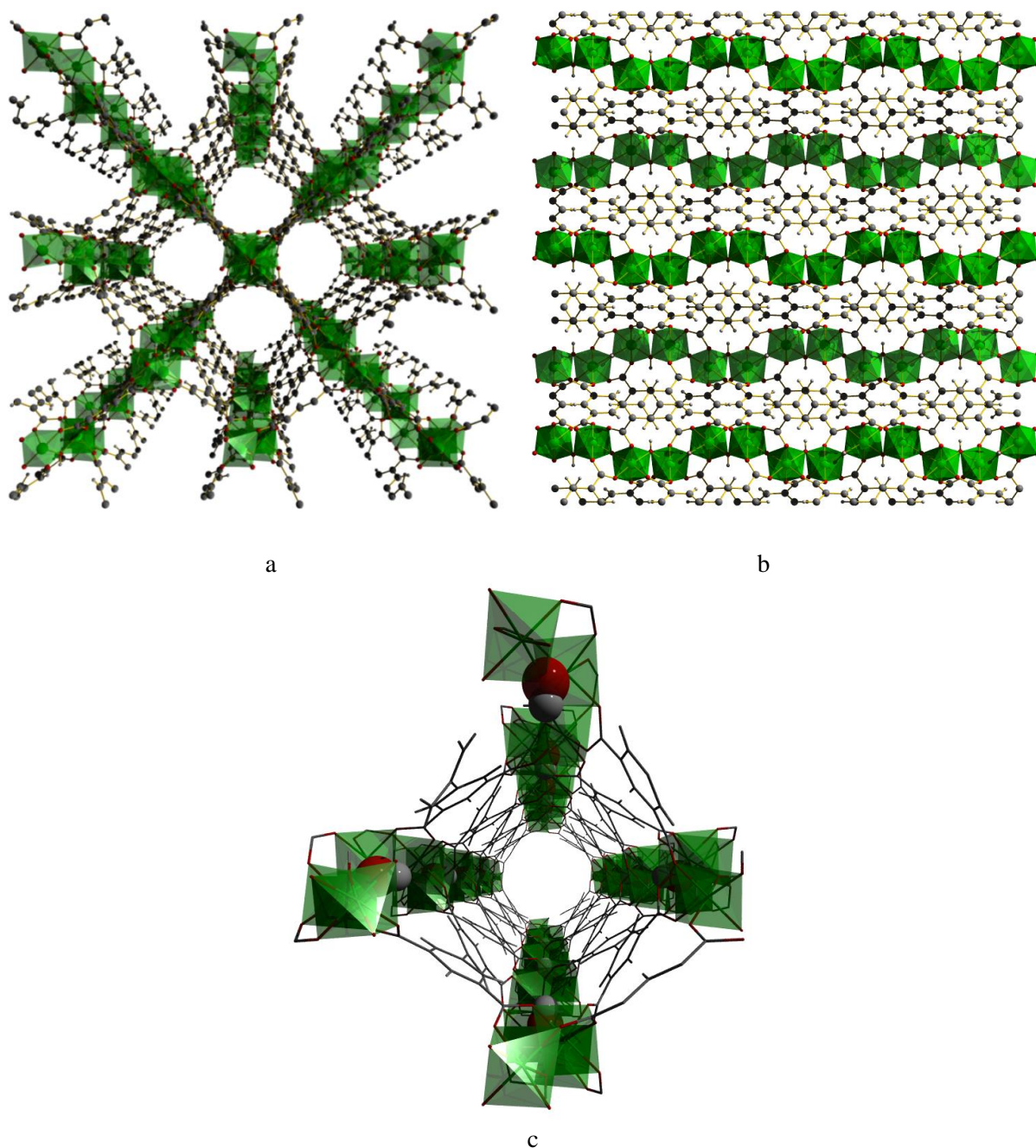
Figure 10. View of the structure for NOTT-300-solvate (a) along the c-axis and (b) along the a-axis. (c) View of the square-shaped channel. The μ_2-(OH) groups protrude into the centre of the channel from four directions. (Al: green; carbon: grey; oxygen: red; hydrogen: white; [AlO$_4$(OH)$_2$]: green octahedron). The structure was obtained by high resolution synchrotron powder diffraction. NOTT-300 displays a surface area of 1370 m^2 g^{-1}, a pore volume of 0.38 cm^3 g^{-1} and 6.5 Å-wide channels decorated with free metal-hydroxyl (M—OH) groups, each with an open environment to guest molecules. The density of free hydroxyl groups is estimated as 21.2 –OH per 1000 Å^2. The distance between two adjacent –OH groups is approximately 3.22 Å (H···H).

a   b
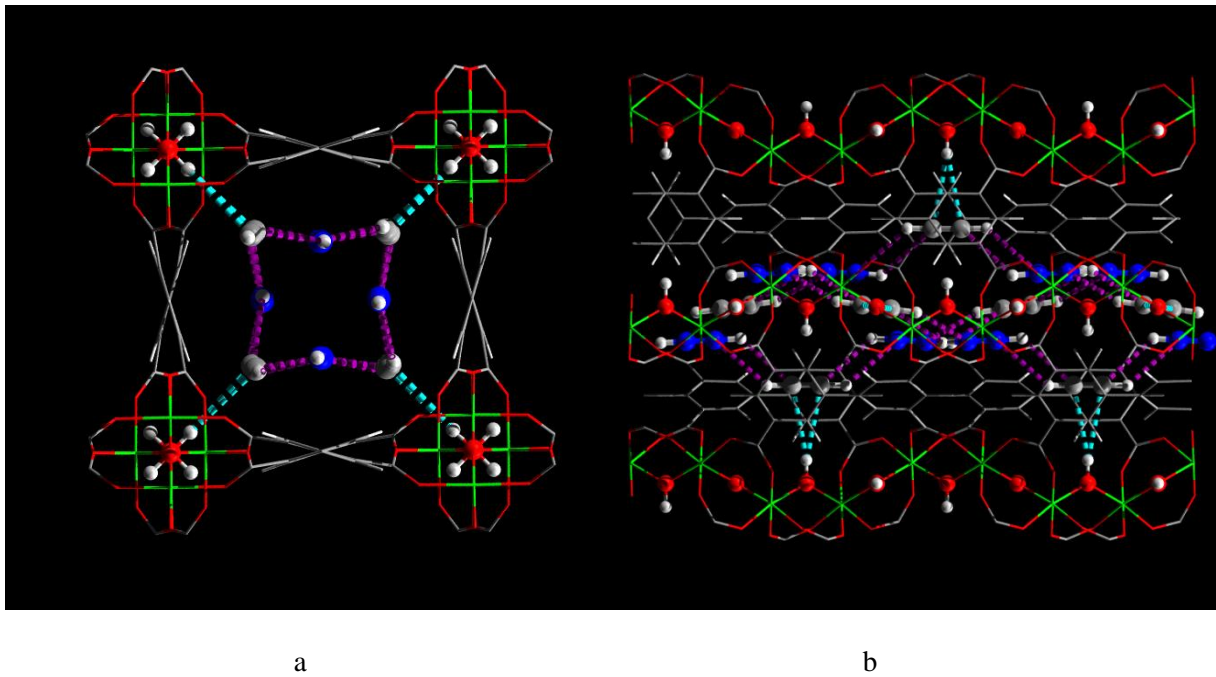
Figure 11. View of the structure of NOTT-300·$3C_2H_2$ (a) along the *c*-axis and (b) along the *a*-axis. The structure was obtained by DFT simulation. The adsorbed C_2H_2 molecules in the pore channel are highlighted by the use of ball-and-stick style. The carbon atoms for C_2H_2(II) molecules are highlighted in blue.
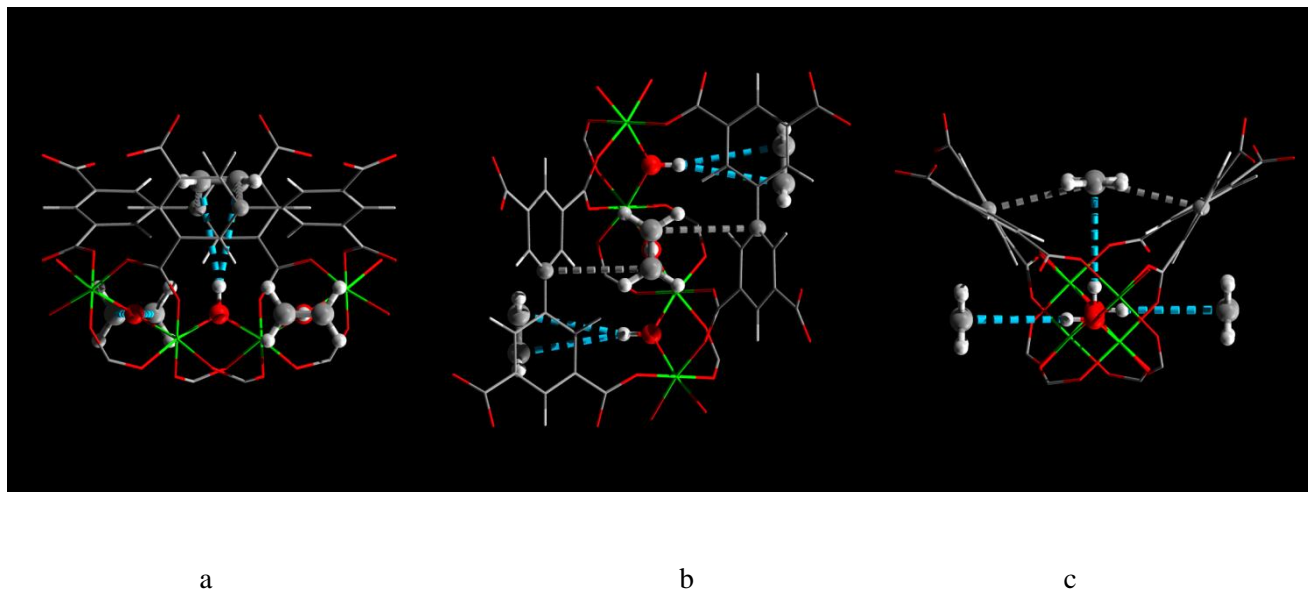
| a | b | c |
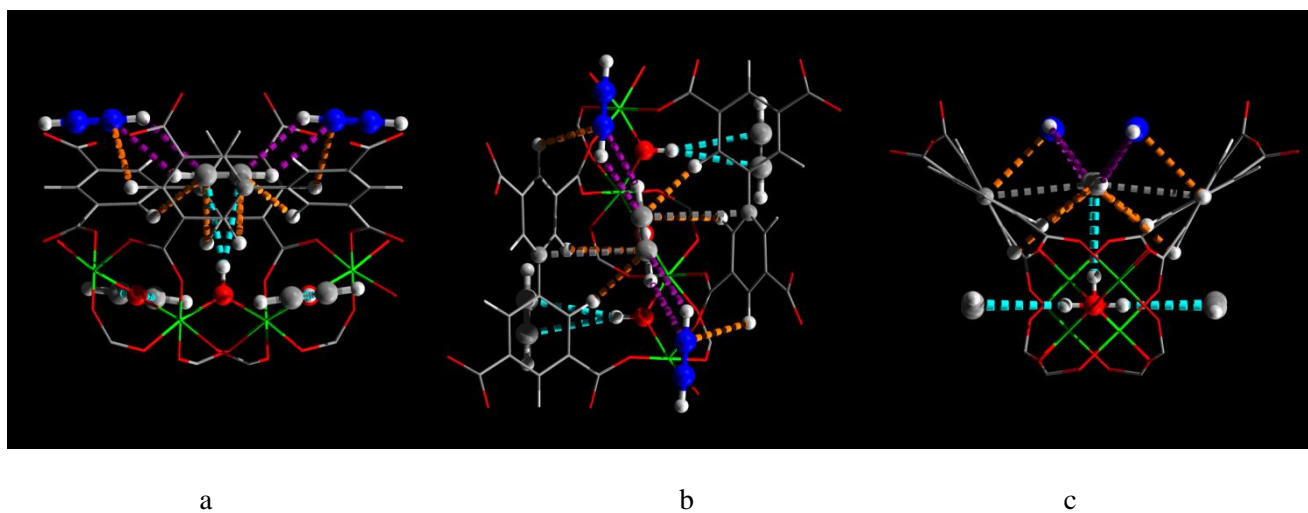
Figure 12. Detailed views of -OH, -CH, and phenyl ring groups binding C_2H_2 molecules in the functionalised cavity of NOTT-300·$3C_2H_2$. Views along (a) the *a*-axis, (b) the *b*-axis and (c) the *c*-axis. The structure was obtained by DFT simulation. The weak hydrogen-bond between C(δ-) of C_2H_2 and H(δ+) of -OH is highlighted in cyan, [O···H = 3.21 Å]. The weak cooperative supramolecular bond between C(δ-) of C_2H_2 and H(δ+) from -CH is highlighted in orange, [O···H = 2.96, 3.64 Å with each occurring twice]. The weak π···π stacking interaction between π-electrons of C_2H_2 and phenyl rings on the ligand is highlighted in grey [C≡C···C_6 = 3.81 Å, occurring twice]. The weak electrostatic dipole interactions between C_2H_2(I) and C_2H_2(II) molecules are highlighted in purple [C^I···H^{II} = 3.24 Å; C^{II}···H^I = 3.12 Å, each occurring twice]. Therefore, in total, four types of weak interactions cooperatively interact together to bind C_2H_2 molecules in the functionalised cavity.
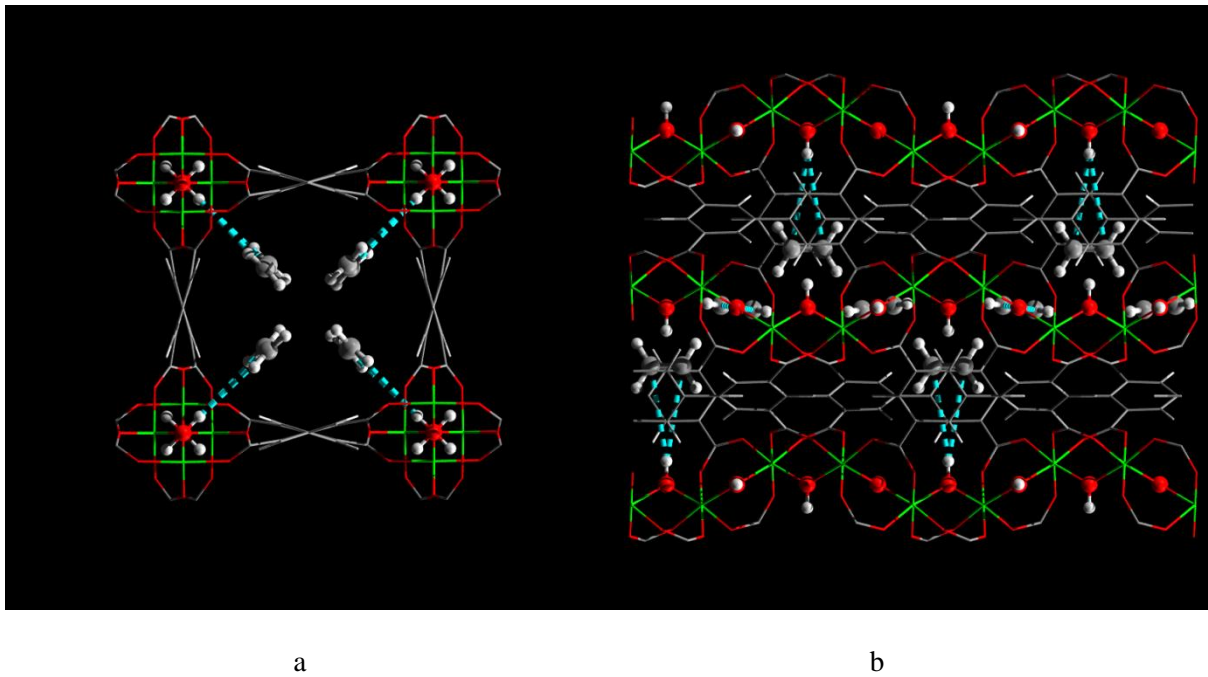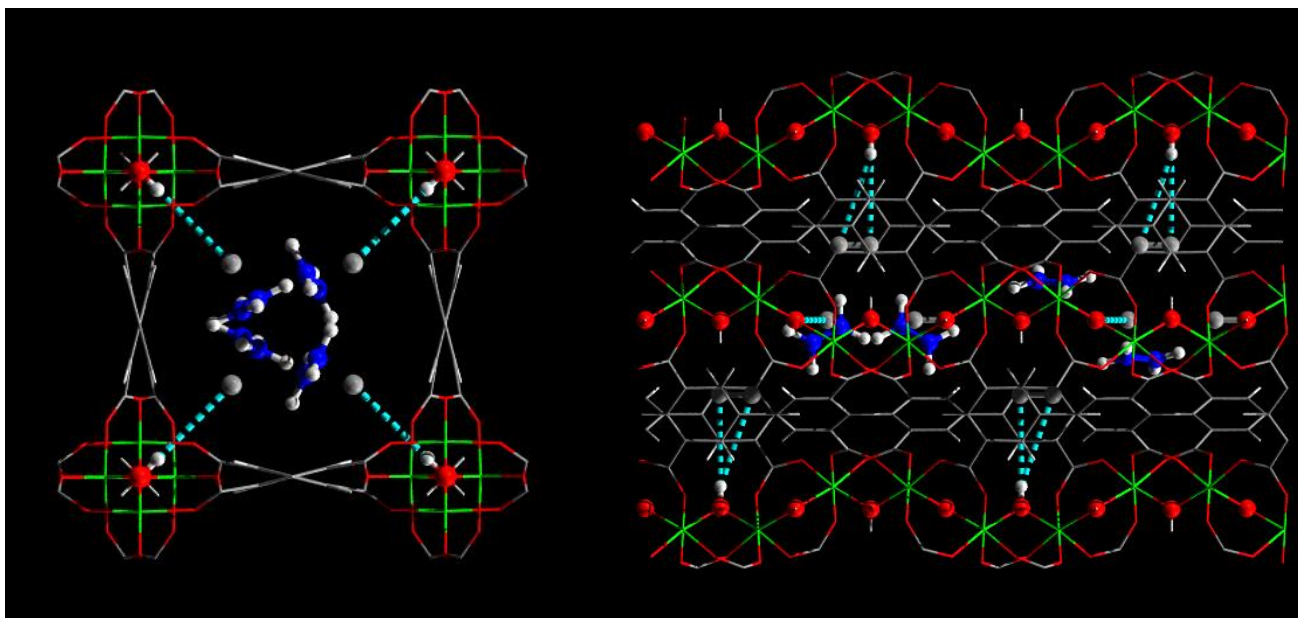
a   b
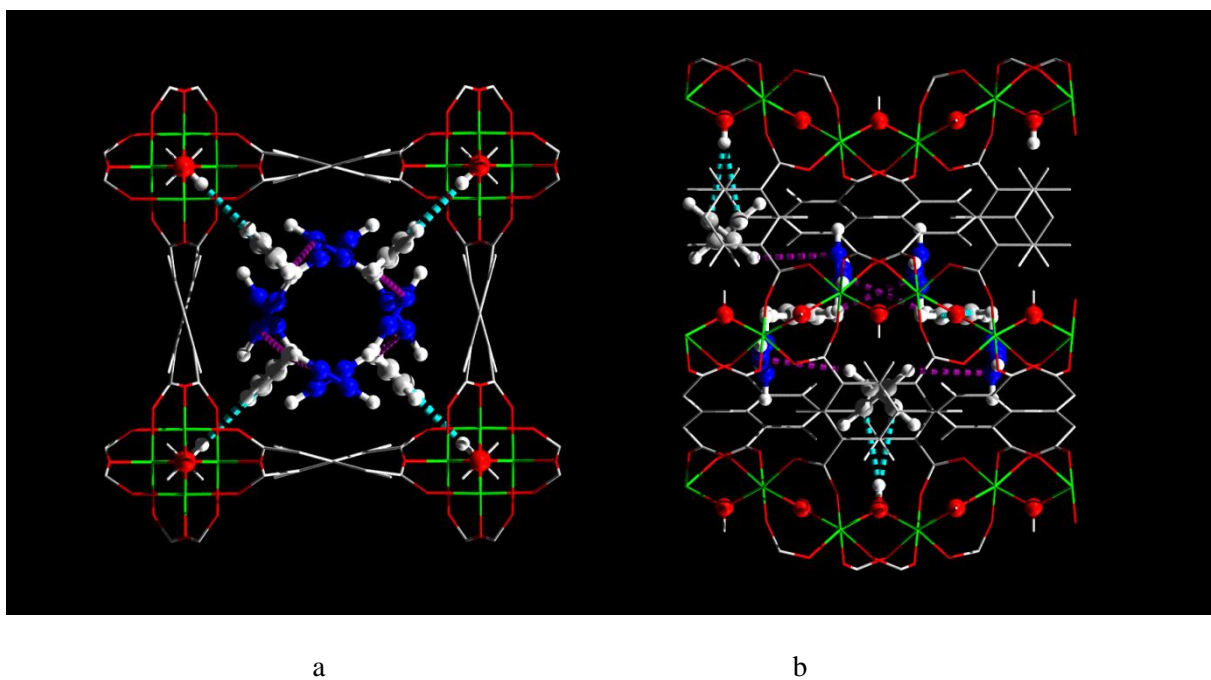
Figure 13. View of the structure of NOTT-300·2.7C_2D_2 (a) along the *c*-axis and (b) along the *a*-axis. The structure was obtained by high resolution neutron powder diffraction. Clear positional disorder for C_2D_2 molecules at both Site I and II can be found. The adsorbed C_2D_2 molecules in the pore channel are highlighted by the use of ball-and-stick style. The carbon atoms for C_2D_2(II) molecules are highlighted in blue.

a   b   c
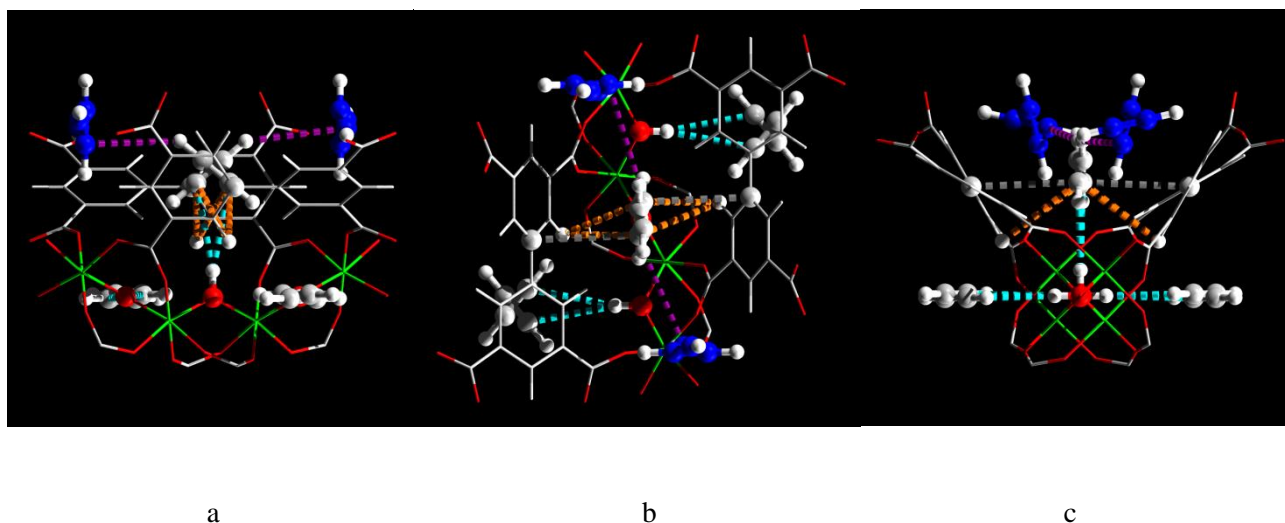
Figure 14. Detailed views of –OH, -CH, and phenyl ring groups binding C_2D_2 molecules in the functionalised "pocket" cavity of NOTT-300·2.7C_2D_2. Views along (a) the *a*-axis, (b), the *b*-axis and (c) the *c*-axis. The structure was obtained by high resolution neutron powder diffraction. Clear positional disorder for C_2D_2 molecules at both sites I and II can be found, inducing slight differences in bond distances in comparison to the model obtained from DFT/INS study which gives the average position without disorder. The weak hydrogen-bond between $C(\delta-)$ of C_2D_2 and $H(\delta+)$ of -OH is highlighted in cyan, $[C\cdots D = 3.41$ Å]. The weak cooperative supramolecular bond between $C(\delta-)$ of C_2D_2 and $H(\delta+)$ from -CH is highlighted in orange, $[C\cdots H = 2.92 - 3.61$ Å]. The weak $\pi\cdots\pi$ stacking interaction between π-electrons of C_2H_2 and phenyl rings on the ligand is highlighted in grey $[C\equiv C\cdots C_6 = 3.81$ Å]. The weak electrostatic dipole interactions between $C_2H_2(I)$ and $C_2H_2(II)$ molecules are highlighted in purple $[C^{II}\cdots H^I = 3.12$ Å]. Therefore, in total, four types of weak interactions cooperatively interact together to bind C_2H_2 molecules in the functionalised cavity.
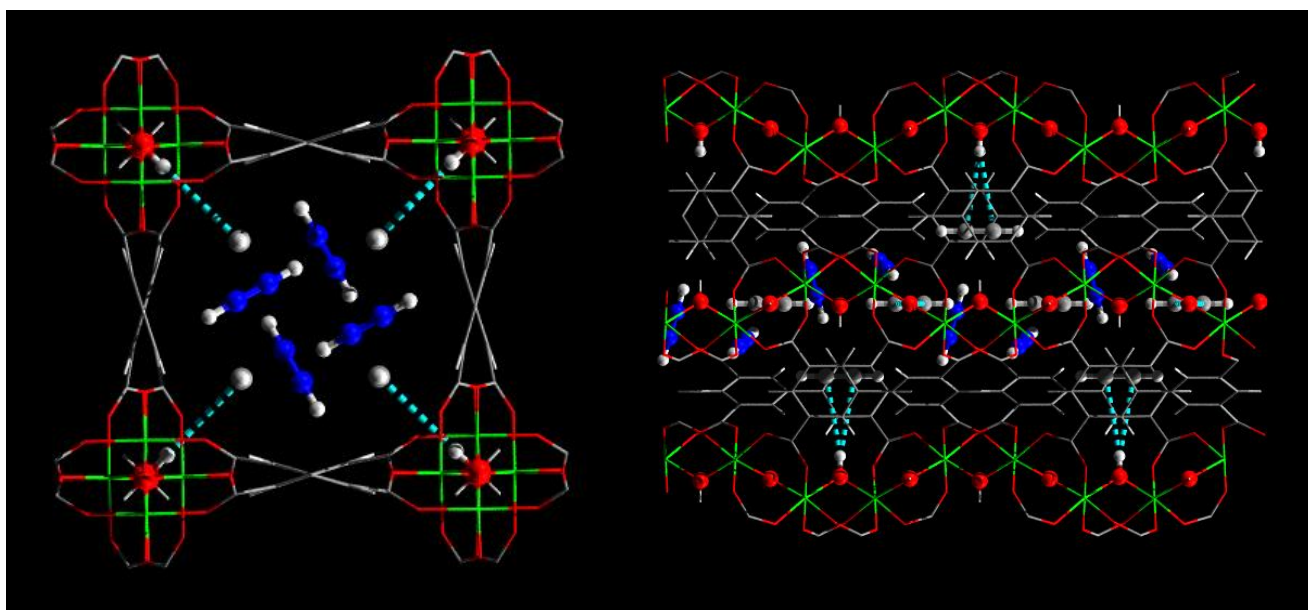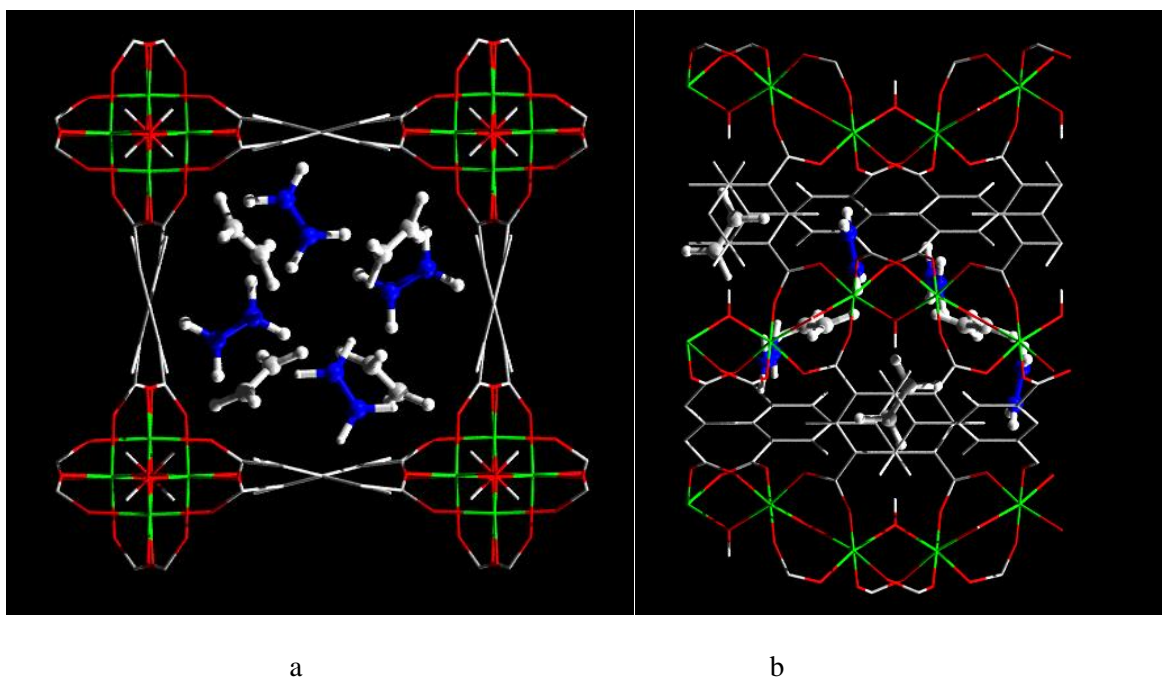
a   b

Figure 15. View of the structure of NOTT-300·4C_2H_2 (a) along the *c*-axis and (b) along the *a*-axis. The structure was obtained by synchrotron X-ray powder diffraction experiments. Clear positional disorder for C_2H_2 molecules at II was found. The adsorbed C_2H_2 molecules in the pore are highlighted by the use of ball-and-stick style. The carbon atoms for C_2H_2(II) molecules are highlighted in blue.
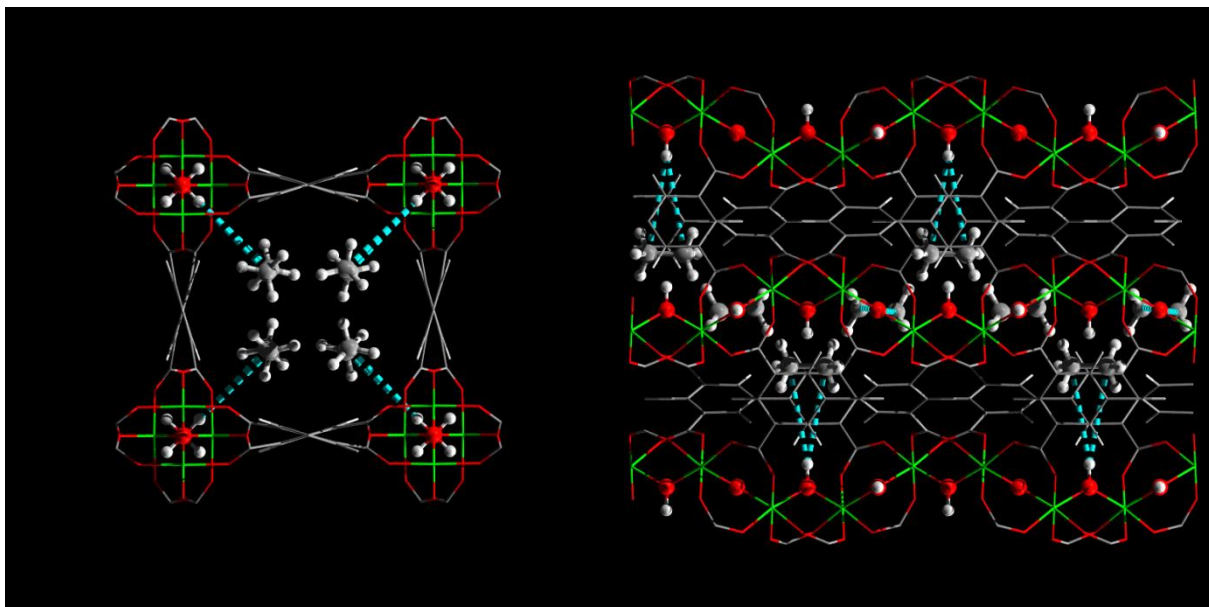
<center>a   b   c</center>
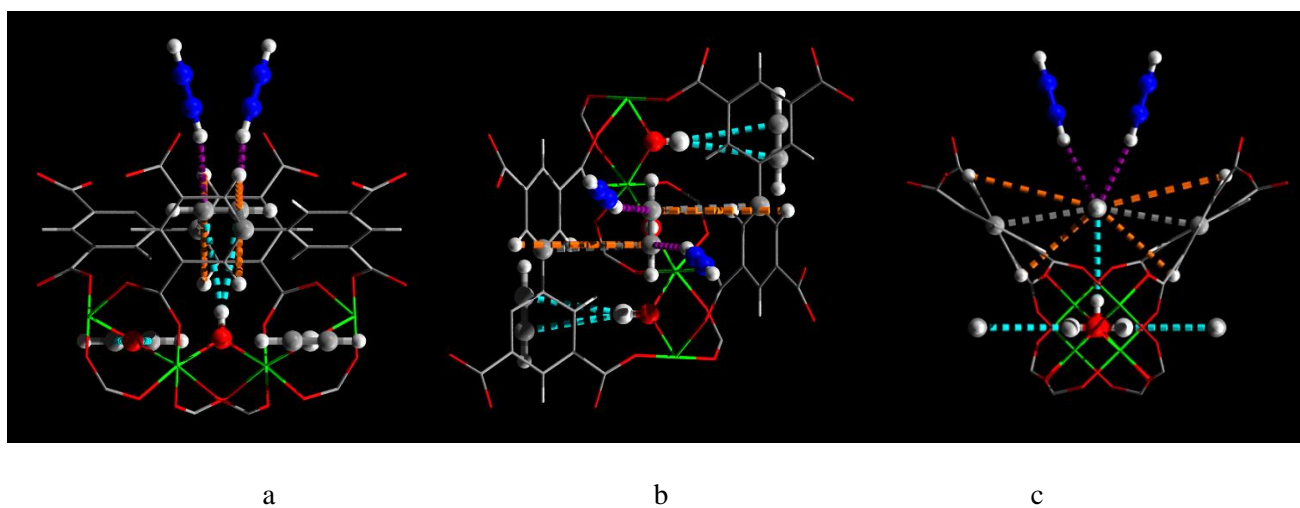
Figure 16. Detailed views of -OH, -CH, and phenyl ring groups binding C_2H_2 molecules in the functionalised cavity of NOTT-300·$4C_2H_2$. Views along (a) the *a*-axis, (b), the *b*-axis and (c) the *c*-axis. The structure was obtained by synchrotron X-ray powder diffraction experiments. The carbon atom on $C_2H_2(II)$ are highlighted in blue. Clear positional disorder for C_2H_2 molecules at Site II was found. The weak hydrogen-bond between $C(\delta-)$ of C_2H_2 and $H(\delta+)$ of -OH is highlighted in cyan, $[C\cdots H = 3.43$ Å$]$. The weak cooperative supramolecular bond between $C(\delta-)$ of C_2H_2 and $H(\delta+)$ from -CH is highlighted in orange, $[C\cdots H = 3.55$, occurring twice$]$. The weak $\pi\cdots\pi$ stacking interaction between π-electrons of C_2H_2 and phenyl rings on the ligand is highlighted in grey $[C\equiv C\cdots C_6 = 3.76$ Å, occurring twice$]$. The weak electrostatic dipole interactions between $C_2H_2(I)$ and $C_2H_2(II)$ molecules are highlighted in purple $[C^{II}\cdots H^{I} = 2.75$ Å$]$. Therefore, in total, four types of weak interactions cooperatively interact together to bind C_2H_2 molecules in the functionalised cavity.
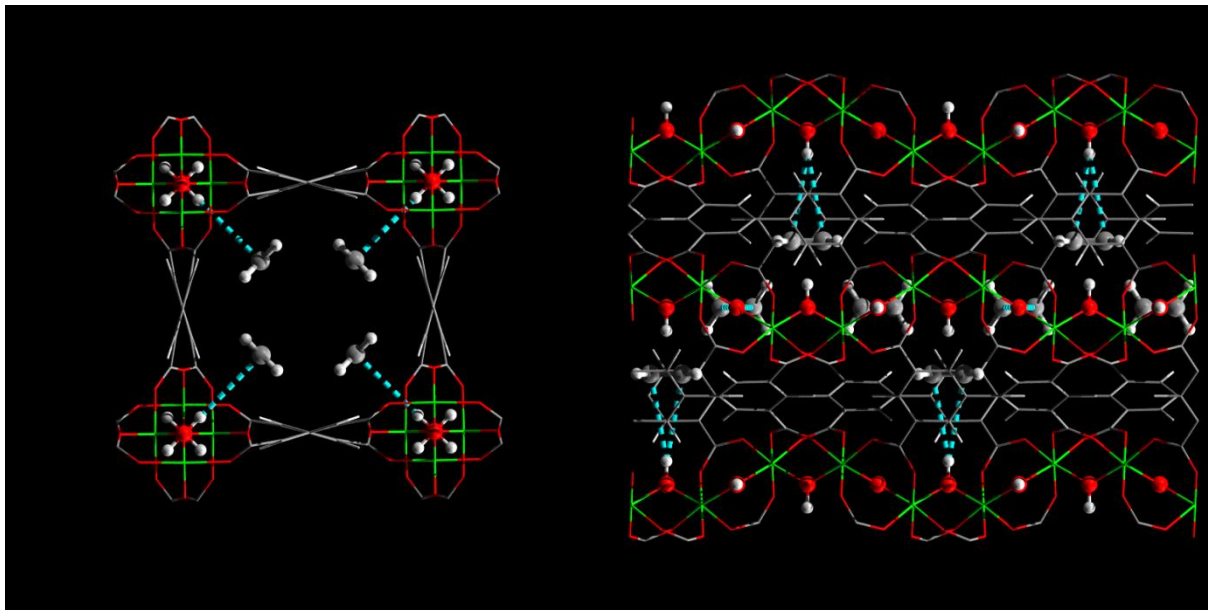
<div align="center">a   b</div>

Figure 17. View of the structure of NOTT-300·C_2H_4G (a) along the c-axis and (b) along the a-axis. The structure was obtained by DFT simulation. The adsorbed C_2H_4 molecules in the pore channel are highlighted by the use of ball-and-stick style.

<div align="center">a   b   c</div>

Figure 18. Detailed views of –OH and phenyl ring groups binding C_2H_4 molecules in the functionalised "pocket" cavity of NOTT-300·C_2H_4G. Views along (a) the *a*-axis, (b), the *b*-axis and (c) the *c*-axis. The structure was obtained by DFT simulation. The weak hydrogen-bond between C(δ-) of C_2H_4 and H(δ+) of -OH is highlighted in cyan, [O···H = 3.71 Å]. The weak π···π stacking interaction between π-electrons of C_2H_4 and phenyl rings on the ligand is highlighted in grey [C≡C···C_6 = 3.82 Å, occurring twice]. Therefore, in total, two types of weak interactions cooperatively interact together to bind C_2H_4 molecules in the functionalised cavity.

a   b

Figure 19. View of the structure of NOTT-300·C_2H_4E (a) along the *c*-axis and (b) along the *a*-axis. The structure was obtained by DFT simulation. The adsorbed C_2H_4 molecules in the pore channel are highlighted by the use of ball-and-stick style.
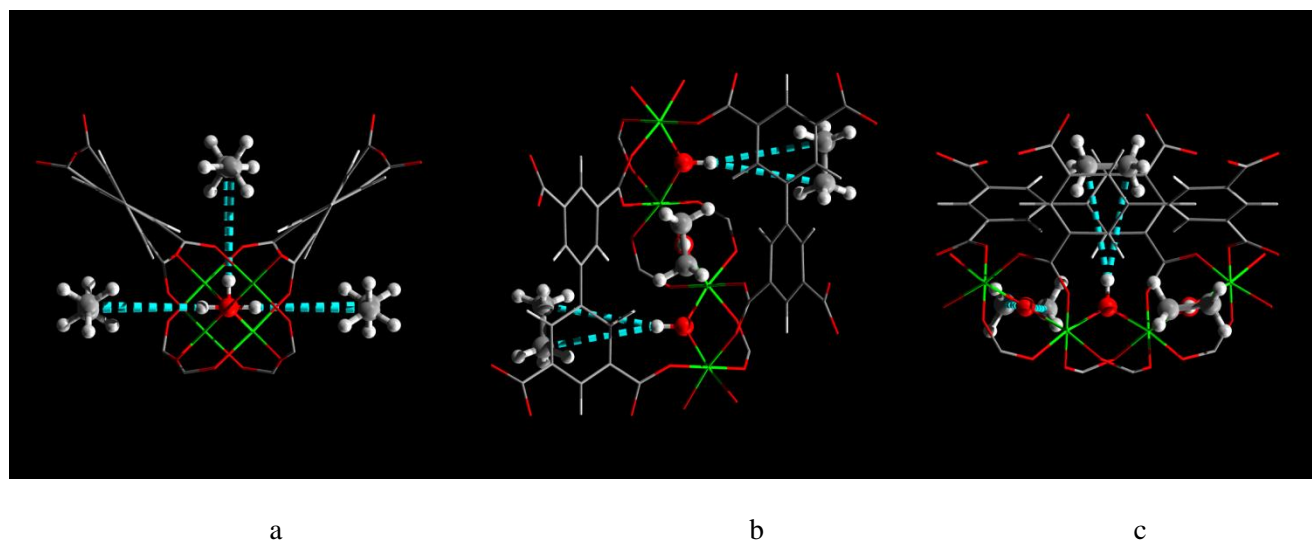
| a | b | c |
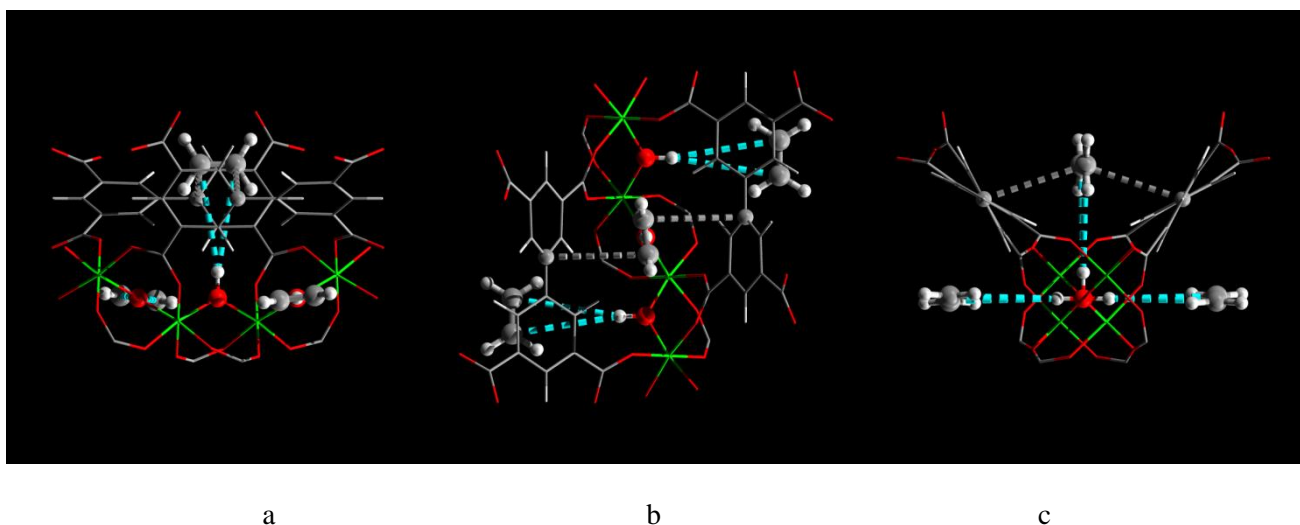
Figure 20. Detailed views of -OH and phenyl ring groups binding C_2H_4 molecules in the functionalised cavity of NOTT-300·C_2H_4E. Views along (a) the *a*-axis, (b), the *b*-axis and (c) the *c*-axis. The structure was obtained by DFT simulation. The weak hydrogen-bond between C(δ-) of C_2H_4 and H(δ+) of -OH is highlighted in cyan, [O$\cdots$H = 4.05 Å]. The weak $\pi\cdots\pi$ stacking interaction between π-electrons of C_2H_4 and phenyl rings on the ligand is highlighted in grey [C$\equiv$C$\cdots$C$_6$ = 4.00 Å, occurring twice]. Therefore, in total, two types of weak interactions cooperatively interact together to bind C_2H_4 molecules in the functionalised cavity.

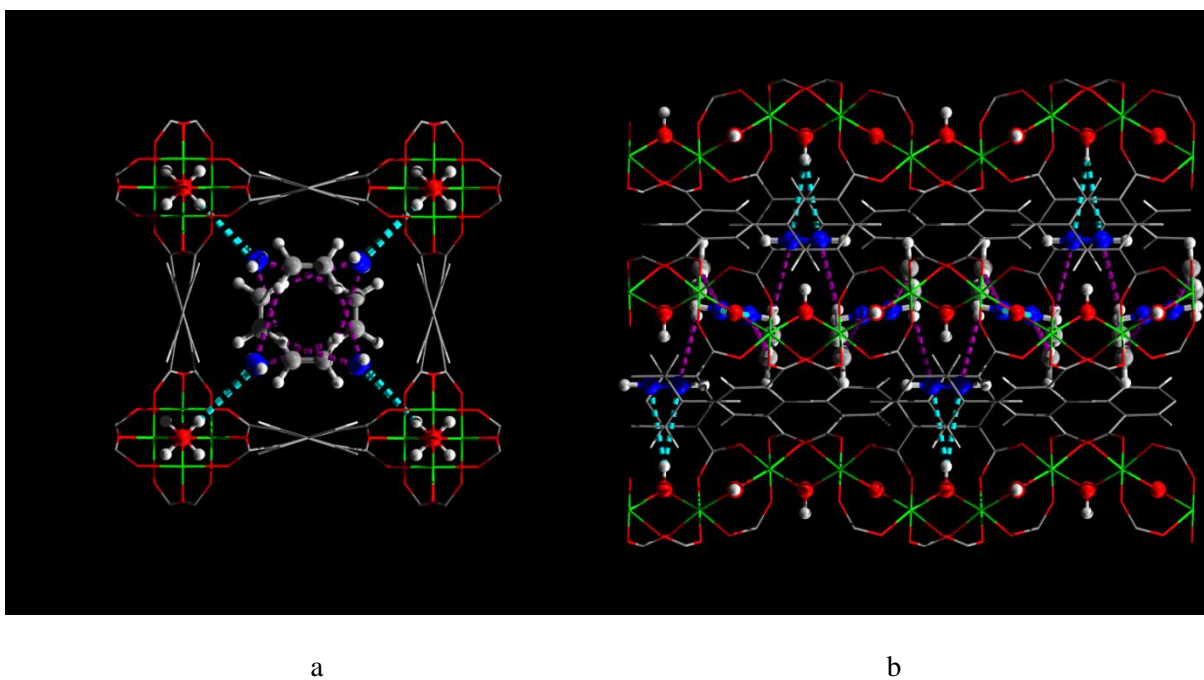a   b

Figure 21. View of the structure of NOTT-300·2.5C_2H_4 (a) along the *c*-axis and (b) along the *a*-axis. The structure was obtained by synchrotron X-ray powder diffraction experiments. In addition to the first site of C_2H_4 molecule, a second site of C_2H_4 (carbon atoms highlighted in blue) was also determined. Both sites present positional disorder for C_2H_4 molecules. The adsorbed C_2H_4 molecules in the pore channel are highlighted by the use of ball-and-stick style.
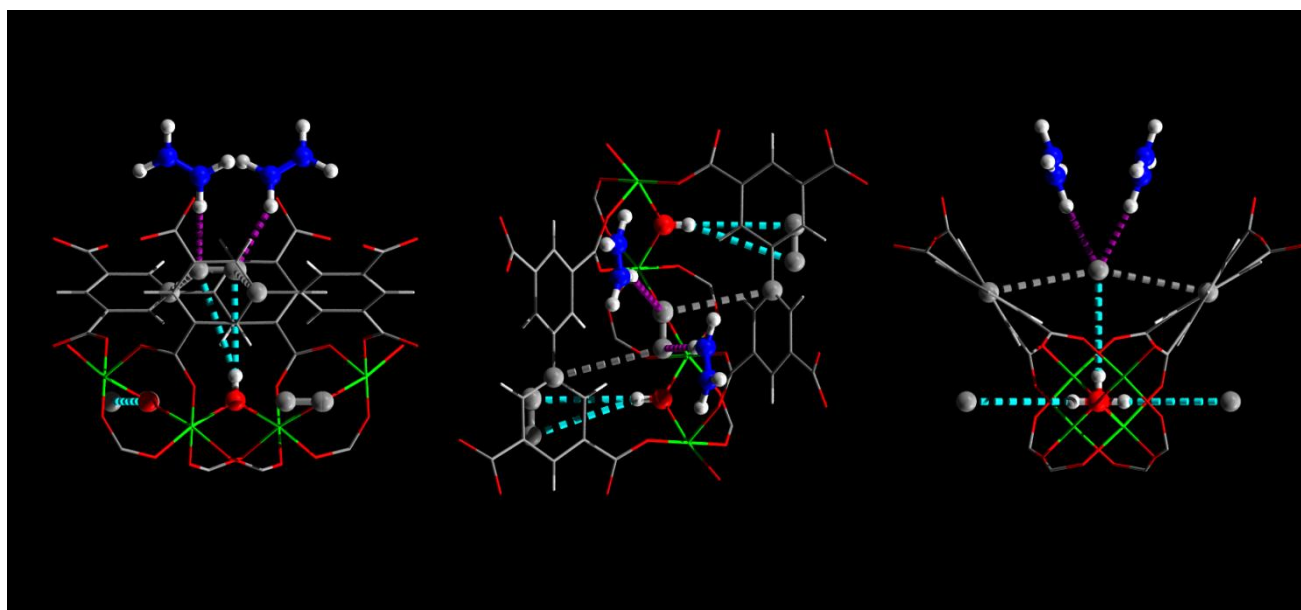
<div align="center">a   b   c</div>

Figure 22. Detailed views of -OH and phenyl ring groups binding C_2H_4 molecules in the functionalised cavity of NOTT-300·2.5C_2H_4. Views along (a) the *a*-axis, (b), the *b*-axis and (c) the *c*-axis. The structure was obtained by synchrotron X-ray powder diffraction experiments. The orientation of the H atoms on C_2H_4(I) was not determined; the orientation of the H atoms on C_2H_4(II) was determined based upon the optimal orientation to form inter-molecular dipole interactions. The weak hydrogen-bond between C(δ-) of C_2H_4(I) and H(δ+) of -OH is highlighted in cyan, [O···H = 3.49, 3.72 Å]. The weak π···π stacking interaction between π-electrons of C_2H_4(I) and phenyl rings on the ligand is highlighted in grey [C≡C···C_6 = 3.86, 3.90 Å]. The weak electrostatic dipole interactions between C_2H_4(I) and C_2H_4(II) molecules are highlighted in purple [C^I···H^{II} = 2.72 Å]. Therefore, in total, three types of weak interactions cooperatively interact together to bind C_2H_4 molecules in the functionalised cavity.

Figure 23. View of the structure of NOTT-300·1.8C_2D_4 (a) along the *c*-axis and (b) along the *a*-axis. The structure was obtained by high resolution neutron powder diffraction, and clear positional disorder for C_2D_4 molecules at both Site I and II can be seen. The adsorbed C_2D_4 molecules in the channel are highlighted by the use of ball-and-stick style. The carbon atoms for C_2D_4(II) molecules are highlighted in blue.
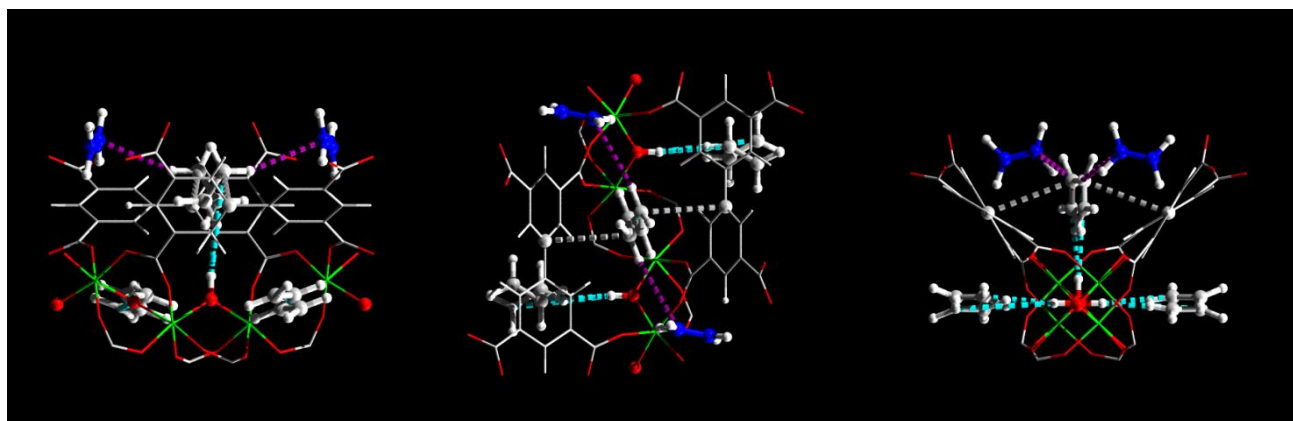
| a | b | c |

Figure 24. Detailed views of –OH, -CH, and phenyl ring groups binding C_2D_4 molecules in the functionalised cavity of NOTT-300·1.8C_2D_4. Views along (a) the a-axis, (b), the b-axis and (c) the c-axis. The structure was obtained by high resolution neutron powder diffraction. Clear positional disorder for C_2D_4 molecules at both Site I and II can be seen, inducing slight differences in bond distances in comparison to the model obtained from DFT/INS study which gives the average position without disorder. The weak hydrogen-bond between C(δ-) of C_2D_4 and H(δ+) of -OH is highlighted in cyan, [C$\cdots$H = 3.46 Å]. The weak $\pi\cdots\pi$ stacking interaction between π-electrons of C_2D_4 and phenyl rings on the ligand is highlighted in grey [C$\equiv$C$\cdots$C$_6$ = 3.82 Å]. The weak electrostatic dipole interactions between C_2D_4(I) and C_2D_4(II) molecules are highlighted in purple [C$^{II}\cdots$D^I = 3.47 Å]. Therefore, in total, four types of weak interactions cooperatively interact together to bind C_2D_4 molecules in the functionalised cavity.

a   b

Figure 25. View of the structure of NOTT-300·0.5C_2H_6 (a) along the *c*-axis and (b) along the *a*-axis. The structure was obtained by DFT simulation. The adsorbed C_2H_6 molecules in the pore channel are highlighted by the use of ball-and-stick style.

| a | b | c |

Figure 26. Detailed views of -OH group binding C_2H_6 molecules in the functionalised cavity of NOTT-300·0.5C_2H_6. Views along (a) the a-axis, (b), the b-axis and (c) the c-axis. The structure was obtained by DFT simulation. The weak hydrogen-bond between C(δ-) of C_2H_6 and H(δ+) of -OH is highlighted in cyan, [O···H = 4.17 Å]. Therefore, only one type of weak interaction binds C_2H_6 molecules in the functionalised cavity.

a   b
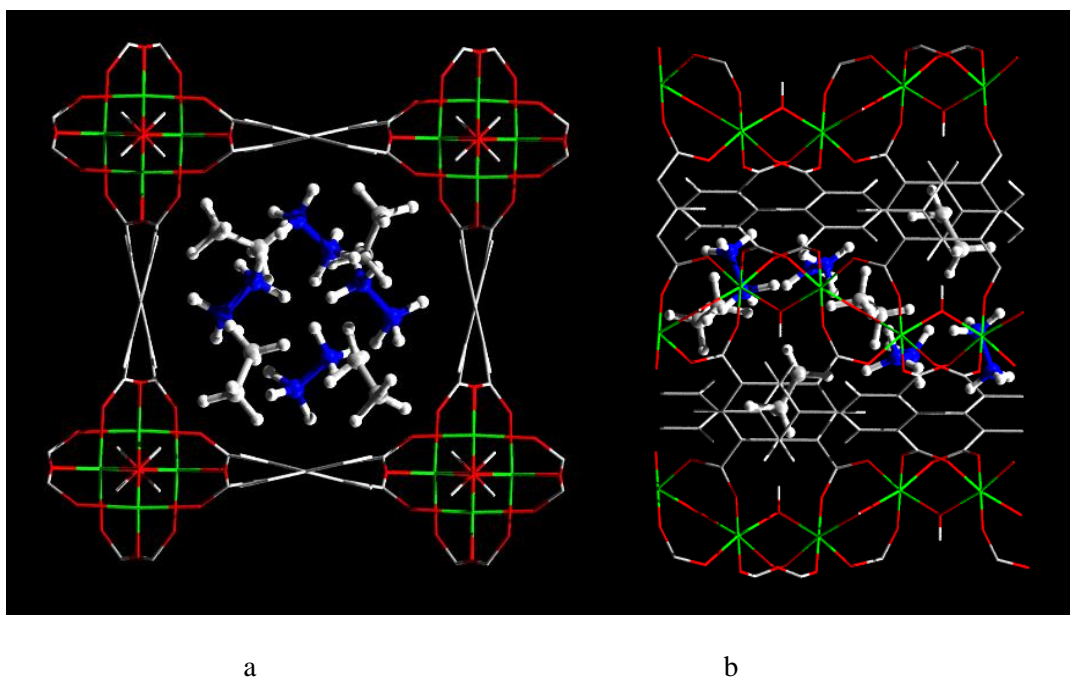
Figure 27. View of the structure of NOTT-300·1.3C_2D_6 (a) along the *c*-axis and (b) along the *a*-axis. The structure was obtained by high resolution neutron powder diffraction, and clear positional disorder for C_2D_6 molecules at both Site I and II can be seen. The adsorbed C_2D_6 molecules in the channel are highlighted by the use of ball-and-stick style. The carbon atoms for C_2D_6(II) molecules are highlighted in blue.

a	b	c
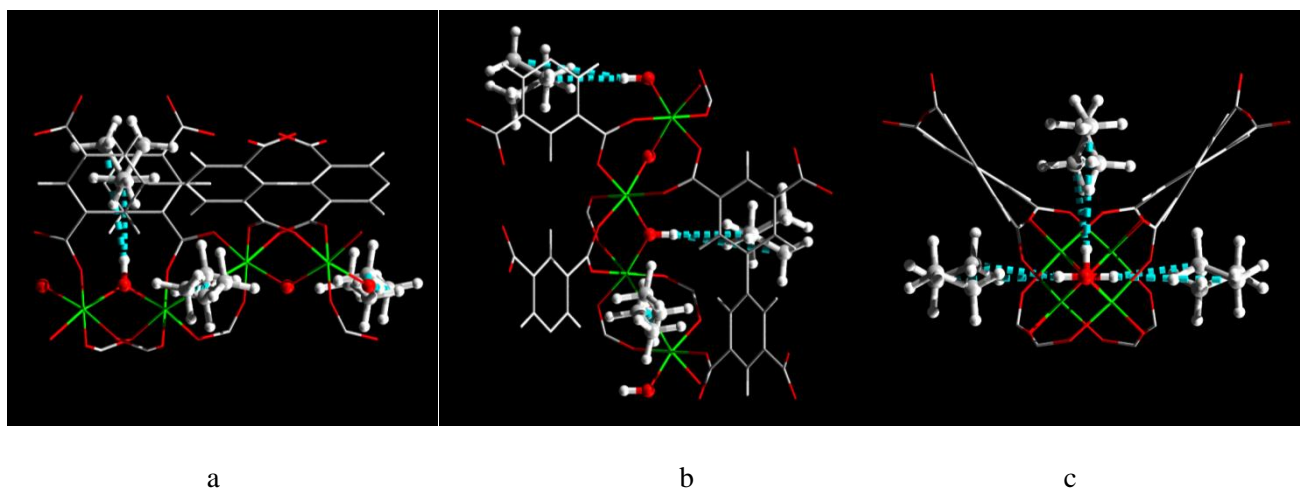
Figure 28. Detailed views of –OH groups binding C_2D_6 molecules in the functionalised cavity of NOTT-300·1.3C_2D_6. Views along (a) the *a*-axis, (b), the *b*-axis and (c) the *c*-axis. The structure was obtained by high resolution neutron powder diffraction. Clear positional disorder for C_2D_6 molecules at both sites I and II can be seen, inducing slight differences in bond distances in comparison to the model obtained from DFT/INS study which gives the average position without disorder. The weak hydrogen-bond between C(δ-) of C_2D_6 and H(δ+) of -OH is highlighted in cyan, [C$\cdots$H = 2.93 - 4.22 Å].

a   b

Figure 29. View of the structure of NOTT-300·2.4C_2H_2·0.8C_2H_4 (a) along the *c*-axis and (b) along the *a*-axis. The structure was obtained by DFT simulation. The adsorbed C_2H_2 and C_2H_4 molecules in the pore channel are highlighted by the use of ball-and-stick style.
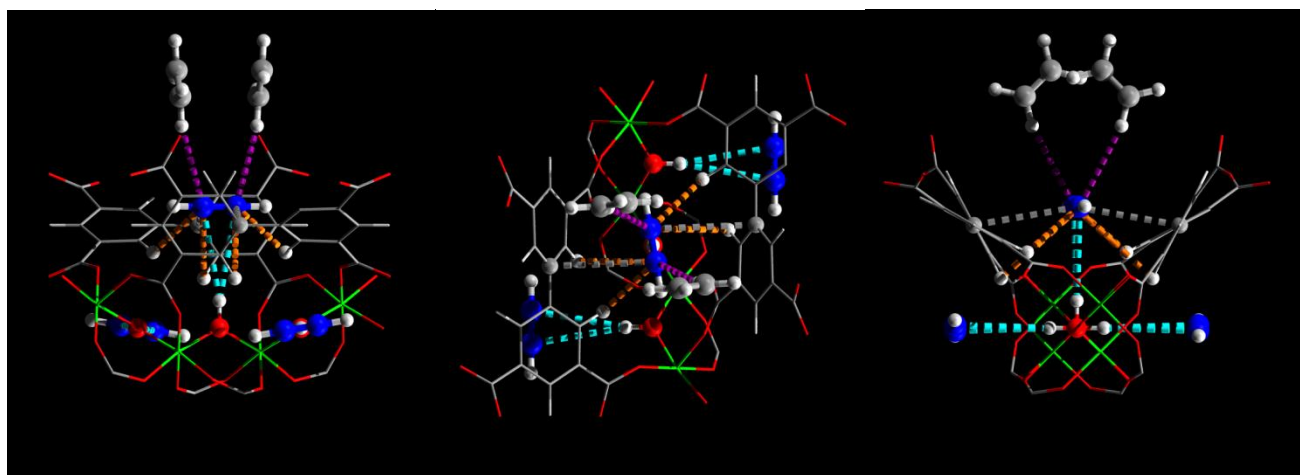
a   b   c

Figure 30. Detailed views of -OH, -CH, and phenyl ring groups binding C_2H_2 and C_2H_4 molecules in the functionalised cavity of NOTT-300·2.4C_2H_2·0.8C_2H_4. Views along (a) the *a*-axis, (b), the *b*-axis and (c) the *c*-axis. The structure was obtained by DFT simulation. The weak hydrogen-bond between C(δ-) of C_2H_2 and H(δ+) of -OH is highlighted in cyan, [O···H = 3.45 Å]. The weak cooperative supramolecular bond between C(δ-) of C_2H_2 and H(δ+) from -CH is highlighted in orange, [O···H = 3.08, 3.93 Å with each occurring twice]. The weak π···π stacking interaction between π-electrons of C_2H_2 and phenyl rings on the ligand is highlighted in grey [C≡C···C_6 = 3.87 Å, occurring twice]. The weak electrostatic dipole interactions between C_2H_2 and C_2H_4 molecules are highlighted in purple [C^a···H^e = 3.37 Å; occurring twice]. Therefore, in total, four types of weak interactions cooperatively interact together to bind C_2H_2 and C_2H_4 molecules in the functionalised cavity.

5.   Additional Gas Sorption Isotherm Plots for NOTT-300
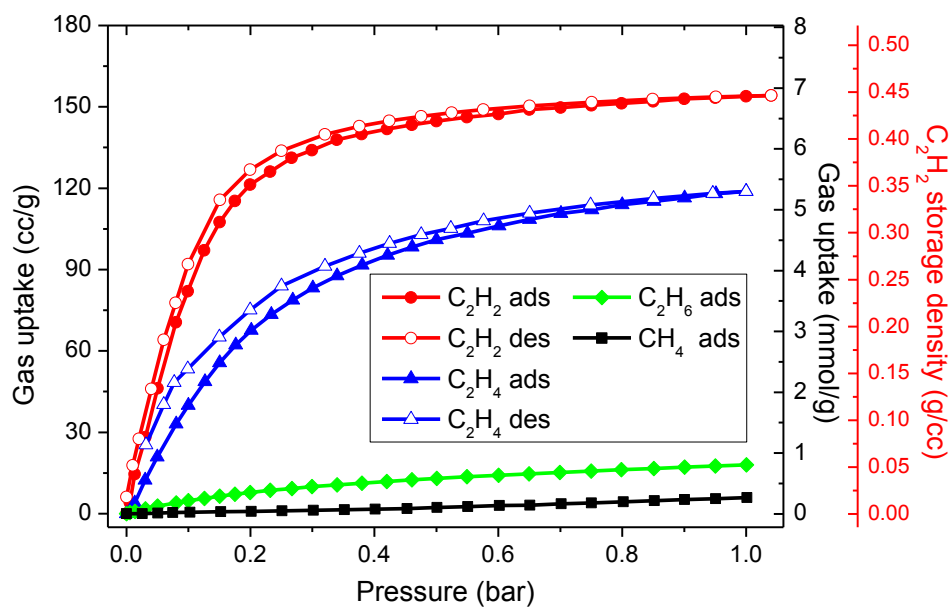
a
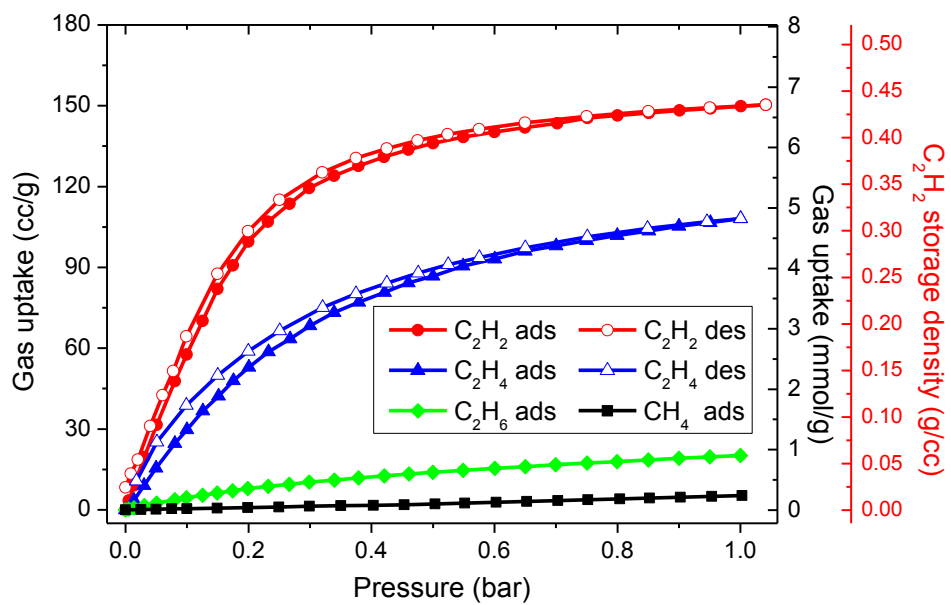
b
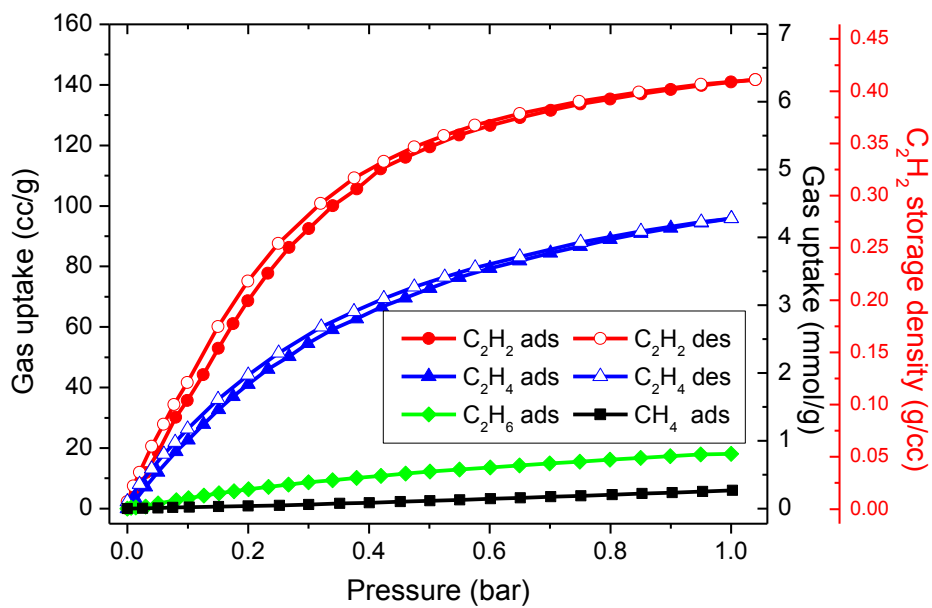
c
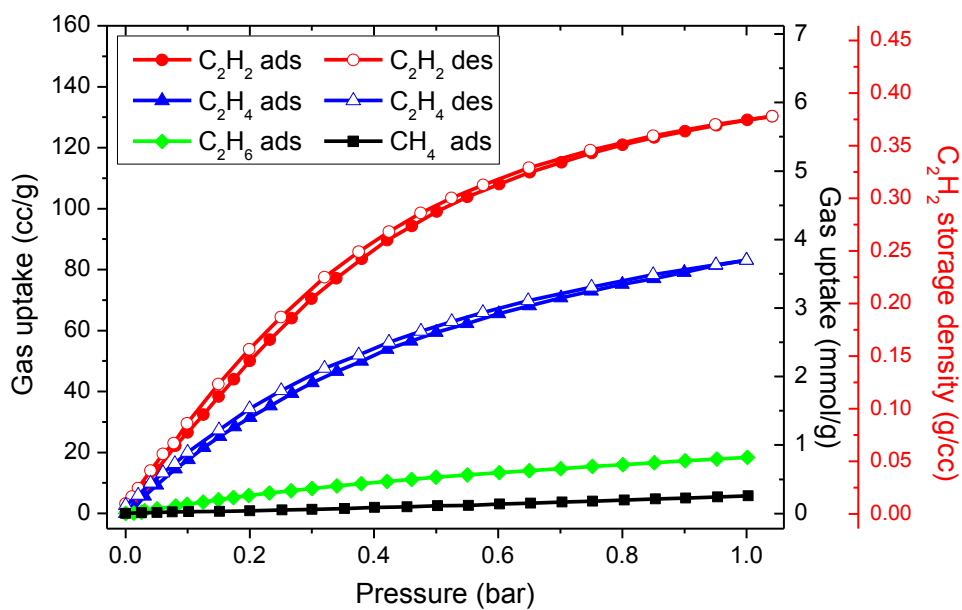
d

Figure 31. Comparison of the gas adsorption isotherms for NOTT-300 at (a) 273 K, (b) 283 K, (c) 293 K and (d) 303 K up to 1.0 bar. NOTT-300 exhibits high, moderate, low and extremely low uptakes for C_2H_2, C_2H_4, C_2H_6 and CH_4, respectively.
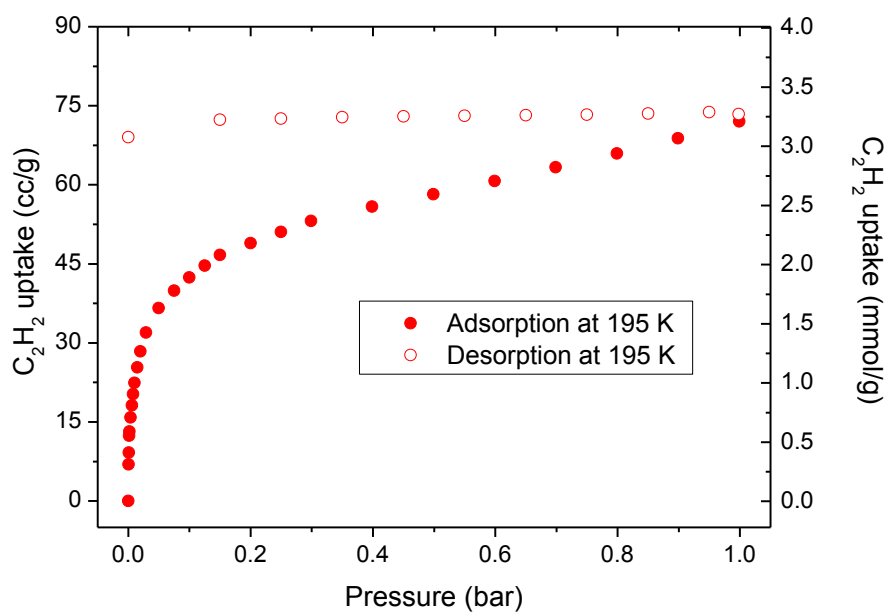
Figure 32. C_2H_2 adsorption isotherm for NOTT-300 at 195 K. In comparison to the isotherm at 273 K, reduced total uptake of C_2H_2 was observed as a result of an increased diffusion barrier at 195 K. This is also evidenced by the hysteretic desorption of C_2H_2 from NOTT-300 as a result of kinetic trapping.
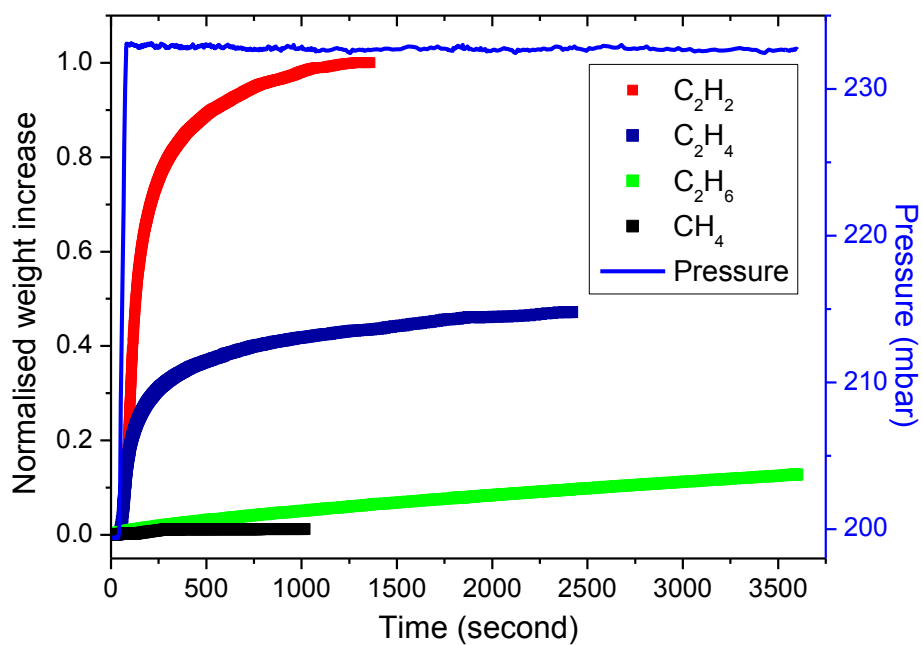
Figure 33. Kinetics for adsorption of hydrocarbons in NOTT-300 at 293 K and 0.2 bar.
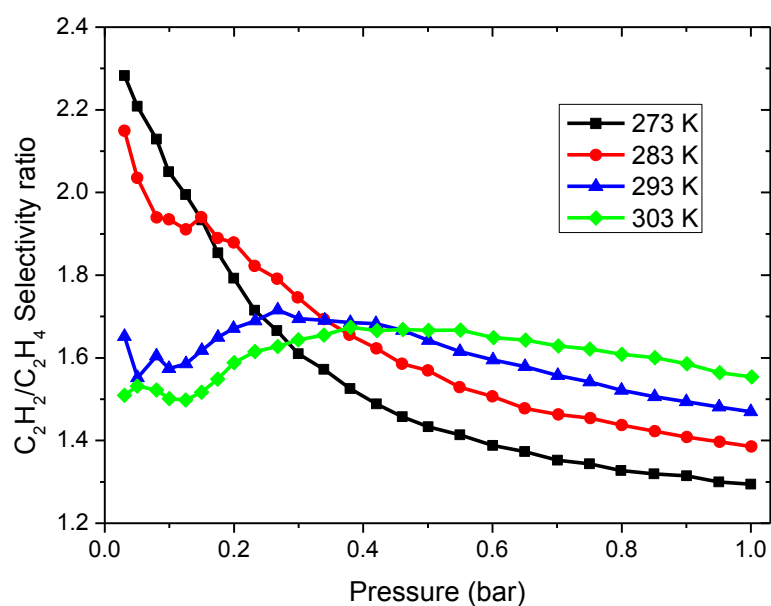
Figure 34. The uptake ratios of C_2H_2 vs C_2H_4 for NOTT-300 at 273-303 K as a function of pressure. At low pressure, NOTT-300 shows higher selectivity at lower temperature. With increasing pressure NOTT-300 shows higher selectivity at higher temperature. This anomalous trend suggests that the rate of the decrease in the uptake in NOTT-300 as temperature increases is greater for alkene than alkyne, indicating that the nature of the binding interactions in NOTT-300/alkyne and NOTT-300/alkene is different.
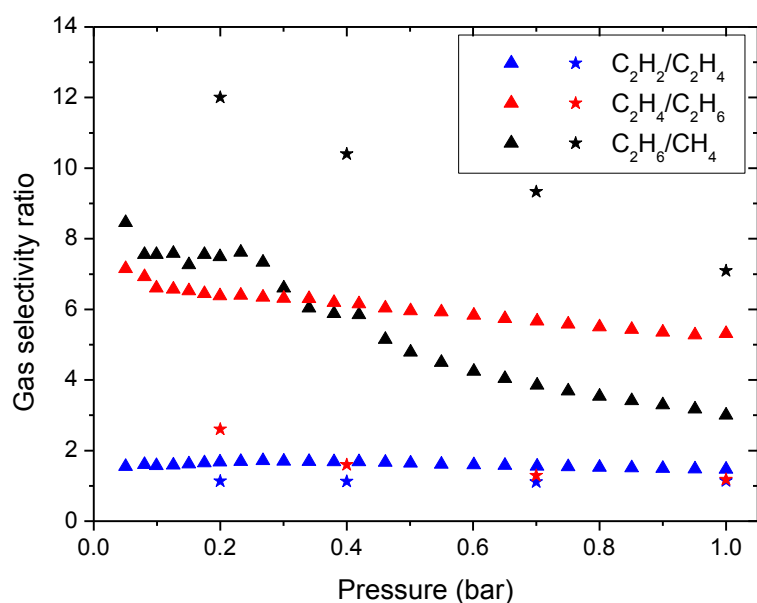
Figure 35. Comparison of the uptake ratios for C_2H_2 vs C_2H_4, C_2H_4 vs C_2H_6, and C_2H_6 vs CH_4 as a function of pressures. Data were obtained by direct comparison of the ratio between total uptakes for different hydrocarbons at a given pressure. Triangles represent the data for NOTT-300 and stars show the data of [Fe$_2$(dobdc)].[9]

6. Additional Inelastic Neutron Scattering (INS) Spectra and analysis

In this study, we have successfully combined INS and DFT to visualise adsorbed C_2H_2, C_2H_4, and C_2H_6 molecules within NOTT-300 by investigating the change in the ***dynamics*** of the hydrogen atoms of both guest hydrocarbon molecules and the local MOF host, including those of the hydroxyl groups and benzene rings of the ligand.

In comparison to the INS spectra for condensed C_2H_2 in the solid state, peaks III and IV are attributed to symmetric and asymmetric C-H vibrational motions of C_2H_2 molecules, respectively. Peaks III and IV are changed compared to free C_2H_2, from singlets to doublets, indicating the removal of the degeneracy of the vibration upon binding of C_2H_2 to the host (Supplementary Figure 36). This change in peak profile is also predicted by DFT calculations (Supplementary Figure 37). Moreover, these two peaks are slightly shifted to lower energies in NOTT-$300 \cdot 3C_2H_2$ compared to free C_2H_2, indicating a restriction on the vibrational motion for adsorbed C_2H_2 molecules, consistent with the formation of a number of weak supramolecular bonds.

To probe further into this change in the degeneracy of the C-H vibration, the π-orbitals (*Py* and *Pz*, assuming *Px* forms the σ bond) of C_2H_2 molecules need to be considered (Supplementary Figure 38). According to the orientation of the π-orbitals, two models (I and II) of the C_2H_2 binding to free -OH group can be developed (Supplementary Figures 39-40). In model I, *Py* and *Pz* orbitals of C_2H_2 approach –OH group equally. Because of the π-electron density of C_2H_2, relatively strong $\pi\cdots\pi$ stacking interaction is formed to primarily stabilise this binding and the $\pi\cdots$HO hydrogen-bond is weaken. In contrast, in model II, *Py* and *Pz* orbitals of C_2H_2 approach –OH group differently, resulting in a splitting of the degeneracy of the π-orbitals. In this orientation, relatively strong $\pi\cdots$HO hydrogen-bond is formed to primarily stabilise this binding and the $\pi\cdots\pi$ stacking interaction is weaken. The splitting of the INS peaks therefore clearly indicates that $\pi\cdots$HO hydrogen-bond in model II is dominating the C_2H_2 binding to the –OH groups.

In addition to the INS study of NOTT-$300 \cdot 3C_2H_2$, we also sought to study the binding dynamics for NOTT-300 with C_2H_2 at a lower loading (Supplementary Figure 41). In comparison to the INS of NOTT-$300 \cdot 3C_2H_2$, INS spectra for NOTT-$300 \cdot 1C_2H_2$ has lower overall scattering intensity due to the reduced loading. There is, however, little difference in scattering features between the high and low loadings of C_2H_2 in NOTT-300, suggesting no significant change in the binding mechanism throughout the adsorption. This is evidenced by the difference spectra (Supplementary Figure 41). The five major changes (Peaks I to V) of the difference INS spectra of NOTT-$300 \cdot 3C_2H_2$ are all present in the difference spectra of NOTT-$300 \cdot 1C_2H_2$ (referenced to bare NOTT-300). A closer examination suggests Peaks I, III, IV, associated with translational, symmetric and asymmetric vibrational motion of the C-H bond, respectively, have reduced intensity as a result of reduced C_2H_2 loading. An interesting observation is Peak II and V-VI, associated with the changes of vibrational motion of –OH and aromatic –CH

groups of the host framework, changed differently as a function of C_2H_2 loading: Peak II barely changes while Peak V-VI exhibit increased intensity on going from NOTT-300·$1C_2H_2$ to NOTT-300·$3C_2H_2$. This result suggests that the binding of C_2H_2 to Al–OH group occurs from low loading and these free –OH sites saturate quickly with increased C_2H_2 adsorption. At higher loading, adsorbed C_2H_2 molecules start to populate on the 2nd site (*i.e.*, in the middle of the pore, more close to the phenyl rings of ligands) and this triggers more significant changes in the molecular motion of the aromatic hydrocarbon atoms on the phenyl ring. Therefore, comparison of these INS spectra confirms that the Al-OH moiety acts as relatively strong binding site to C_2H_2 due to the cooperative supramolecular interactions. This is also consistent with the observed higher occupancy for the C_2D_2 molecules bound to Al-OH group than that of 2nd site packed inside the channel in NOTT-300·$2.7C_2D_2$ studied by neutron powder diffraction. Moreover, splitting of the Peaks III and IV are also observed at lower C_2H_2 loading (Supplementary Figure 42b), confirming the interaction between π electrons (δ-) of C_2H_2 molecules and the –OH(δ+) group and the associated removal of degeneracy of the vibrational modes for C-H bond in C_2H_2.

In the INS study of NOTT-300 loaded with an equimolar mixture of C_2H_2/C_2H_4, although the adsorption equilibrium was achieved at room temperature and the sample cell was isolated and sealed before cooling, it is very challenging to definitively conclude whether there was any guest rearrangement during the cooling process. In particular, C_2H_2 and C_2H_4 have different boiling points (Supplementary Table 12) and adsorption of C_2H_2 and C_2H_4 in NOTT-300 gives different isosteric heats of adsorption (Figure 1f). In order to gauge the effect of thermodynamics on the uptake of the gas mixture and the possible shift of adsorption equilibrium during cooling, we have designed and completed the following experiment to study the intermolecular exchange of C_2H_2 and C_2H_4 in the pore of NOTT-300, and to gain more insight into the intermolecular adsorbate-exchange in NOTT-300.

Desolvated NOTT-300 was loaded with pure C_2H_4 to generate NOTT-300·$1C_2H_4$ at room temperature before the sample cell was isolated, sealed and cooled down to below 10 K. An INS spectrum (denoted as NOTT-300·$1C_2H_4$ in Supplementary Figure 43) of C_2H_4-loaded NOTT-300 was collected at ~7 K. The sample cell was then warmed to room temperature and opened to a pure C_2H_2 reservoir containing approximately equal amount of C_2H_2 gas to allow the intermolecular exchange between adsorbed C_2H_4 in NOTT-300 and free C_2H_2 molecules in gas phase. The connection was left open for 3 hours and the sample cell was then slowly cooled to ~200 K when the cell was isolated and sealed. Since C_2H_2 has a higher isosteric heat of adsorption (Figure 1f) and is in large excess in the gas phase, it is expected significant intermolecular guest exchange will happen, leading to a C_2H_2/C_2H_4 mixture loaded NOTT-300 with mixed site occupancy upon equilibrium. The sample cell was then cooled to below 10 K for INS spectrum collection (denoted as NOTT-300·$1C_2H_4$ reacted with C_2H_2 in Supplementary Figure 43). Very surprisingly, INS spectra for C_2H_4 loaded NOTT-300 and the NOTT-300·$1C_2H_4$ post-C_2H_2 exchange look almost identical (Supplementary Figure 43) and the corresponding difference spectra (referenced with bare NOTT-300 as

background) confirm only the recoil/rotational motion of C_2H_4 in the pore as dominating feature with barely detectable sign of presence of adsorbed C_2H_2 molecules in the pore (Supplementary Figure 44). This experiment suggests that intermolecular exchange of hydrocarbon molecules after equilibrium has been achieved is negligible in NOTT-300 during the cooling process. Clearly in addition to thermodynamics, kinetics (*i.e.,* diffusion of hydrocarbons in the pore) also plays an important role in establishing the adsorption equilibrium. In the case of hydrocarbon adsorption in NOTT-300, the difference in isosteric heats of adsorption is not sufficient to overcome the large diffusion barrier, and therefore, intermolecular guest exchange was not observed in NOTT-300. It is worth mentioning that at lower temperatures the effect of any diffusion barrier will become more significant. Therefore, the neutron scattering analysis of NOTT-300 loaded with a C_2H_2/C_2H_4 mixture at ~7 K represents the actual equilibrium achieved at room temperature for competing binding in NOTT-300. This result is also consistent with the selectivity obtained from IAST analysis and mixed gas adsorption experiments.

To probe further into the discrepancy between experimental and calculated difference INS spectra for C_2H_2 loaded NOTT-300 (Supplementary Figure 45a), additional DFT calculations with van der Waals corrections taken into account were undertaken (Supplementary Figure 45b). Comparison of the calculated INS spectra with and without van der Waals correction does not show significant changes. This observation confirms that the vibrational properties of the solid material involved and measured are not determined by the soft interactions, such as van der Waals interactions. For example, zero point energy and thermodynamic effects are mostly ignored. This conclusion is also evidenced by calculations with and without van der Waals correction to condensed C_2H_2 in solid state. Indeed, very similar results were obtained from the two calculations (Supplementary Figure 46), confirming the minimal effect of van der Waals interactions to the vibrational properties of the solid material. The small discrepancy between experimental and calculated difference INS spectra for C_2H_2 loaded NOTT-300 (Supplementary Figure 45a) can be due to a number of factors. The calculations do not consider the positional disorder of the guest molecules in the pore owing to thermal motion. Additionally, not all the void space within a porous material is necessarily accessible by the gaseous substrate upon gas loading, and the powder sample may not correspond precisely to the ideal structure model optimised by calculations owing to the framework collapse, or there may be some residual free solvent molecules in the pore.
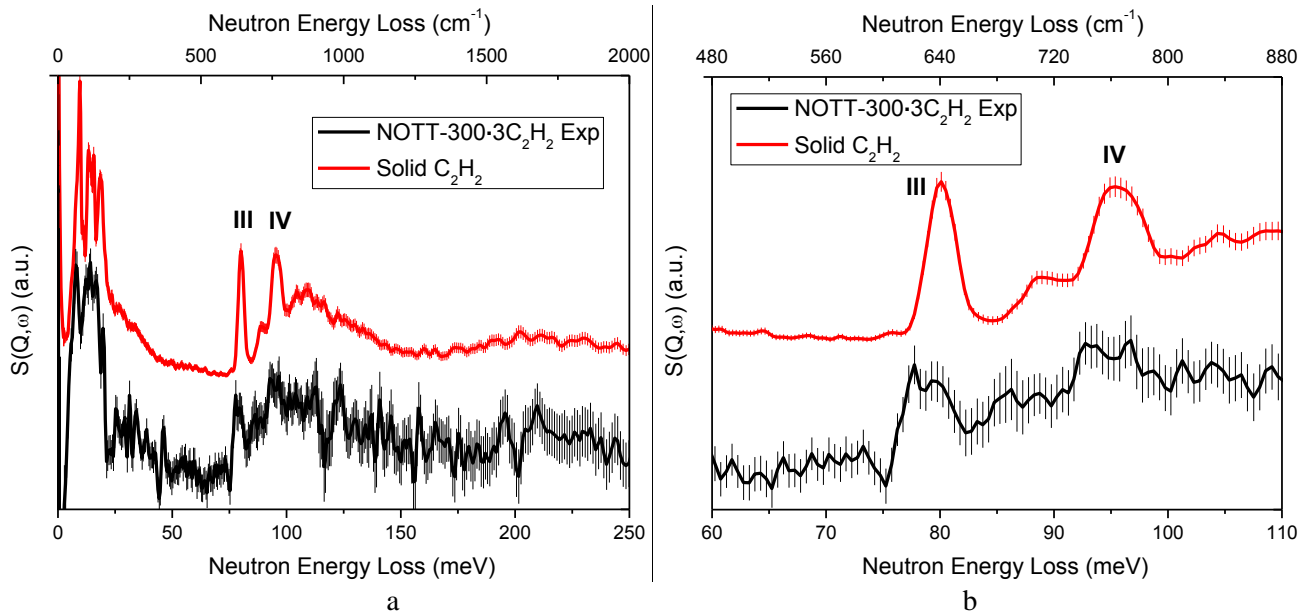
Figure 36. Comparison of the difference plot for experimental INS spectra of bare NOTT-300 and the C_2H_2-loaded NOTT-300 and experimental INS spectra for condensed C_2H_2 in solid; peaks III and IV at 60-110 meV are scaled up in (b).
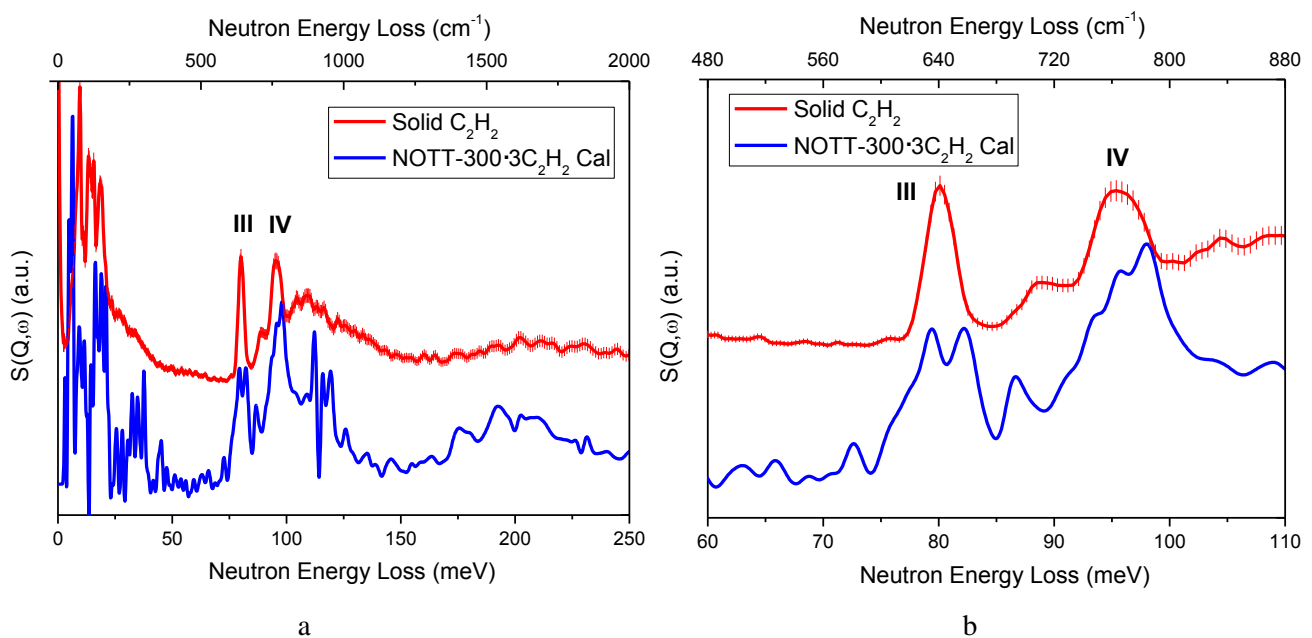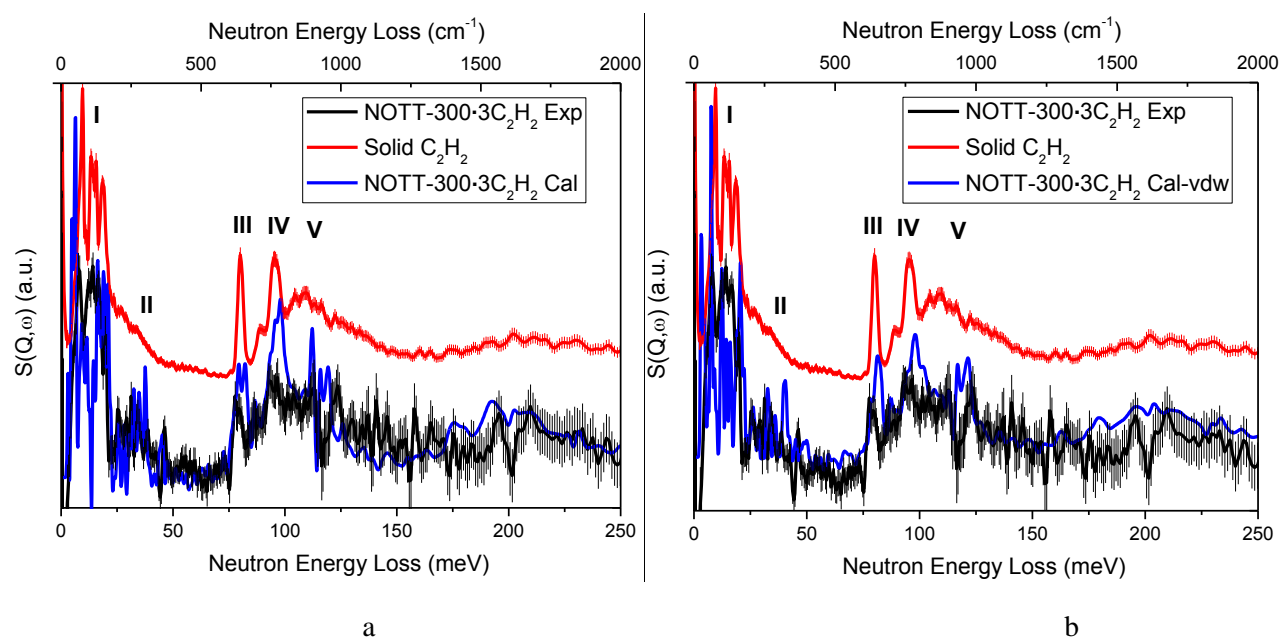

Figure 37. Comparison of the difference plot for calculated INS spectra of bare NOTT-300 and the C_2H_2-loaded NOTT-300 and experimental INS spectra for condensed C_2H_2 in solid; peaks III and IV at 60-110 meV are scaled up in (b).
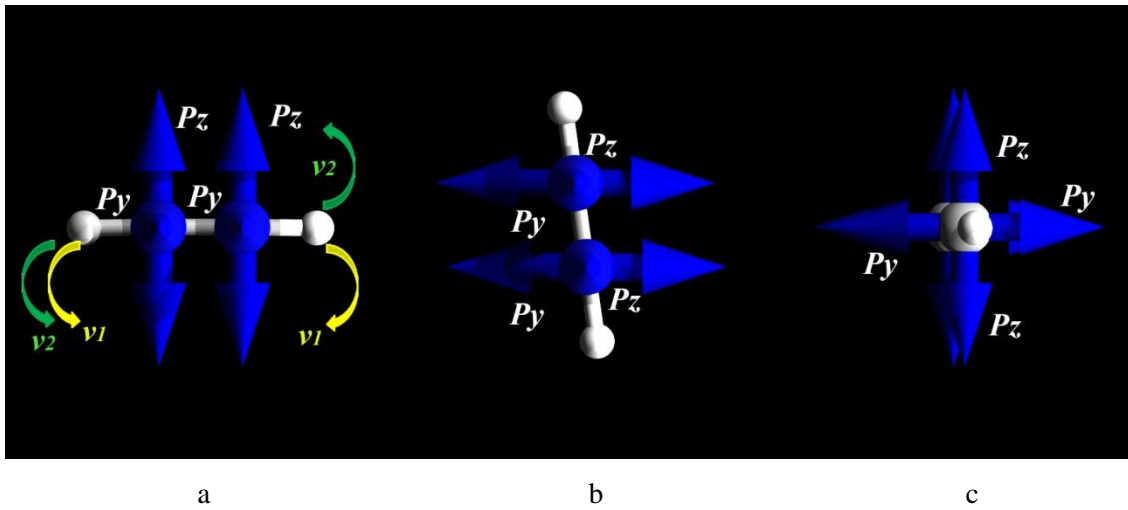
Figure 38. Views of the π-orbitals of *Py*, *Pz* for free C_2H_2 molecules along (a) the *a*-axis, (b), the *b*-axis and (c) the *c*-axis (*Py* and *Pz* orbitals are highlighted in blue). *Py* and *Pz* are equivalent to each other in free C_2H_2 molecules.
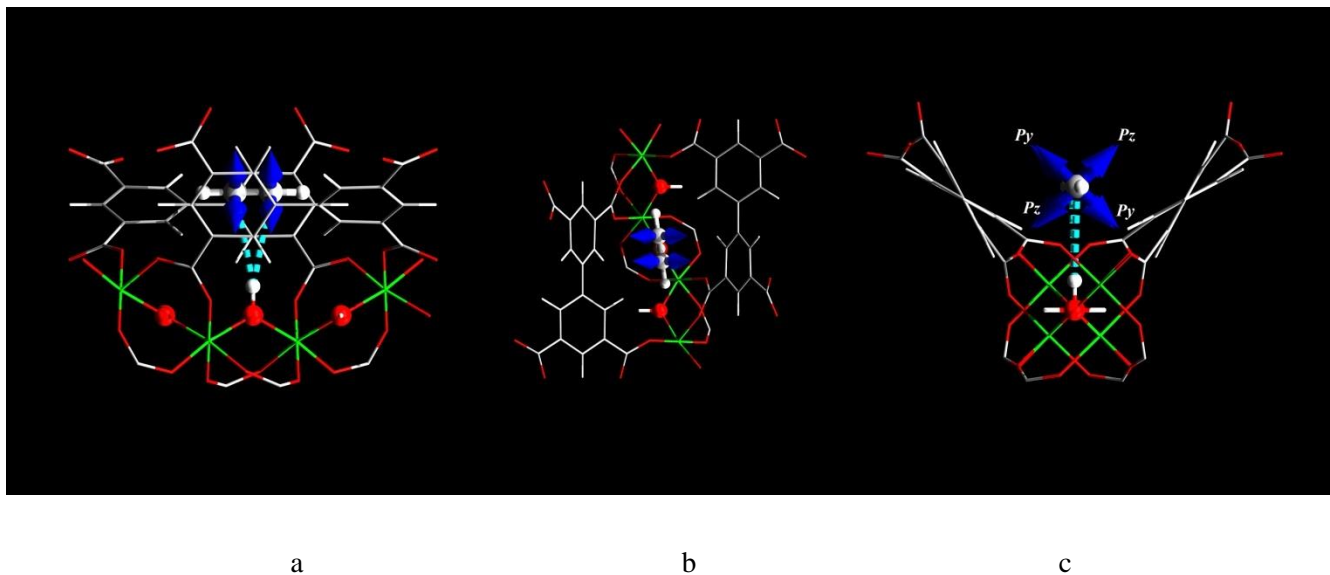
Figure 39. Model I: views of the π-orbitals of *Py*, *Pz* for adsorbed C_2H_2 molecules along (a) the *a*-axis, (b), the *b*-axis and (c) the *c*-axis (*Py* and *Pz* orbitals are highlighted in blue). *Py* and *Pz* are equivalent to each other upon adsorption in this mode, giving no change in degeneracy of the C-H vibrations.
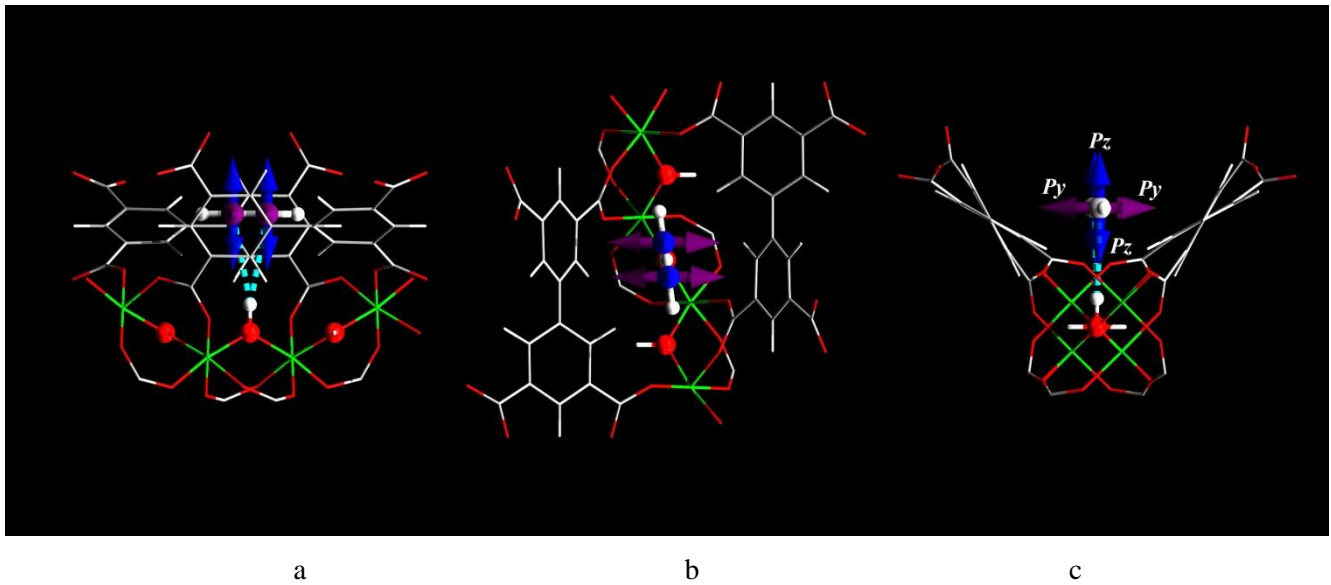
Figure 40. Model II: views of the π-orbitals of *Py*, *Pz* for adsorbed C$_2$H$_2$ molecules along (a) the *a*-axis, (b), the *b*-axis and (c) the *c*-axis (*Py* and *Pz* orbitals are highlighted in purple and blue, respectively). *Py* and *Pz* are not equivalent to each other upon adsorption in this mode, leading to removal of degeneracy of the C-H vibrations.
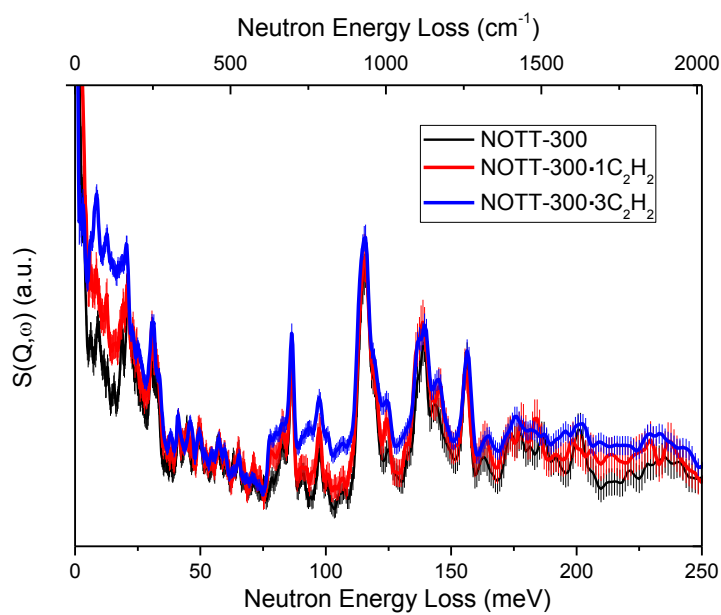
Figure 41. Comparison of the INS spectra for bare NOTT-300, NOTT-300·1C$_2$H$_2$, and NOTT-300·3C$_2$H$_2$. Data were measured at below 10 K.
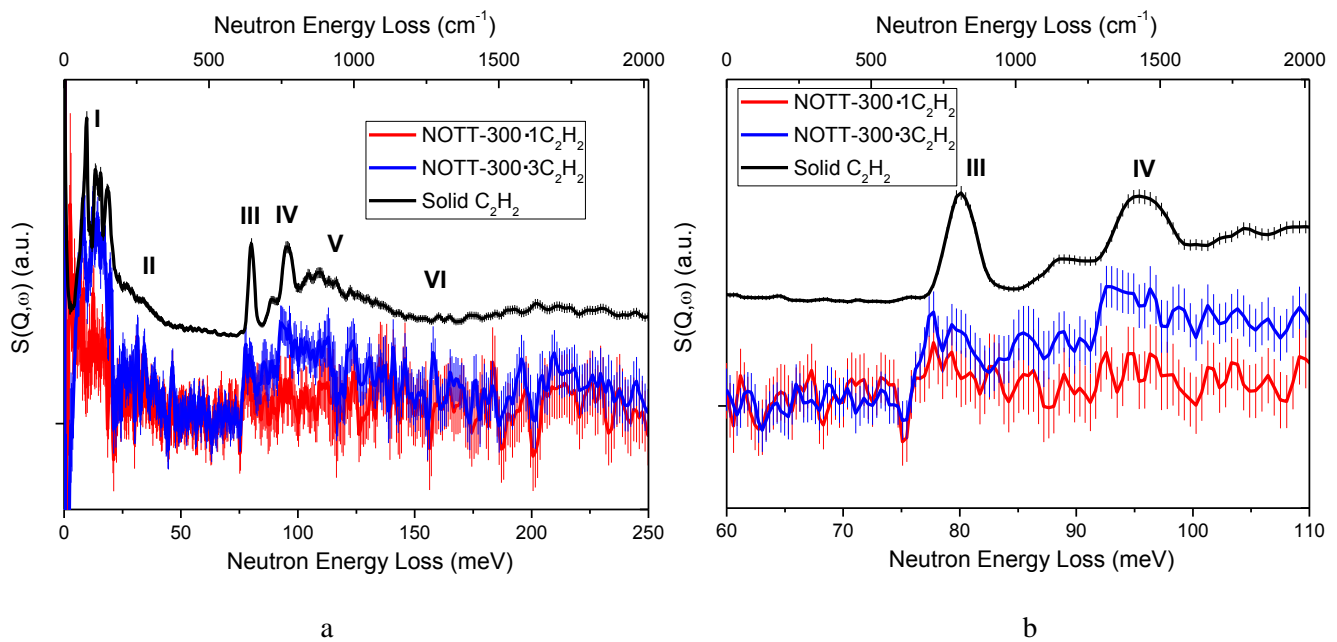
Figure 42. (a) Comparison of the difference INS spectra of NOTT-300·1C$_2$H$_2$ and NOTT-300·3C$_2$H$_2$ with bare NOTT-300 as background, and the INS spectra of condensed C$_2$H$_2$ in the solid state; peaks III and IV at 60-110 meV are scaled up in (b).
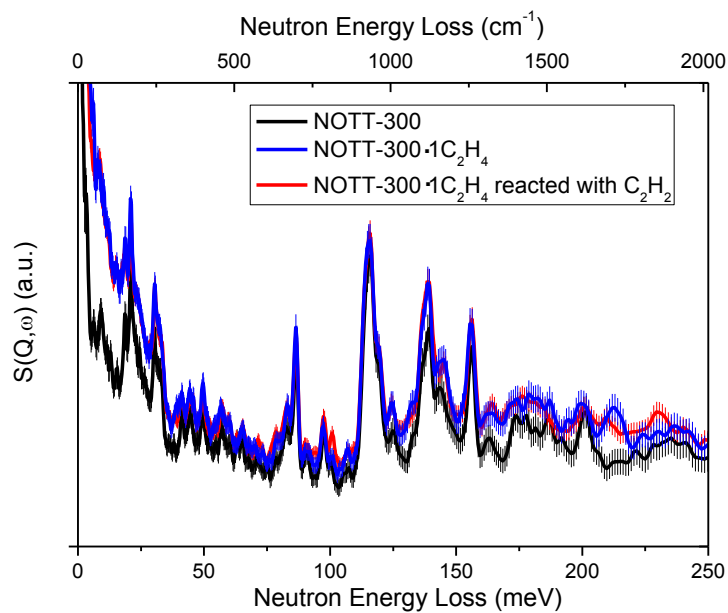
Figure 43. Comparison of the INS spectra for bare NOTT-300, NOTT-300·1C$_2$H$_4$, and NOTT-300·1C$_2$H$_4$ reacted with C$_2$H$_2$. Data were measured at below 10 K.
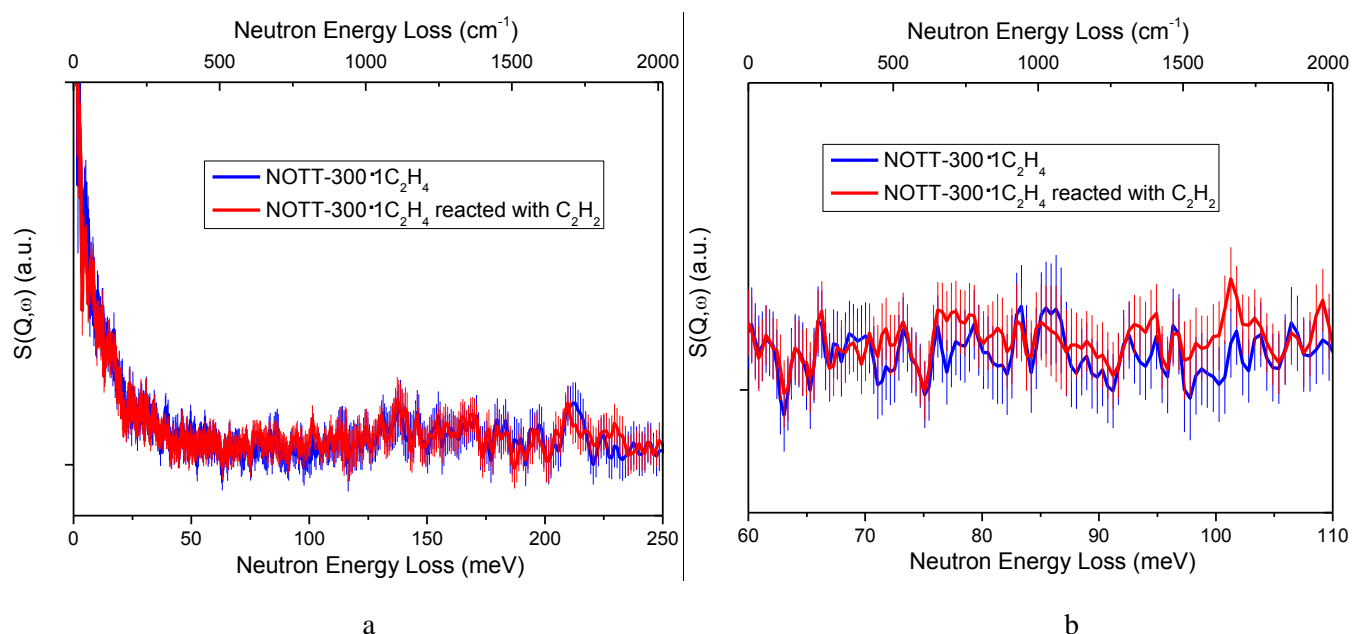
Figure 44. (a) Comparison of the difference INS spectra of NOTT-300·1C₂H₄ and NOTT-300·1C₂H₄ reacted with C₂H₂ with bare NOTT-300 as background; spectra at 60-110 meV are scaled up in (b) to confirm the absence of distinct symmetric and asymmetric vibration of C-H bond of C₂H₂, and thus suggesting very small amount of C₂H₂ was exchanged.

Figure 45. Comparison of the difference plots for experimental INS spectra of bare NOTT-300 and C₂H₂-loaded NOTT-300, and the experimental INS spectra of condensed C₂H₂ in the solid state. The difference plots for DFT calculated INS spectra of bare and the C₂H₂-loaded NOTT-300 without (a) and with (b) van der Waals correction are also shown. In general, no significant change for calculated INS spectra was observed with van der Waals correction taken into account.
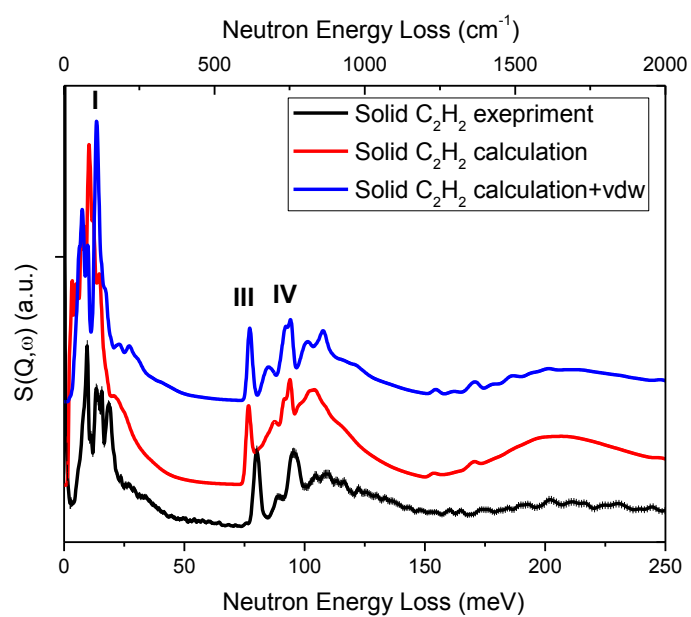
Figure 46. Comparison of the experimental and calculated INS spectra of condensed C_2H_2 in the solid state. Comparison of the calculated spectra with and without van der Waals correction is shown. In general, no significant change for calculated INS spectra was observed with van der Waals correction taken into account.

7.   **Views of Crystal Structures for solid C_2H_2 and C_2H_4**
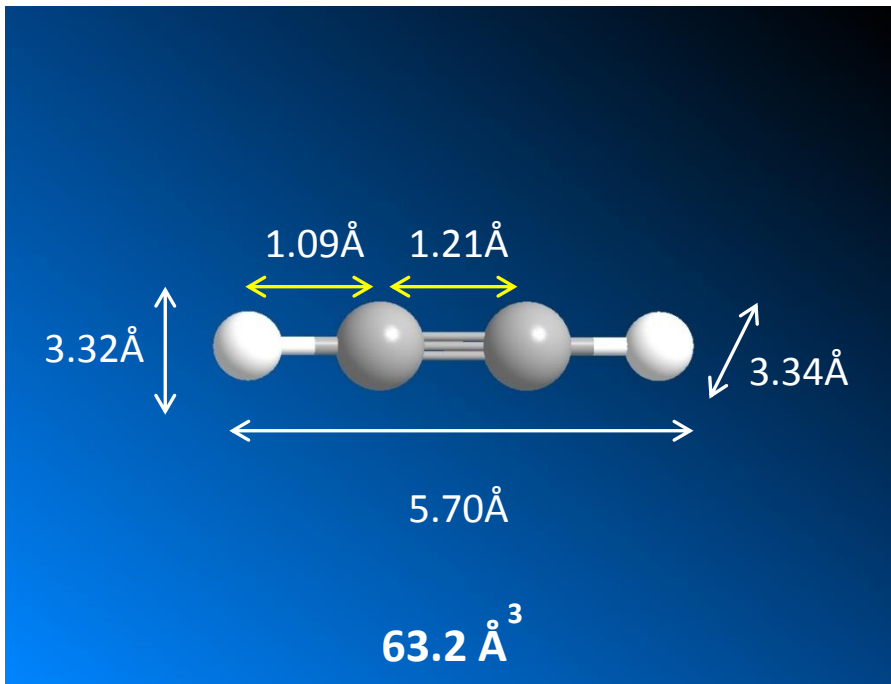
Figure 47. View of the molecular structure for C_2H_2.
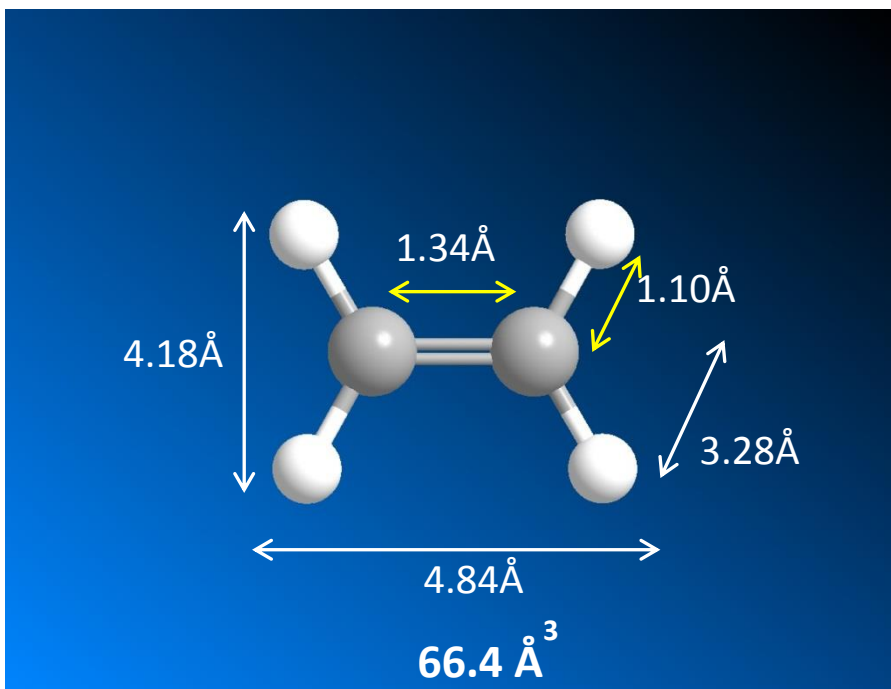
Figure 48. View of the molecular structure for C_2H_2.

Table 12. Summary of physical properties for C_2H_2 and C_2H_4.

	Molecular weight	Melting point (°C)	Boiling point (°C)	Density in bulk (g/cc)	Storage density[a] (g/cc)	Heat of vaporisation (kJ/mol)
C_2H_2	26.04	-84	-83.8	0.729 (Solid)	0.477 (65% of Solid)	20.9
C_2H_4	28.05	-169	-104	0.568 (Liquid)	0.397 (70% of liquid)	13.5

[a] measured at 273 K and 1.0 bar in NOTT-300

a   b
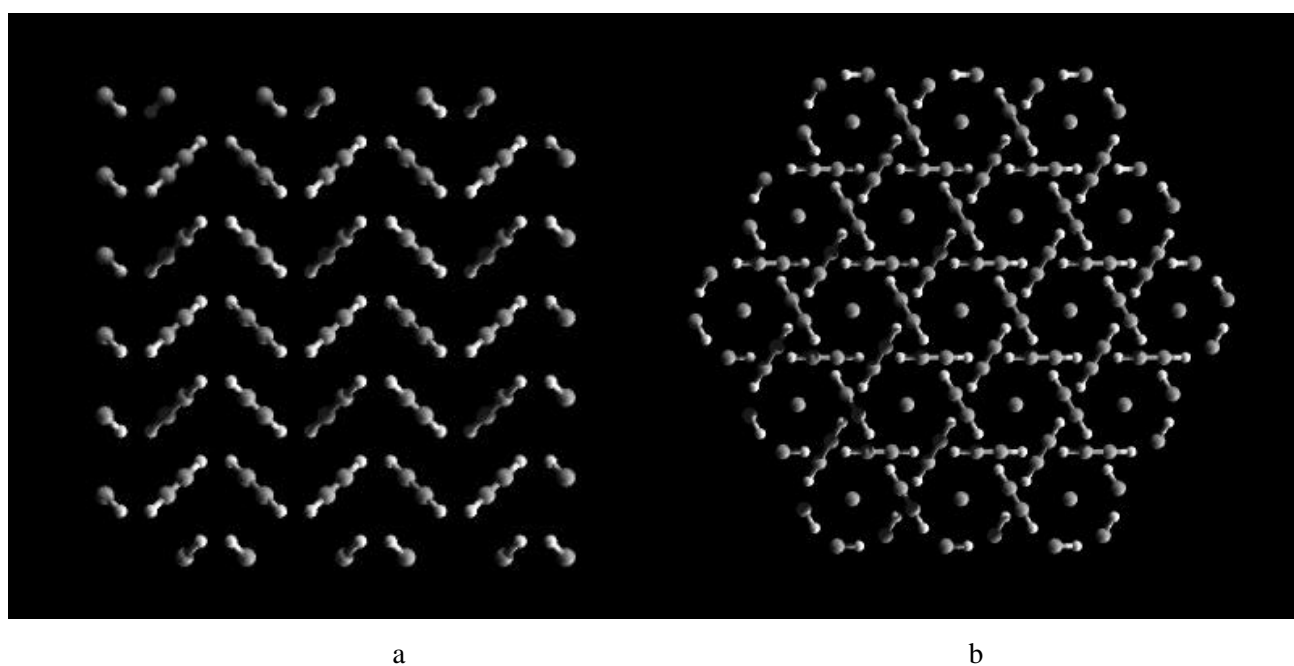
Figure 49. Views of the crystal structure for solid C_2H_2 along (a) the *a*-axis; (b) [111] direction.

a   b
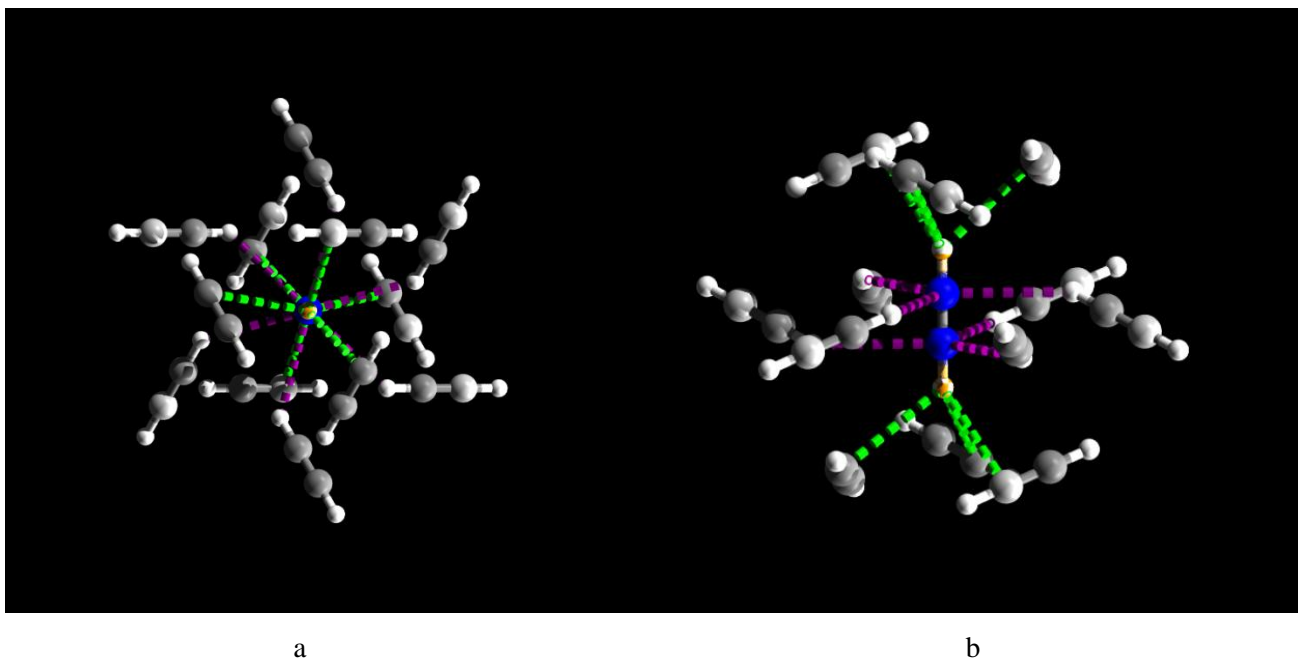
Figure 50. Views of the inter-molecular dipole interactions between C_2H_2 molecules in solid along (a) [111] direction; (b) the *a*-axis. The weak electrostatic dipole interactions between $C_2H_2(I)$ and $C_2H_2(II)$ molecules are highlighted in purple and green [$C^I \cdots H^{II}$ = 3.10 Å]. Each C_2H_2 molecule is involved in the formation of twelve such weak dipole inter-molecular interactions.
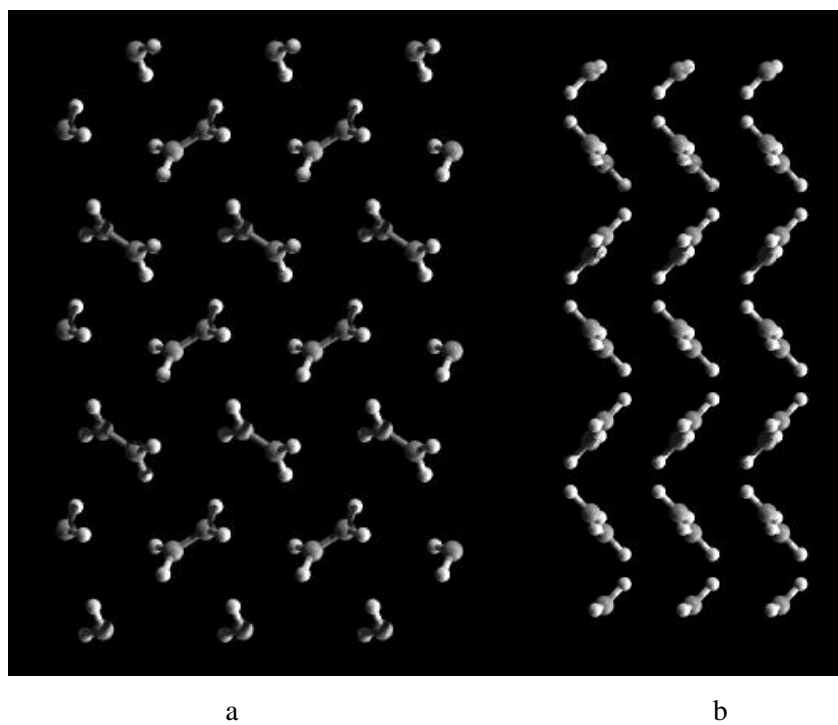
Figure 51. Views of the crystal structure for solid C_2H_4 along (a) the *a*-axis; (b) the *c*-axis.
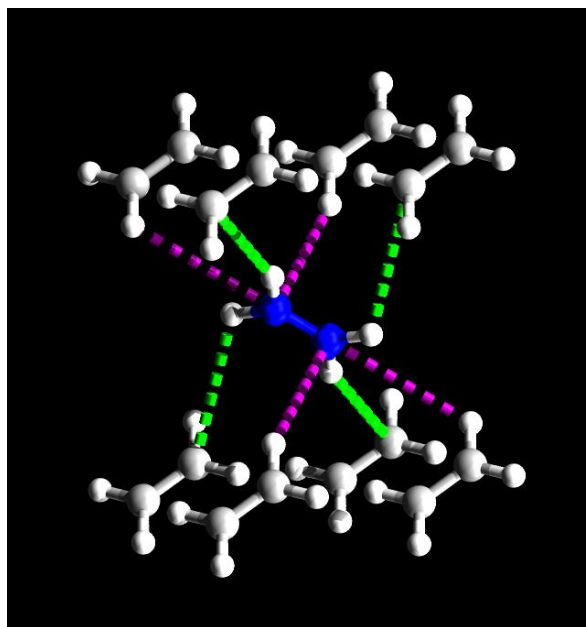
Figure 52. Views of the inter-molecular dipole interactions between C_2H_4 molecules in the solid state. The weak electrostatic dipole interactions between C_2H_4(I) and C_2H_4(II) molecules are highlighted in purple and green [$C^I \cdots H^{II}$ = 3.11 Å; $C^{II} \cdots H^I$ = 3.29 Å]. Each C_2H_4 molecule is involved in the formation of eight such weak dipole inter-molecular interactions.

8. Quasi-elastic Neutron Scattering (QENS) Spectra
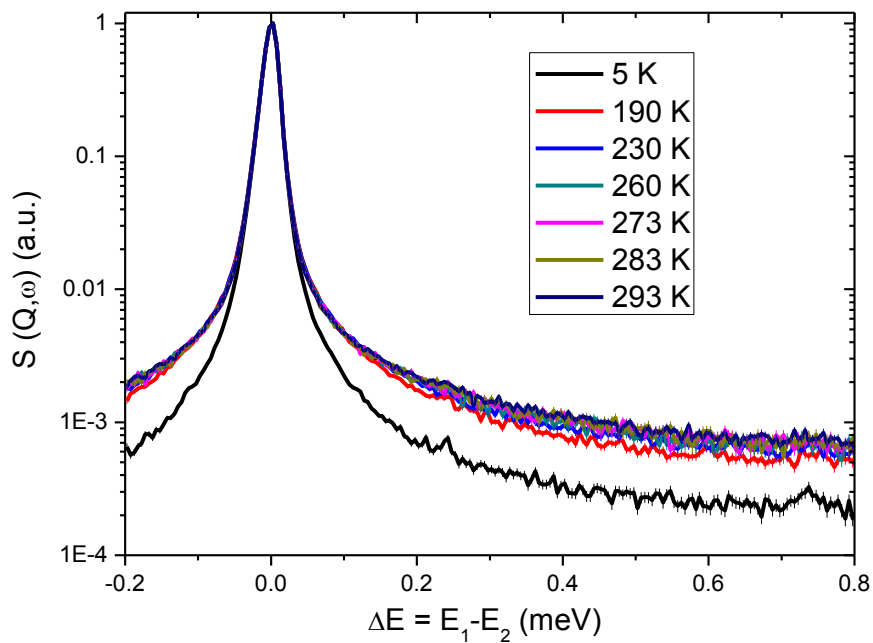
Figure 53. QENS spectra for bare NOTT-300 at 5-293 K. Clear QENS broadening is observed, suggesting the activated motion of free hydroxyl groups as temperature increases.
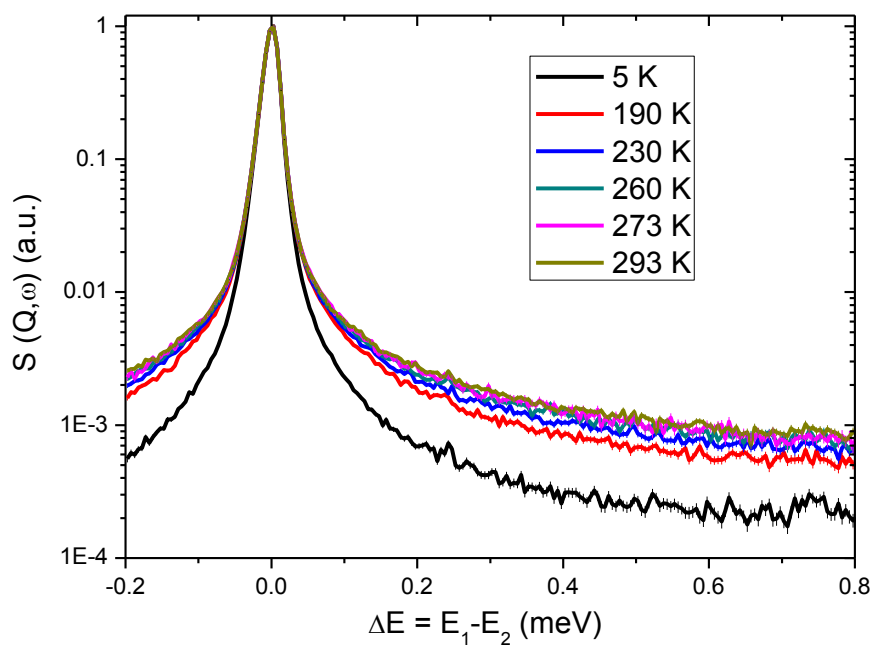
Figure 54. QENS spectra for NOTT-300·$2C_2H_2$ at 5-293 K.
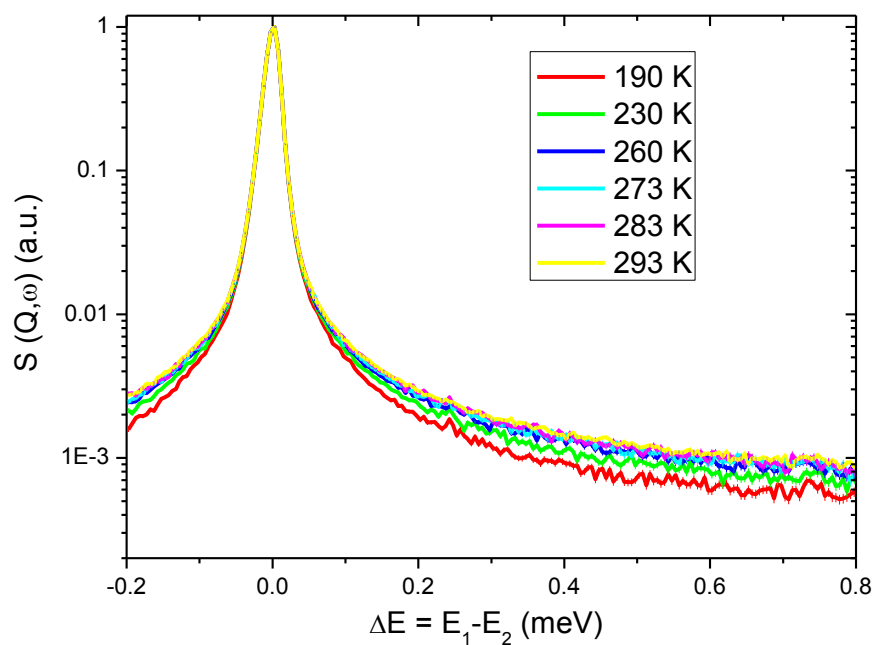
Figure 55. QENS spectra for NOTT-300·3C$_2$H$_2$ at 190-293 K. No significant QENS broadening was observed for this additional C$_2$H$_2$ dosing, suggesting adsorbed C$_2$H$_2$ molecules at both sites are strongly bound to the framework host and therefore have limited mobility.
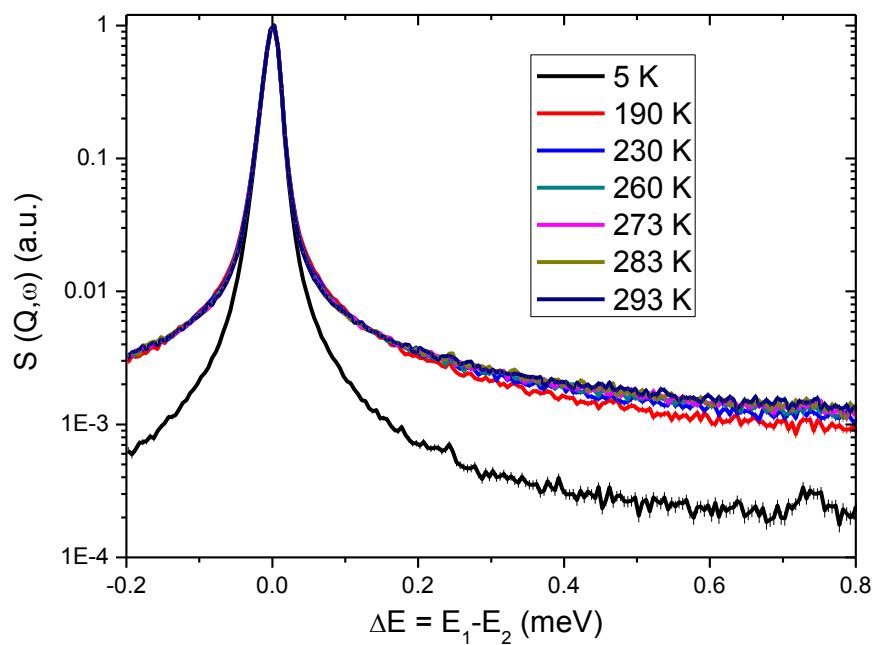
Figure 56. QENS spectra for NOTT-300·1C$_2$H$_4$ at 5-293 K.
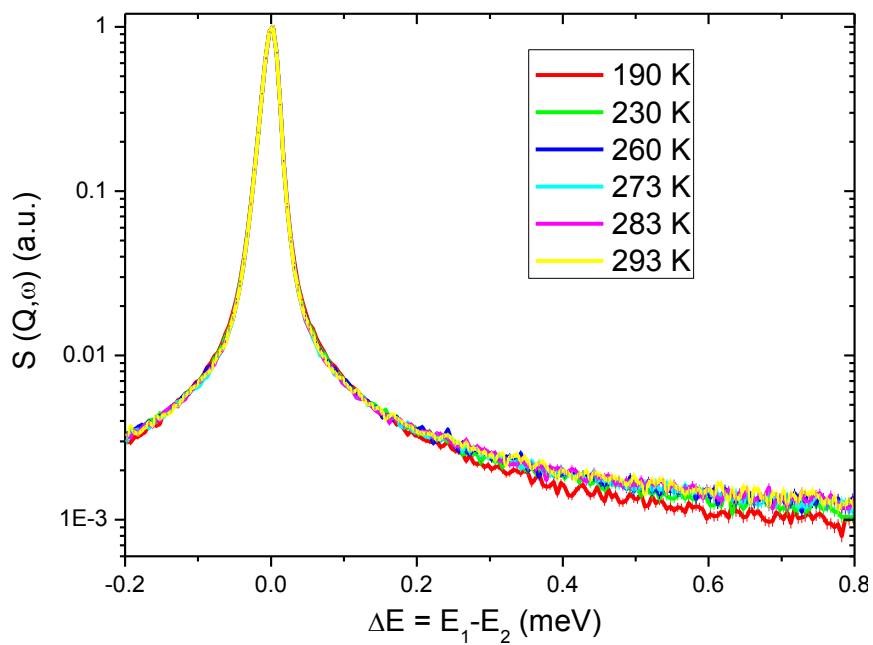
Figure 57. QENS spectra for NOTT-300 loaded with a 1:1mixture of C_2H_2-C_2H_4 at 190-293 K.
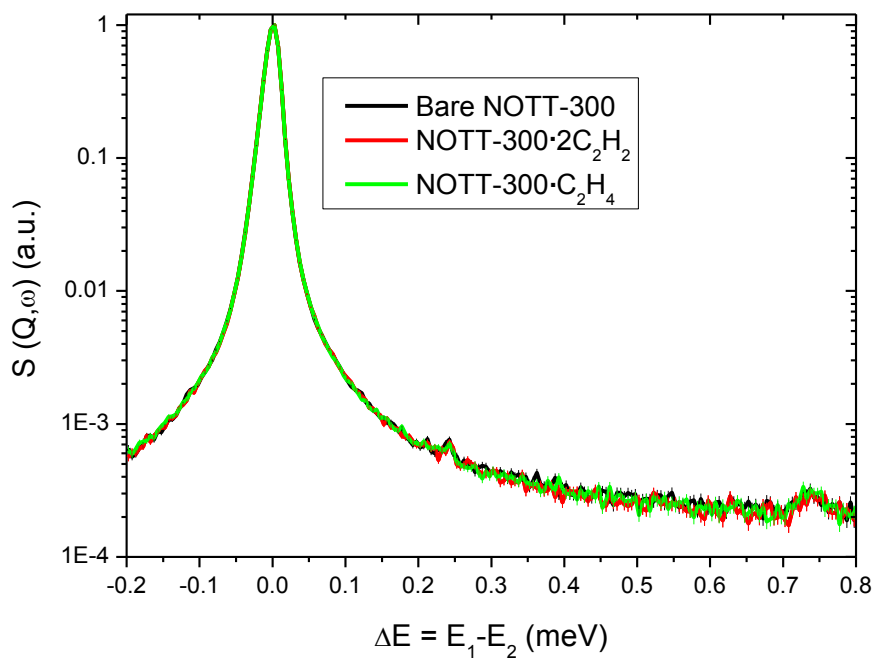
Figure 58. QENS spectra for bare NOTT-300, NOTT-300·$2C_2H_2$, NOTT-300·$1C_2H_4$ at 5 K.
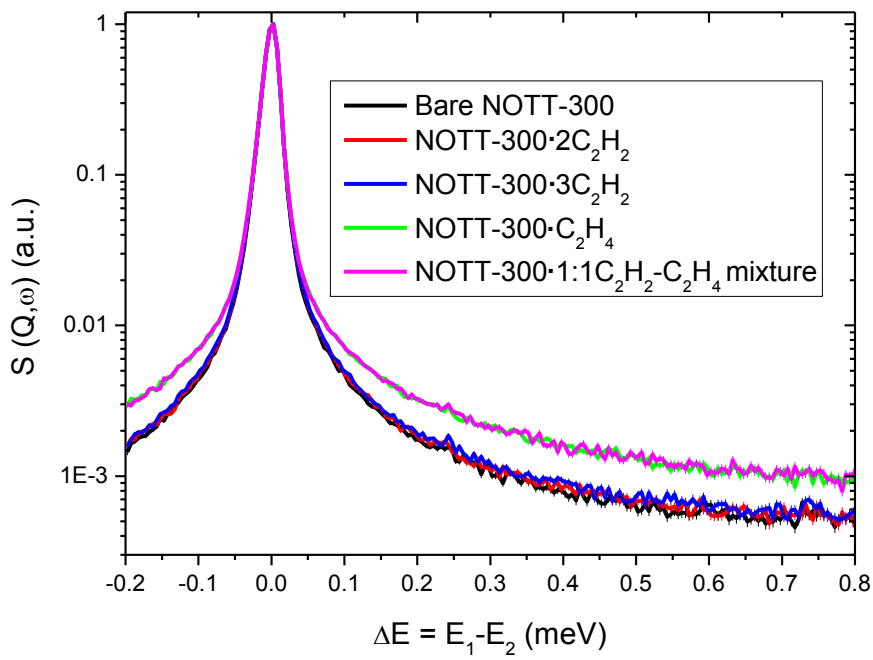
Figure 59. QENS spectra for bare NOTT-300, NOTT-300·2C$_2$H$_2$, NOTT-300·3C$_2$H$_2$, NOTT-300·1C$_2$H$_4$, and NOTT-300 loaded with a 1:1mixture of C$_2$H$_2$-C$_2$H$_4$ at 190 K.
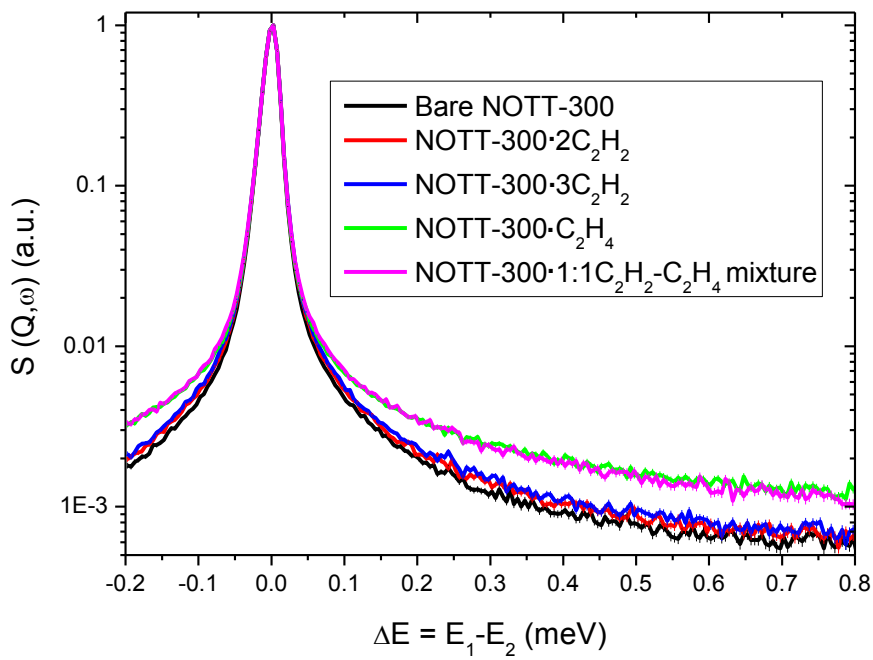
Figure 60. QENS spectra for bare NOTT-300, NOTT-300·2C$_2$H$_2$, NOTT-300·3C$_2$H$_2$, NOTT-300·1C$_2$H$_4$, and NOTT-300 loaded with a 1:1mixture of C$_2$H$_2$-C$_2$H$_4$ at 230 K.
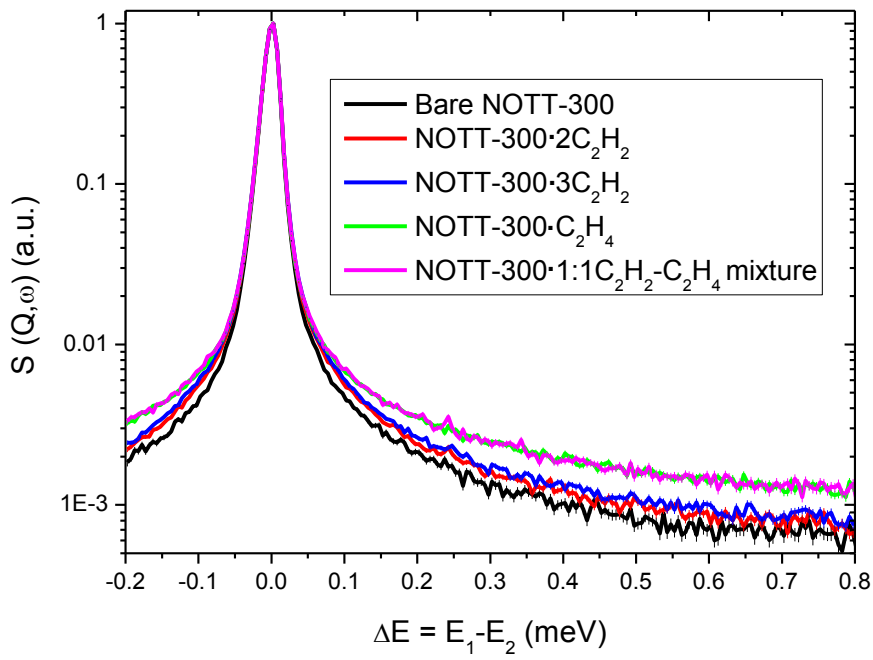
Figure 61. QENS spectra for bare NOTT-300, NOTT-300·2C$_2$H$_2$, NOTT-300·3C$_2$H$_2$, NOTT-300·1C$_2$H$_4$, and NOTT-300 loaded with a 1:1mixture of C$_2$H$_2$-C$_2$H$_4$ at 260 K.
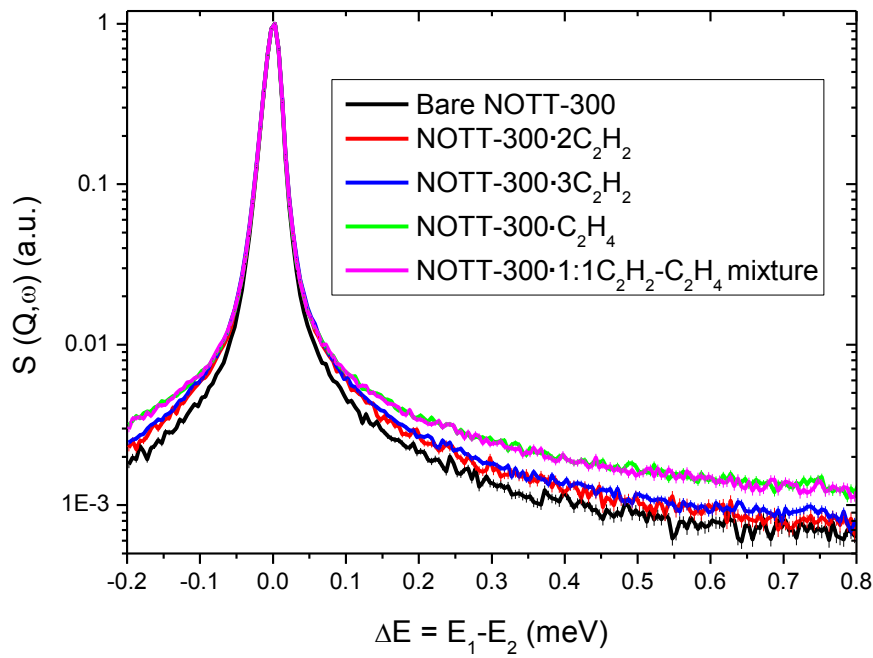
Figure 62. QENS spectra for bare NOTT-300, NOTT-300·2C$_2$H$_2$, NOTT-300·3C$_2$H$_2$, NOTT-300·1C$_2$H$_4$, and NOTT-300 loaded with a 1:1mixture of C$_2$H$_2$-C$_2$H$_4$ at 273 K.
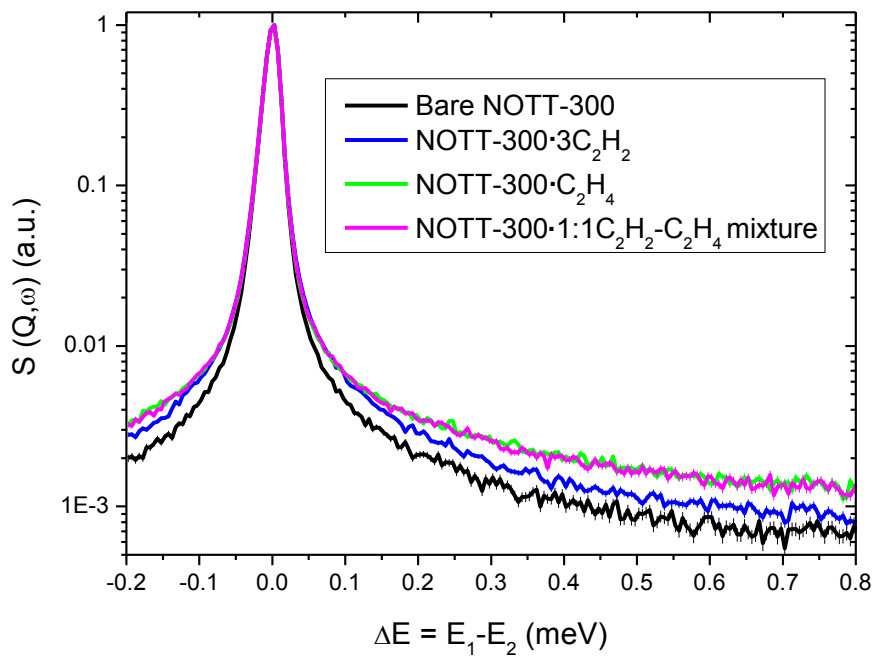
Figure 63. QENS spectra for bare NOTT-300, NOTT-300·2C$_2$H$_2$, NOTT-300·3C$_2$H$_2$, NOTT-300·1C$_2$H$_4$, and NOTT-300 loaded with a 1:1mixture of C$_2$H$_2$-C$_2$H$_4$ at 283 K.
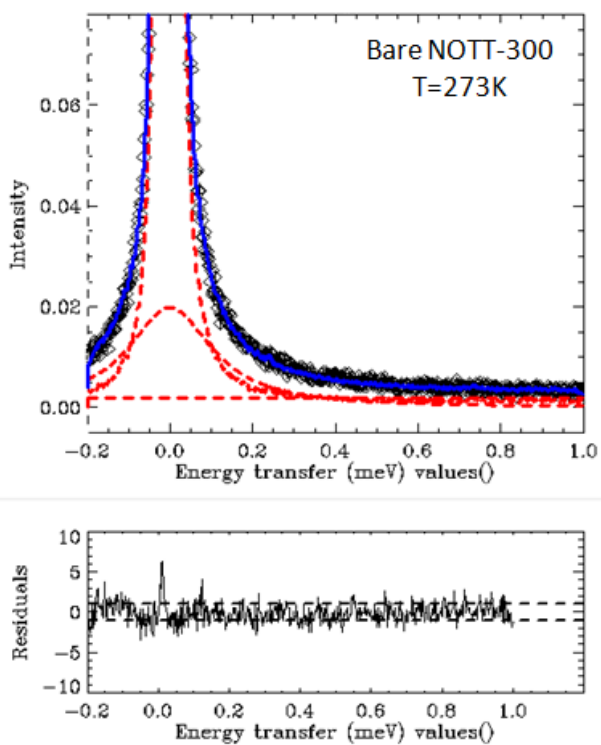
Figure 64. Lorentzian fitting of the QENS spectra at 273 K for bare NOTT-300.
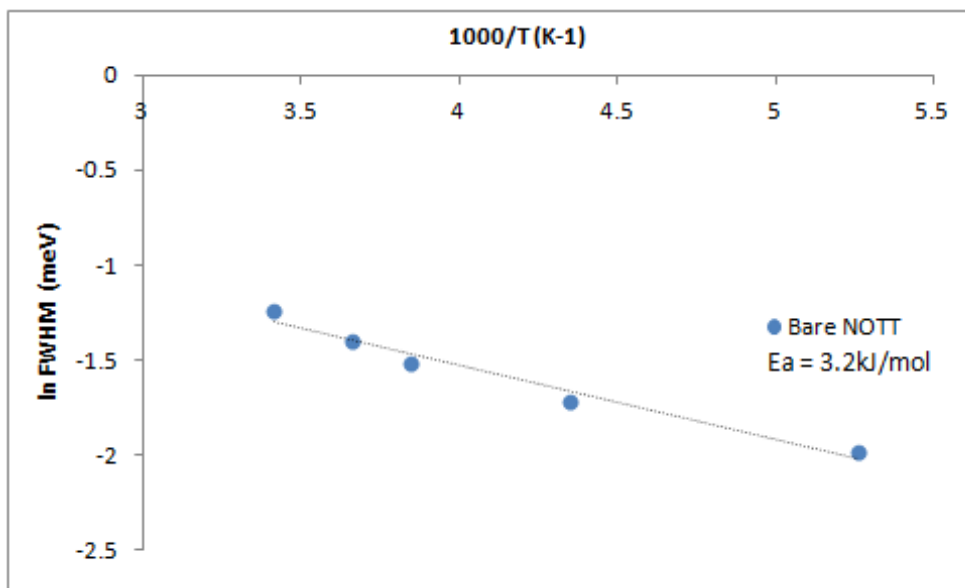
Figure 65. Arrhenius fitting of the full-width at half maximum of the Lorentzian of the QENS spectra at 190-293 K for bare NOTT-300.

9. Analysis and Derivation of the Isosteric Heat of Adsorption for C_2H_2 and C_2H_4 adsorption

To estimate the differential enthalpies (ΔH_n) and entropies (ΔS_n) for C_2H_2 and C_2H_4 adsorption, all isotherms at 273—303 K were fitted to the van't Hoff isochore (2):

$$\ln(p)_n = \frac{\Delta H_n}{RT} - \frac{\Delta S_n}{R} \tag{2}$$

where p is pressure, T is the temperature, R is the real gas constant. Selected linear fitting plots at 0.5, 1.0, 1.5 and 2.0 mmol g^{-1} are shown in Supplementary Figures 66-67. All linear fittings show R^2 above 0.99, indicating consistency of the isotherm data. A plot of $ln(p)$ versus $1/T$ at constant amount adsorbed allows the differential enthalpy and entropy of adsorption and also the isosteric enthalpy of adsorption ($Q_{st,n}$) to be determined.
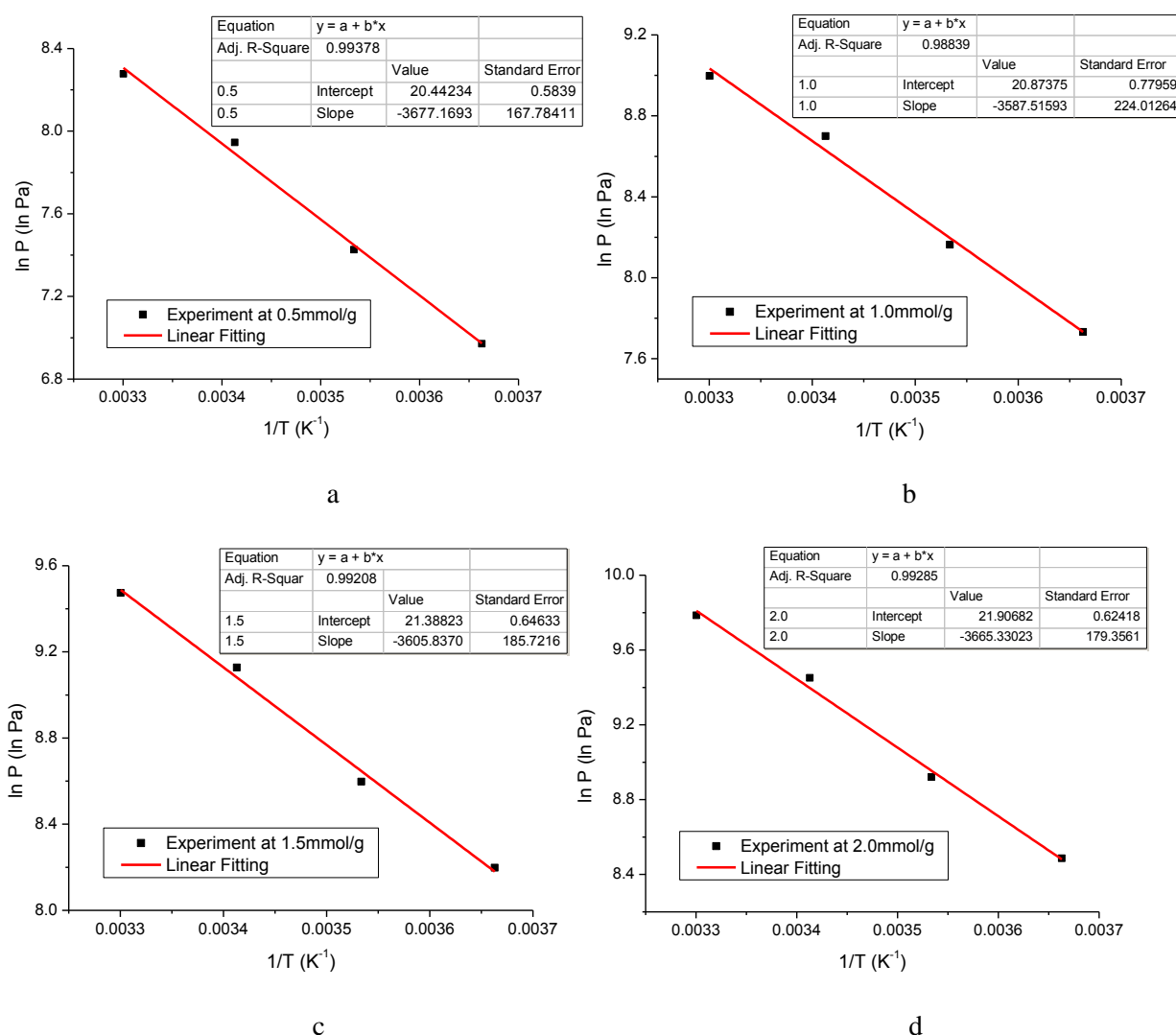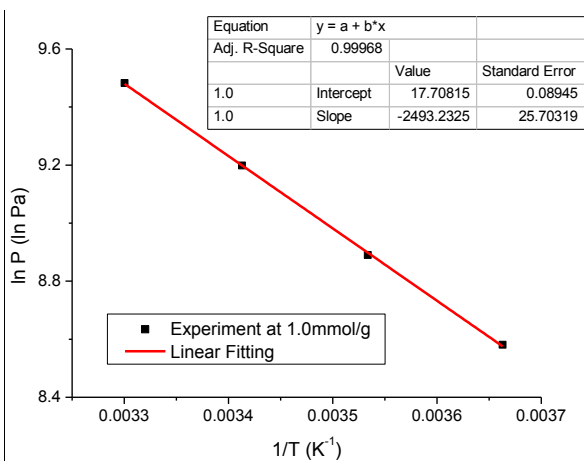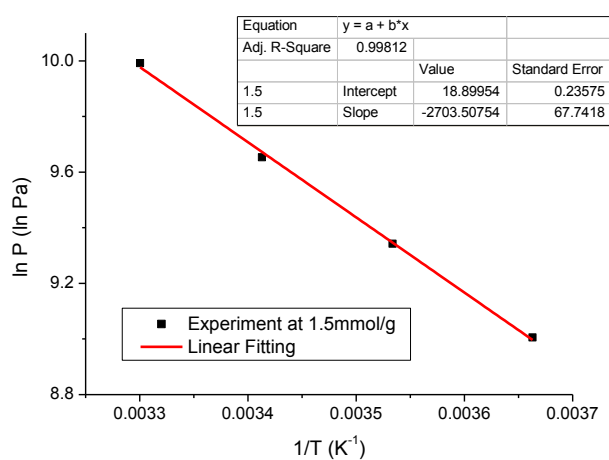

Figure 66. Linear fitting of Van't Hoff plots for the C_2H_2 adsorption isotherms at (a) 0.5, (b) 1.0, (c) 1.5 and (d) 2.0 mmol g^{-1} loadings in NOTT-300.
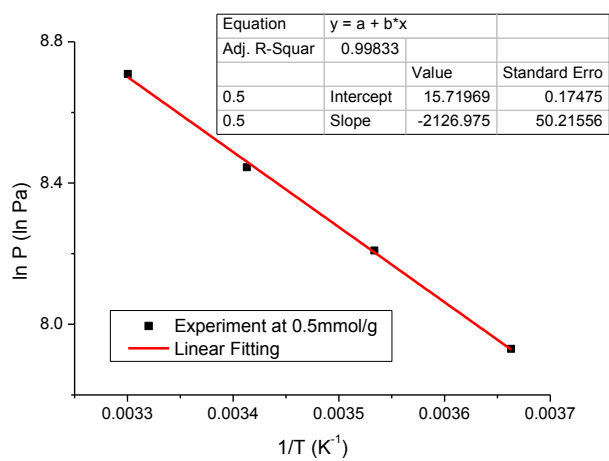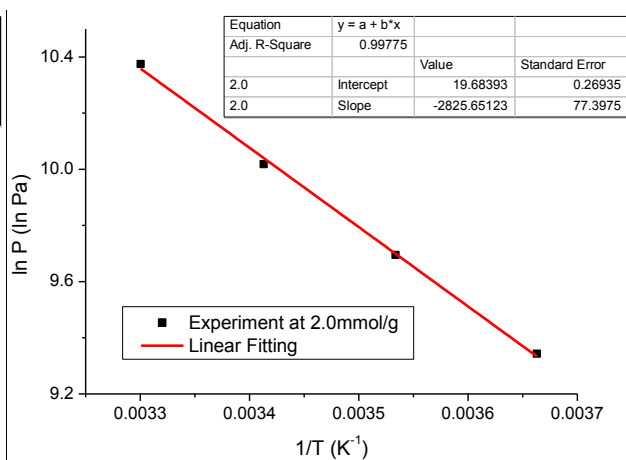
Figure 67. Linear fitting of Van't Hoff plots for the C_2H_4 adsorption isotherms at (a) 0.5, (b) 1.0, (c) 1.5 and (d) 2.0 mmol g^{-1} loadings in NOTT-300.

10. Analysis and Derivation of the Isosteric Heat of Adsorption for C_2H_6 adsorption

A virial-type expression (3) was used to fit the combined C_2H_6 isotherm data for NOTT-300 at 283 and 303 K:

$$\ln(p) = \ln(n) + (1/T)\sum_{i=0}^{m} a_i n^i + \sum_{j=0}^{n} b_j n^j \qquad (3)$$

Where P is the pressure expressed in mbar, N is the amount adsorbed in mmol/g, T is the temperature in K, a_i and b_i are virial coefficients, and m and n represent the number of coefficients required to adequately describe the isotherms. The equation was fit using the **R** statistical software package (www.R-project.org); m and n were gradually increased until the contribution of extra added a and b coefficients was deemed to be statistically insignificant toward the overall fit, as determined using the t-test. The values of the virial coefficients a_0 through a_m were then used to calculate the isosteric heat of adsorption using the following expression (4):

$$Q_{st} = -R\sum_{i=0}^{m} a_i n^i \qquad (4)$$

Here, Qst is the coverage-dependent isosteric heat of adsorption and R is the universal gas constant.
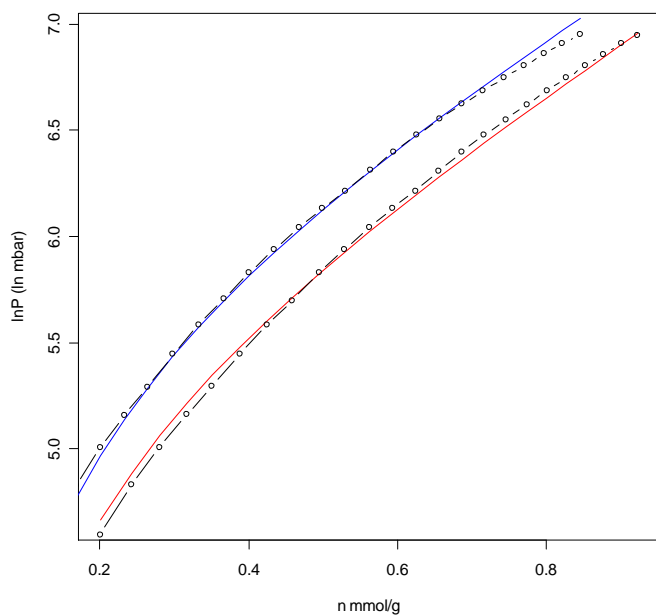

Figure 68. The virial simulation graph of C_2H_6 adsorption isotherms of NOTT-300 at 283 K and 303 K. Fitting residual error: 0.0352; fitting R^2>0.999. Fitting parameters: a_0, -1225; a_1, -960; a_2, 3653; a_3, -4428; a_4, 1925; b_0, 10.87.

11. Analytical fitting of the adsorption isotherms by dual-site Langmuir-Freundlich model

The adsorption isotherms of C_2H_2, C_2H_4, C_2H_6 and CH_4 in NOTT-300 at 293 K were fitted using a dual-site Langmuir-Freundlich model (equation 5), where n is the amount adsorbed in mmol g^{-1}, P is the pressure in bar, $q_{sat,i}$ is the saturation capacity in mmol g^{-1}, b_i is the Langmuir parameter in bar^{-1}, and v_i is the Freundlich parameter for two sites 1 and 2. The fitted parameters for each adsorption isotherm are listed in supplementary Table 13. Comparison of the adsorption isotherms and the corresponding dual-site Langmuir-Freundlich fits are shown in Supplementary Figure 69. The regression coefficients are all above 0.999 for the C_2H_2, C_2H_4, C_2H_6 and CH_4 adsorption data of NOTT-300, confirming that the model fits the data very well.

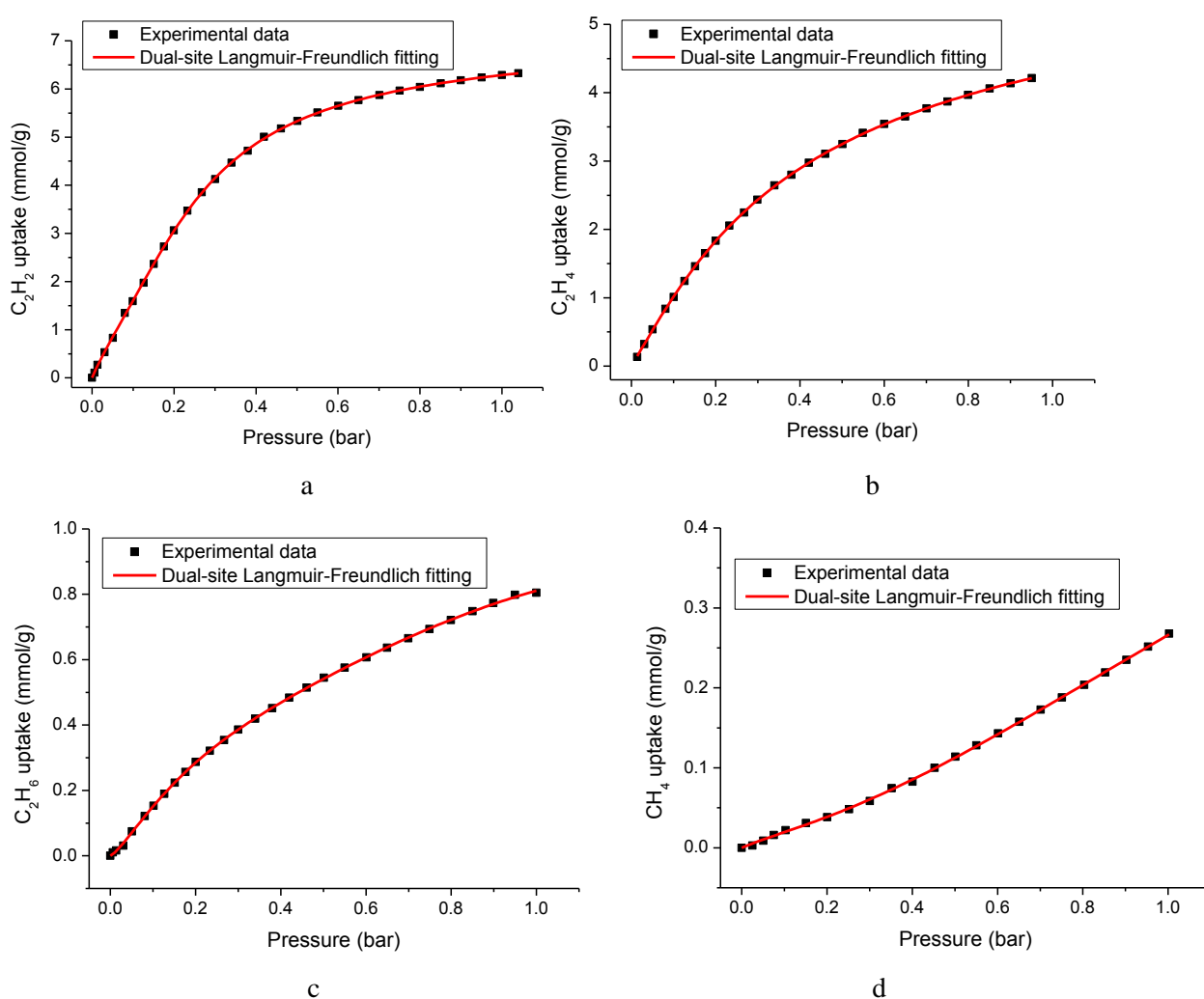$$n = \frac{q_{sat1}b_1P^{v_1}}{1+b_1P^{v_1}} + \frac{q_{sat2}b_2P^{v_2}}{1+b_2P^{v_2}}$$

(5)

Figure 69. The dual-site Langmuir-Freundlich fitting for (a) C_2H_2, (b) C_2H_4, (c) C_2H_6 and (d) CH_4 adsorption isotherms in NOTT-300 at 293 K.

Table 13. Summary of the dual-site Langmuir-Freundlich fitting parameters for C_2H_2, C_2H_4, C_2H_6 and CH_4 adsorption isotherms in NOTT-300 at 293 K.

	C_2H_2	C_2H_4	C_2H_6	CH_4
q_{sat1} (mmol g^{-1})	4.368	5.636	0.7061	0.870
b_1 (bar^{-1})	3.751	1.866	5.174	0.365
v_1 (dimensionless)	0.956	1.000	1.283	1.782
q_{sat2} (mmol g^{-1})	2.962	0.658	0.364	0.0389
b_2 (bar^{-1})	23.10	13.65	1.518	5.825
v_2 (dimensionless)	2.270	1.739	2.926	1.000
R^2	0.9999	0.9999	0.9999	0.9997
Residual	0.0068	0.0014	$2.3e^{-4}$	$4.1e^{-5}$

12. IAST Analysis of the selectivity data of hydrocarbon adsorption in NOTT-300

Ideal adsorbed solution theory (IAST)[10] was used to determine the selectivity factor, S, for binary mixtures using pure component isotherm data. The selectivity factor, S, is defined according to Equation 6 where x_i is the amount of each component adsorbed as determined from IAST and y_i is the mole fraction of each component in the gas phase at equilibrium. The IAST adsorption selectivities were calculated for C_2H_2/C_2H_4, C_2H_4/C_2H_6, C_2H_2/CH_4, C_2H_4/CH_4, and C_2H_6/CH_4 binary mixtures of varying compositions (5:95 to 95:5) at 293 K and a total pressure of 1.0 bar. The selectivity of C_2H_2/CH_4, C_2H_4/CH_4, and C_2H_6/CH_4 binary mixtures are subject to uncertainties associated with isotherm measurement of the extremely low methane uptake in NOTT-300. The accuracy of the IAST analysis starts to decay when (i) strong binding sites appear on the pore surface of the host material (*i.e.* the pore surface is not homogenous), and (ii) in the gas mixture one component is much more strongly adsorbed than the other.[10] These selectivity data are shown in Supplementary Figure 70, and importantly have also been confirmed with multi-component gas adsorption experiment (see below please). The IAST selectivity data S for a 50:50 mixture adsorption in NOTT-300 are reported in Table 1.

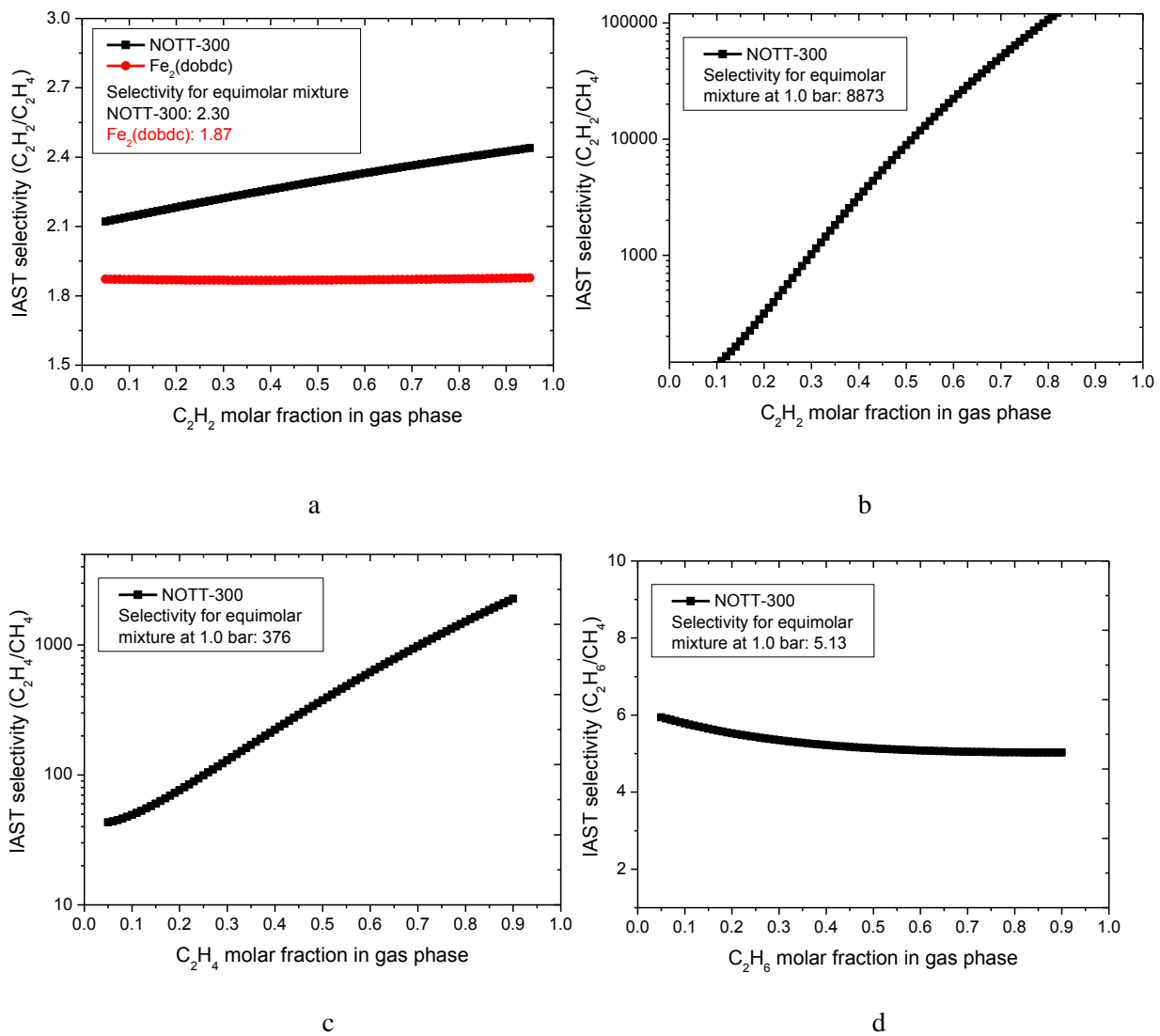$$S = \frac{x_1 / y_1}{x_2 / y_2} \qquad (6)$$

Figure 70. IAST selectivities for binary mixtures of (a) C_2H_2 and C_2H_4, (b) C_2H_2 and CH_4, (c) C_2H_4 and CH_4 and (d) C_2H_6 and CH_4 of varying compositions at a total pressure of 1.0 bar and 293 K.

13. Adsorption isotherms of equimolar binary hydrocarbon mixtures in NOTT-300 and IAST analysis

To validate the selectivities obtained from IAST analysis, we also measured dual-component adsorption isotherms for equimolar mixtures of C_2H_2/C_2H_4, C_2H_4/C_2H_6, C_2H_2/CH_4, and C_2H_4/CH_4 at 293 K under flow mode using two identical mass flow controllers. In contrast to a typical static isotherm experiment, flow experiments allow the gas in the sample station to be constantly refreshed by a flow of equimolar gas mixture to guarantee that the mixture composition in the gas phase is unchanged throughout the experiment. The measured uptakes of hydrocarbon mixtures were compared with those predicted by IAST calculations[10] (Supplementary Figures 71-74). Due to the low uptakes of both C_2H_6 and CH_4, the measurement of C_2H_6/CH_4 mixture uptake suffers relatively large uncertainties and is not reported here. Excellent agreements have been seen for other binary mixtures confirming the capability of hydrocarbon separation in NOTT-300 at ambient conditions.
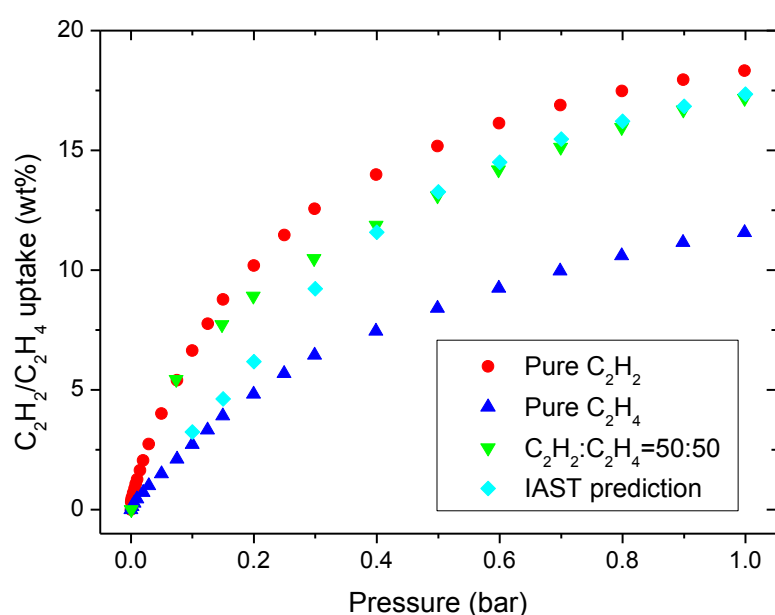

Figure 71. Comparison of the adsorption isotherms for C_2H_2, C_2H_4, and an equimolar mixture of C_2H_2/C_2H_4 at 293 K in NOTT-300. Data were measured in flow mode. Prediction from the IAST calculation is shown in cyan.
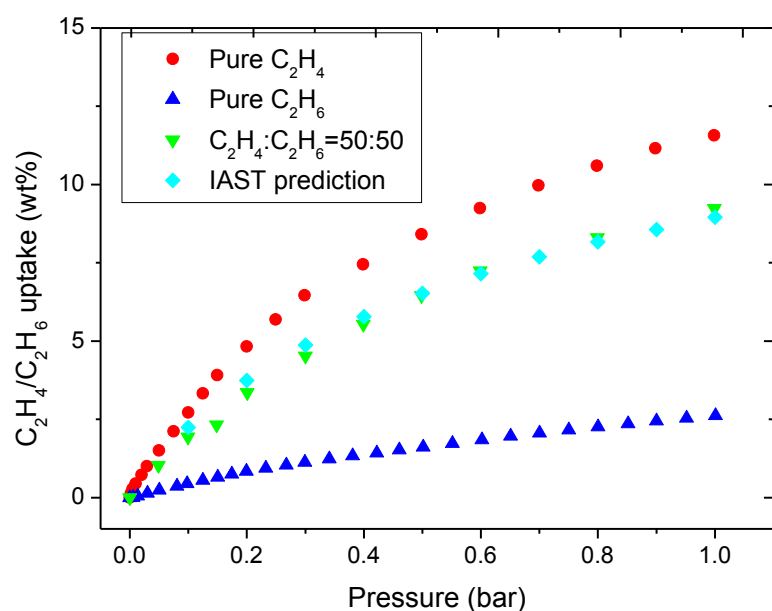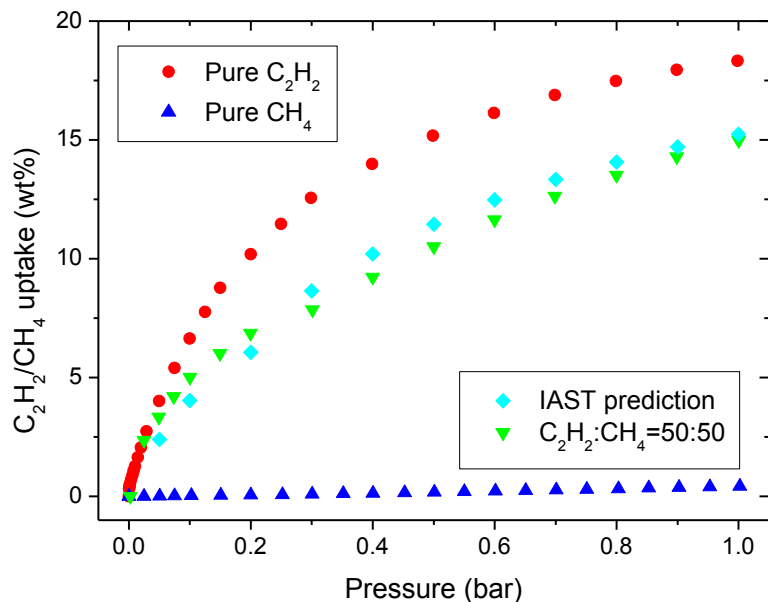

Figure 72. Comparison of the adsorption isotherms for C_2H_4, C_2H_6, and an equimolar mixture of C_2H_4/C_2H_6 at 293 K in NOTT-300. Data were measured in flow mode. Prediction from the IAST calculation is shown in cyan.
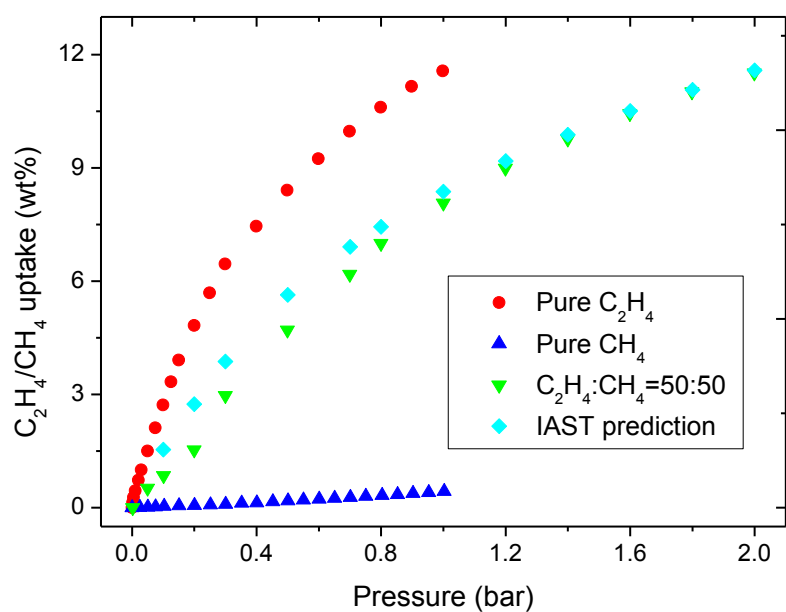
96

Figure 73. Comparison of the adsorption isotherms for C_2H_2, CH_4, and an equimolar mixture of C_2H_2/CH_4 at 293 K in NOTT-300. Data were measured in flow mode. Prediction from the IAST calculation is shown in cyan.

Figure 74. Comparison of the adsorption isotherms for C_2H_4, CH_4, and an equimolar mixture of C_2H_4/CH_4 at 293 K in NOTT-300. Data were measured in flow mode. Prediction from the IAST calculation is shown in cyan.
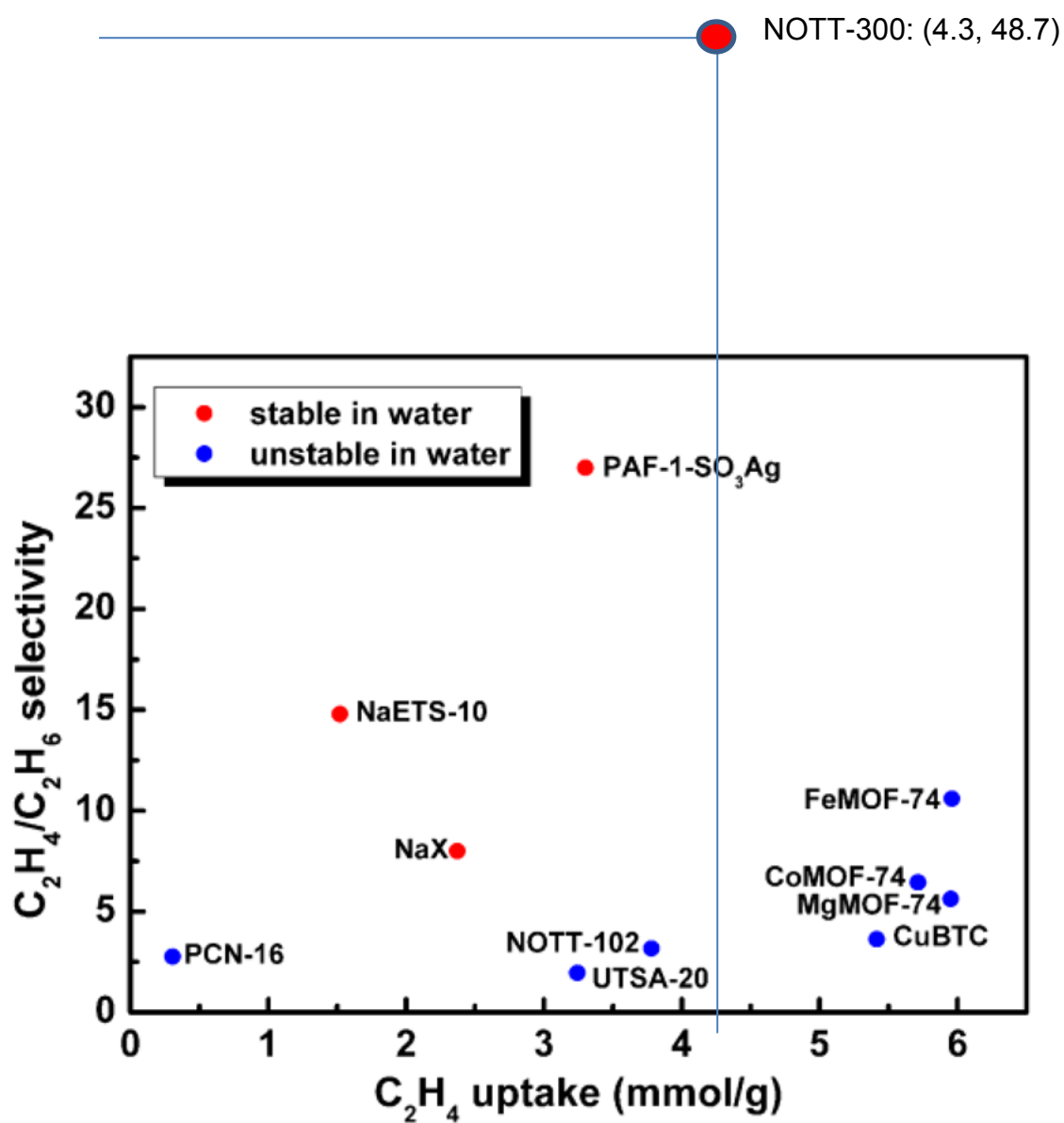
Figure 75. Summary of C_2H_4/C_2H_6 selectivities in porous materials. Reproduced and modified from Ma *et al*. *J. Am. Chem. Soc.*, 2014, **136**, 8654.

14.   Breakthrough experiments

To further evaluate the performance of NOTT-300 in an adsorption-based separation process, breakthrough experiments were performed in which an equimolar mixture of C_2H_2 and C_2H_4 was flowed through a packed bed of NOTT-300 with a total flow of 2 ml/min at 293 K and 1.0 bar. The C_2H_2/C_2H_4 mixture was selected because it currently represents the most challenging mixture for adsorption based separations. As suggested from pure component isotherms and IAST calculations, NOTT-300 has selectivity to C_2H_2. In the breakthrough experiment, C_2H_4 was the first to elute through the bed, with C_2H_2 retained. Upon saturation, C_2H_2 broke through from the bed and reaches saturation rapidly. As measured from this breakthrough experiment, for an entering equimolar mixture of $C_2H_2/$ C_2H_4, the C_2H_4 composition can be purified to 99.5% which then drops to 97.5% until C_2H_2 started to break through.

Dimensionless breakthrough plots were also calculated with the following parameters: bed diameter, d, (7 mm), bed length, L, (120 mm), flow rate (2 ml/min), bed volume (5 ml), sample mass (3.4 g), sample framework density (1.06 g/cc). The sample occupies a volume of 3.21 ml (assuming 100% purity and no framework collapse), and thus the fractional porosity of the fixed bed, ε, is calculated to be 0.358. The superficial gas velocity, u, at the entrance of the bed corresponds to $8.66e^{-4}$ m/s. The characteristic contact time between the gas and the NOTT-300 samples, $\varepsilon L/u =$ 49.61 s. The dimensionless time, τ, was obtained by dividing the actual time, t, by the contact time between the gas and the NOTT-300 sample, $\varepsilon L/u$, i.e. $\tau = tu/\varepsilon L$. The dimensionless breakthrough plots are shown in Supplementary Figure 78.
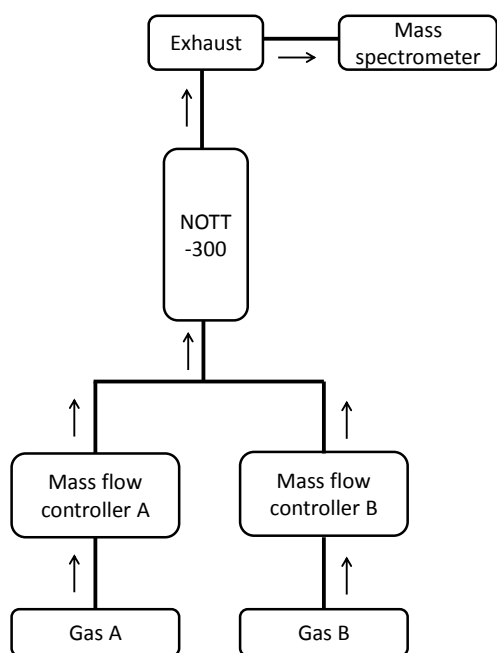

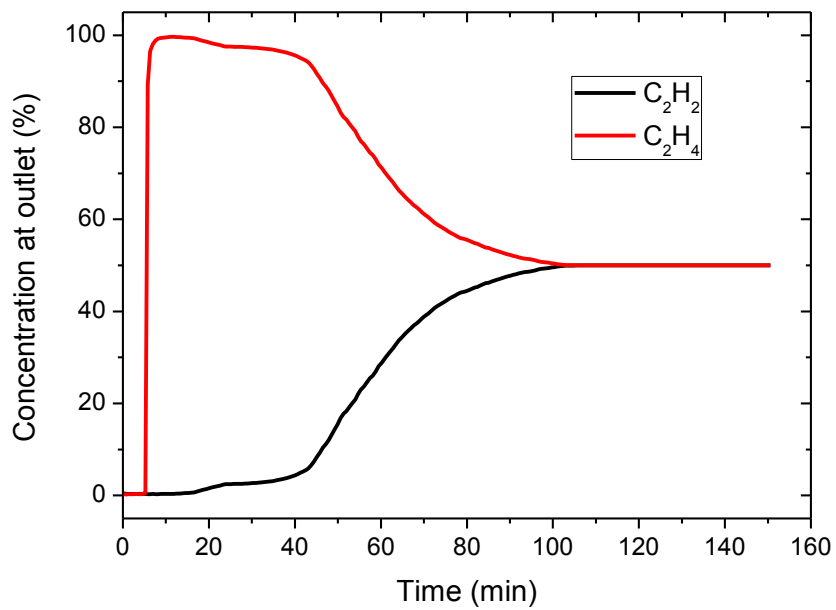Figure 76. Schematic view of the breakthrough reactor used in this study.

Figure 77. Breakthrough plots for an equimolar mixture of C_2H_2/C_2H_4 through NOTT-300 at room temperature and atmospheric pressure conditions.
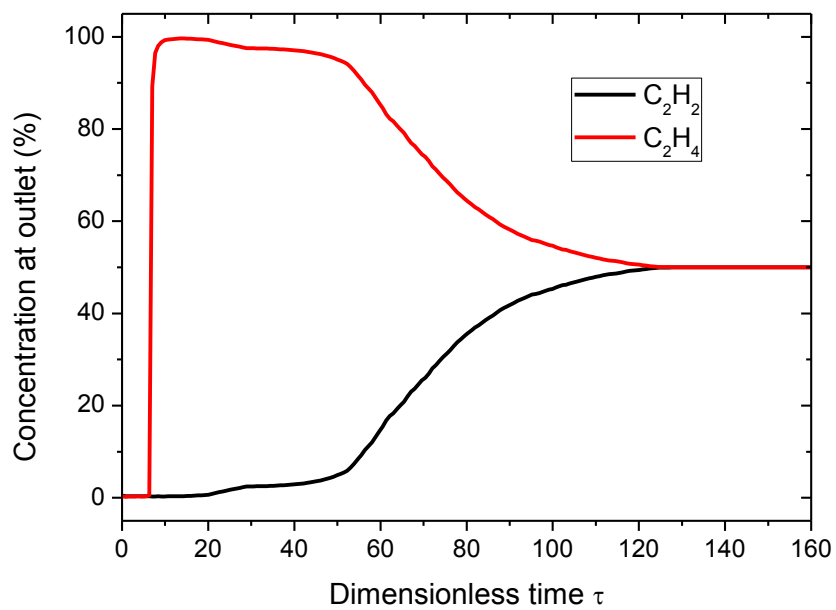

Figure 78. Dimensionless breakthrough plots for C_2H_2/C_2H_4 equimolar mixture in NOTT-300 at room temperature and atmospheric pressure conditions.

15. References:

1   S. Yang *et al.*, Selectivity and direct visualization of carbon dioxide and sulfur dioxide in a decorated porous host. *Nature Chem.* **4**, 887 (2012)

2   S. J. Clark, *et al.* First principles methods using CASTEP. *Z. Kristall.* **220**, 567, (2005).

3   J. P. Perdew, K. Burke, M. Ernzerhof, Generalized gradient approximation made simple. *Phys. Rev. Lett.* **77**, 3865, (1996).

4   A. J. Ramirez-Cuesta, aCLIMAX 4.0.1, The new version of the software for analyzing and interpreting INS spectra. *Comput. Phys. Commun.* **157**, 226, (2004).

5   H. Jobic, D. N. Theodorou, Quasi-elastic neutron scattering and molecular dynamics simulation as complementary techniques for studying diffusion in zeolites. *Microporous Mesoporous Mater.* **102**, 21 (2007).

6   S. P. Thompson, *et al.*, Beamline I11 at Diamond: a new instrument for high resolution powder diffraction. *Rev. Sci. Instrum.* **80**, 075107 (2009).

7   H. M. Rietveld, A profile refinement method for nuclear and magnetic structures. *J. Appl. Crystallogr.* **2**, 65 (1969).

8   L.C. Chapon, P. Manuel *et al*, *Neutron News* **22,** 22 (2011).

9   Bloch, E. D. *et al.* Hydrocarbon separations in a metal-organic framework with open iron(II) coordination sites. *Science* **335**, 1606-1610 (2012).

10   Myers, A. L. & Prausnitz, J. M. Thermodynamics of mixed-gas adsorption. *AIChE J.* **11**, 121-127 (1965).